

EXPERIMENTAL AND THEORETICAL ANALYSES ON THE ULTRASONIC  
CAVITATION PROCESSING OF AL-BASED ALLOYS  
AND NANOCOMPOSITES

by

SHIAN JIA

LAURENTIU NASTAC, COMMITTEE CHAIR

MARK L. WEAVER  
J. BRIAN JORDON  
PAUL G. ALLISON  
AMBER L. GENAU

A DISSERTATION

Submitted in partial fulfillment of the requirements  
for the degree of Doctor of Philosophy in the  
Department of Metallurgical and Materials Engineering  
in the Graduate School of  
The University of Alabama

TUSCALOOSA, ALABAMA

2015

Copyright Shian Jia 2015  
ALL RIGHTS RESERVED

## ABSTRACT

Strong evidence is showing that microstructure and mechanical properties of a casting component can be significantly improved if nanoparticles are used as reinforcement to form metal-matrix-nano-composite (MMNC). In this paper, 6061/A356 nanocomposite castings are fabricated using the ultrasonic stirring technology (UST). The 6061/A356 alloy and  $\text{Al}_2\text{O}_3/\text{SiC}$  nanoparticles are used as the matrix alloy and the reinforcement, respectively. Nanoparticles are injected into the molten metal and dispersed by ultrasonic cavitation and acoustic streaming. The applied UST parameters in the current experiments are used to validate a recently developed multiphase Computational Fluid Dynamics (CFD) model, which is used to model the nanoparticle dispersion during UST processing. The CFD model accounts for turbulent fluid flow, heat transfer and the complex interaction between the molten alloy and nanoparticles using the ANSYS Fluent Dense Discrete Phase Model (DDPM). The modeling study includes the effects of ultrasonic probe location and the initial location where the nanoparticles are injected into the molten alloy.

The microstructure, mechanical behavior and mechanical properties of the nanocomposite castings have been also investigated in detail. The current experimental results show that the tensile strength and elongation of the as-cast nanocomposite samples (6061/A356 alloy reinforced by  $\text{Al}_2\text{O}_3$  or SiC nanoparticles) are improved. The addition of the  $\text{Al}_2\text{O}_3$  or SiC nanoparticles in 6061/A356 alloy matrix changes the fracture mechanism from brittle dominated to ductile dominated.

## DEDICATION

This dissertation is dedicated to everyone who helped me and guided me through the trials and tribulations of creating this manuscript. In particular, I would like to thank from my heart my family and close friends who stood by me throughout the time taken to complete this work.

## LIST OF ABBREVIATIONS AND SYMBOLS

$v_p$	Volume fraction of the particles
$\sigma_m$	Yield strength of the unreinforced matrix
$k_y$	Strengthening coefficient
$d_p$	Particle diameter
$d_m$	Grain size
$G_E$	Equiaxed grain density
$\theta_i$	Preferential crystallographic orientation angle
P	Power
f	Frequency
A	Amplitude
$f_b$	Bubble volume fraction
$\rho_b$	Bubble density
$\vec{V}_b$	Bubble phase velocity
$R_G$	Mass transfer source terms related to the growth of the cavitation bubbles
$R_C$	Mass transfer source terms related to the collapse of the cavitation bubbles
$R_b$	Bubble radius
$\sigma_L$	Surface tension coefficient of the liquid phase
$\rho_L$	Liquid density
$\nu_L$	Kinematic viscosity of the liquid phase

$p_b$  Bubble surface pressure

$p$  Local far-field pressure

## ACKNOWLEDGMENTS

I am pleased to have this opportunity to thank my colleagues, friends, and the MTE faculty who have helped me with this research project. I am most indebted to Dr. Laurentiu Nastac, the chairman of this dissertation, for sharing his research expertise and for mentoring me throughout my PhD program at the University of Alabama. I would also like to thank all of my committee members, Dr. Mark Weaver, Dr. Brian Jordon, Dr. Paul Allison, and Dr. Amber Genau for their invaluable input, inspiring and constructive comments, and support of both the dissertation and my academic progress. I would like to thank Daojie Zhang for his assistance in modeling and simulation work in this study. I would like to thank Yang Xuan and Robert Fanning for their assistance with the experimental work.

This research would not have been possible without the support of my friends and fellow graduate students and of course of my family who never stopped encouraging me to persist.

## CONTENTS

ABSTRACT.....	ii
DEDICATION.....	iii
LIST OF ABBREVIATIONS AND SYMBOLS .....	iv
ACKNOWLEDGMENTS .....	vi
LIST OF TABLES.....	ix
LIST OF FIGURES .....	x
CHAPTER 1 – INTRODUCTION.....	1
CHAPTER 2 – LITERATURE REVIEW .....	5
2.1 A356 and 6061 Alloys.....	5
2.2 Metal-Matrix-Composites vs. Metal-Matrix-Nanocomposites.....	5
2.3 Effects of Ultrasonic Stirring.....	8
2.4 Novel Fabrication Methods of Nanocomposites .....	11
2.5 Strengthening Mechanisms.....	17
2.5.1 Load Transfer Effect.....	17
2.5.2 Hall-Petch Strengthening.....	18
2.5.3 Orowan Strengthening .....	18
2.5.4 CTE and M Mismatch.....	19
2.6 Modeling of Ultrasonic Cavitation and Nanodispersion Phenomena during Molten Metal and Solidification Processing.....	19
CHAPTER 3 – EXPERIMENTAL APPROACH .....	23

CHAPTER 4 – MODELING APPROACH.....	26
4.1 CFD Ultrasonic Cavitation Model.....	26
4.2 CFD Nanodispersion Model.....	28
CHAPTER 5 – SIMULATION RESULTS AND DISCUSSION.....	31
5.1 CFD Ultrasonic Cavitation Modeling Results.....	31
5.2 CFD Nanodispersion Modeling Results.....	32
CHAPTER 6 – EXPERIMENTAL RESULTS AND DISCUSSION.....	38
6.1 Microscopy Analysis of 6061 / 1.0 wt. % SiC Samples.....	38
6.2 Analysis of Mechanical Properties of 6061 and A356 Nanocomposites.....	48
6.3 Microscopy Analysis of A356 Based Samples Treated during Solidification.....	55
CHAPTER 7 – CONCLUSIONS AND RECOMMENDATIONS FOR FUTURE WORK.....	66
7.1 Conclusions.....	66
7.2 Main Contributions of This Study.....	67
7.3 Recommendations for Future Work.....	68
REFERENCES.....	70

## LIST OF TABLES

Table 2.1 Nominal chemical composition of matrix alloy studied (in wt. %)	5
Table 6.1 Tensile testing results for A356 samples	48
Table 6.2 Tensile testing results for some other A356 alloy based nanocomposites samples	51
Table 6.3 Tensile testing results for 6061 samples	52
Table 6.4 EDS spectrum result	64

## LIST OF FIGURES

Figure 2.1 Ultrasonic treatment: prediction of the solidification structure for an A356 alloy (2 mm x 4 mm test geometry): (a) without UST ( $G_E = 5 \times 10^7$ nuclei/m <sup>2</sup> ); (b) with UST and high superheat ( $G_E = 5 \times 10^8$ nuclei/m <sup>2</sup> ); (c) with UST and low superheat ( $G_E = 5 \times 10^9$ nuclei/m <sup>2</sup> ) and (d) with UST, low superheat and 1% SiC nanoparticles ( $G_E = 5 \times 10^{10}$ nuclei/m <sup>2</sup> ) [113] .....	21
Figure 3.1 UST equipments: (a) ultrasonic probe, injector and induction furnace (b) generator and (c) ASTM B108-02 standard metal mold.....	25
Figure 4.1 Model geometry.....	28
Figure 4.2 Velocity inlet profile.....	29
Figure 5.1 (a) Cavitation region and (b) velocity vectors (m/s) at $t = 2e-04$ s [113].....	32
Figure 5.2 Fluid flow profile after 3s using different ultrasonic probe locations: (a) ultrasonic probe located at the top and (b) ultrasonic probe located at the top [115].....	33
Figure 5.3 Particles distributions after 3s using different injection positions and ultrasonic probe locations: (a) particles injected at the bottom (ultrasonic probe located at the top); (b) particles injected at the top (ultrasonic probe located at the top); and (c) particles injected at the bottom (ultrasonic probe located at the bottom) [115] .....	35
Figure 5.4 Distribution associated with the solidification after (a) 2 min and (b) 4 min [124]....	37
Figure 6.1 (a) SEM tensile fracture surface of the 6061/1% SiC nanocomposite (b) EDS (for the Spectrum position) on the tensile fracture surface of the 6061/1% SiC nanocomposite (c) EDS for the whole area on the tensile fracture surface of the 6061/1% SiC nanocomposite (d) EDS mapping result for Carbon (e) EDS mapping result for Aluminum.....	41
Figure 6.2 SEM pictures of tensile fracture surface for the two alloy samples processed under different conditions: (a) Ar degassed 6061 alloy casting at X100 and (b) Ar degassed 6061 alloy casting at X430 and (c) UST 6061 alloy casting at X100 (d) UST 6061 alloy casting at X430.....	43
Figure 6.3 SEM pictures of tensile fracture surface for the 6061 based nanocomposite samples processed under different melting conditions: (a) UST+1% SiC nanocomposite casting at	

X100 (b) UST+1% SiC nanocomposite casting at X430 (c) UST+1% Al <sub>2</sub> O <sub>3</sub> nanocomposite casting at X100 (d) UST+1% Al <sub>2</sub> O <sub>3</sub> nanocomposite casting at X430.....	45
Figure 6.4 SEM pictures of tensile fracture surface for the 6061 based nanocomposite samples at higher magnification: (a) UST+1% SiC nanocomposite casting at X10000 (b) UST+1% SiC nanocomposite casting at X37000 .....	46
Figure 6.5 SEM pictures of tensile fracture surface for the 6061 based nanocomposite samples at higher magnification: (a) UST+1% Al <sub>2</sub> O <sub>3</sub> nanocomposite casting at X10000 (b) UST+1% Al <sub>2</sub> O <sub>3</sub> nanocomposite casting at X33000.....	47
Figure 6.6 Tensile testing results for as-cast A356 samples.....	49
Figure 6.7 Tensile testing results for T6 heat treated A356 samples.....	49
Figure 6.8 Comparison of (a) as-cast degassed 6061 sample and (b) T6 heat treated sample .....	50
Figure 6.9 Tensile testing results for the as-cast 6061 samples.....	52
Figure 6.10 Tensile testing results for the T6 heat treated 6061 samples.....	53
Figure 6.11 T6 heat treated A356 degassed sample .....	53
Figure 6.12 Optical microscope pictures at X50 for A356 samples (a) without UST treatment and (b) with UST treatment during solidification.....	56
Figure 6.13 Optical microscope pictures at X50 for A356 samples reinforced with (a) UST + 1% SiC and (b) UST + 1% Al <sub>2</sub> O <sub>3</sub> .....	57
Figure 6.14 SEM results at X50 magnification for A356 samples reinforced with UST + 1% SiC during solidification: (a) SEM pictures (b) EDS mapping result for Al element (c) EDS mapping result for Si element (d) EDS mapping result for C element.....	59
Figure 6.15 EDS mapping results at X50 magnification for A356 samples reinforced with UST + 1% SiC during solidification: (a) Al (in green) and Si (in red) elements (b) Al (in green) and C (in red) elements (c) Al (in green), Si (in red) and C (in blue) elements .....	61
Figure 6.16 SEM results at X200 magnification for A356 samples reinforced with UST + 1% SiC during solidification: (a) SEM pictures (b) EDS mapping result for Al element (c) EDS mapping result for Si element (d) EDS mapping result for C element (e) EDS spectrum result .	63
Figure 6.17 EDS mapping results at X50 magnification for A356 samples reinforced with UST + 1% SiC during solidification: (a) Al (in green) and Si (in red) elements (b) Al (in green) and C (in red) elements (c) Al (in blue), Si (in green) and C (in red) elements .....	65

## CHAPTER 1 – INTRODUCTION

Ultrasonic stirring technology can be effectively used in commercial casting processes, *e.g.* direct-chill, shape and die casting due to its effects on microstructure of metals, which include control of grain structure, refinement of secondary phases, improvement of material homogeneity, and the uniform distribution of inclusions [1-9]. The existence of these effects is proven experimentally, and some of them are used in industry [10, 11].

Strong evidence shows that microstructure and mechanical properties of a casting product can be noticeably improved if nanoparticles are used as reinforcement to form MMNC. Aluminum matrix composites have the potential to offer desirable properties, including low density, high specific strength, high specific stiffness, excellent wear resistance and controllable expansion coefficient, which make them attractive for numerous applications in aerospace, automobile, and military industries. It is a promising approach to use nano-sized ceramic particles to strengthen MMNC, while maintaining good ductility [12, 13]. Currently, there are several fabrication methods of MMNC, including mechanical alloying with high energy milling [14], ball milling [15], nano-sintering [16], spray deposition, electrical plating, sol-gel synthesis, laser deposition, *etc.* The mixing of nano-sized ceramic particles is normally lengthy, expensive, and energy consuming.

In the present study, 6061/A356 nanocomposite castings are fabricated using the ultrasonic stirring technology (UST). The 6061/A356 alloy and  $\text{Al}_2\text{O}_3/\text{SiC}$  nanoparticles are used as the matrix alloy and the reinforcement, respectively. Nanoparticles are added into the molten metal and then dispersed by ultrasonic cavitation and acoustic streaming. Ultrasonic vibration

has been extensively used in purifying, degassing, and refinement of metallic materials [17-21], mainly because introducing the ultrasonic energy into a liquid will induce nonlinear effects such as cavitation and acoustic streaming.

The dispersion and deagglomeration of nanoparticles into liquids is an important application of ultrasonic devices. If powders are wetted, the nanoparticles build agglomerates and are held together by attraction forces of various physical and chemical nature, including van der Waals forces and liquid surface tension. The attraction forces must be overcome in order to deagglomerate and disperse the particles into liquid media. A uniform dispersion and deagglomeration is important to use the full potential of the particles. Especially nanoparticles offer extraordinary characteristics, which can only be exploited in a highly uniform dispersed state.

The application of stress generated by ultrasonic cavitation breaks the particle agglomerates apart. Also, liquid is pressed between the particles. Dispersion by ultrasonic is a consequence of microturbulences caused by fluctuation of pressure and cavitation. Ultrasonic cavitation is very effective in breaking agglomerates, aggregates and even primaries. Ultrasonic cavitation can create small-size transient domains that could reach very high temperatures and pressures as well as extremely high heating and cooling rates. The shock force that takes place during ultrasonic cavitation processing coupled with local high temperatures can break the nanoparticle clusters and clean the surface of the particles. Furthermore, ultrasonic vibration can improve the wettability between the reinforced nanoparticles and the metal matrix [22-24], which will assist to distribute the nanoparticles more uniformly into the metal matrix. Ultrasonic cavitation in liquids causes high speed liquid jets of up to 1000 km/h (approximately 600 mph). Such jets press liquid at high pressure between the particles and separate them from each other [25].

The applied UST parameters in the current experiments are used to validate a recently developed multiphase CFD model [26], which is capable to model the cavitation and nanoparticle dispersion during UST processing. The CFD model accounts for turbulent fluid flow, heat transfer and the complex interaction between the molten alloy and nanoparticles by using the ANSYS Fluent DDPM model.

$\text{Al}_2\text{O}_3$  and SiC are widely used as reinforcement particles due to their relatively good thermal and chemical stability. In this study, the effects of the ultrasonically dispersed  $\text{Al}_2\text{O}_3$  and SiC nanoparticles on the microstructure and mechanical properties of nanocomposite casting samples are studied.

Results of microstructure, mechanical behavior and mechanical properties of the nanocomposite castings have been also investigated. The current experimental results show that the tensile strength of the as-cast 6061 based nanocomposite samples (reinforced by  $\text{Al}_2\text{O}_3$  or SiC nanoparticles) increases slightly while the elongation increases significantly. The addition of the  $\text{Al}_2\text{O}_3$  or SiC nanoparticles in 6061 alloy matrix changes the fracture mechanism from brittle dominated to ductile dominated. The tensile strength of as-cast A356 samples increases after the UST treatment and addition of nanoparticles, and the elongation of these samples shows different changes.

The purpose of this study is to research the main five topics mentioned below. This study advances the state-of-the-art of the UST processing method and assists in research and development of new advanced materials, which have not been produced before by conventional methods.

1. UST is applied to the fabrication of aluminum based alloy and nanocomposites. Based on the literatures, the effects of UST on the processing are reviewed in detail. These effects include

degassing, refinement of the primary phase, modification of eutectic phase, dispersing of reinforcement nanoparticles, and improving of the wettability of nanoparticles.

2. A variety of types of nanoparticles are used as reinforcement nanoparticles such as  $\beta$ -SiC,  $\text{Al}_2\text{O}_3$ , ZrC, TiN,  $\text{TiB}_2$ , and multi-wall carbon nanotubes (MWCNTs). The optimum type and amount of nanoparticles are determined. The role of nanoparticles in the nucleation and the strengthening of the matrix are analyzed as well. The strengthening mechanisms are determined based on careful comparisons of microstructure and properties with and without nanoparticles.

3. In most of the proposed experiments, high superheat values similar to those used in the industrial practice have been applied. Also, several novel methods of adding nanoparticles into the molten alloys are investigated to better suit the requirements of the scale-up work of fabricating MMNC.

4. In another set of experiments, processing method of producing Al-based alloy and nanocomposites by using UST processing at low superheat is developed. Molten metal is treated during solidification process. Detailed metallurgical characterization of samples produced with this method is performed.

5. The applied UST parameters in the studied experiments are used to validate a recently developed multiphase CFD model, which is capable to model cavitation and nanoparticle dispersion during UST processing. A parametric study using this model has been performed and the results are used to further improve the proposed experimental methods.

## CHAPTER 2 – LITERATURE REVIEW

### 2.1 A356 and 6061 Alloys

Aluminum alloy A356 and 6061 are selected as the metal matrix because they are readily castable and widely studied. Typically A356 alloy is used to make aircraft pump parts, automotive transmission cases, aircraft fittings and control parts, water-cooled cylinder blocks and other applications where excellent castability, good weldability, pressure tightness, and good resistance to corrosion are required.

6061 alloy has good mechanical properties and exhibits good weldability. It is one of the most common used aluminum alloys for general purpose use. 6061 is commonly used for the following components: construction of aircraft structures, such as wings and fuselages, commonly in homebuilt aircraft than commercial or military aircraft, yacht construction, including small utility boats, automotive parts, such as wheel spacers, aluminum cans for the packaging of foodstuffs and beverages. 6061 is more easily worked and remains resistant to corrosion even when the surface is abraded.

The chemical compositions of the A356 and 6061 alloys are shown in Table 2.1.

Table 2.1 Nominal chemical composition of matrix alloys studied (in wt. %)

Matrix Alloy	Si	Fe	Cu	Mn	Mg	Zn	Ti	Balance
A356	6.5-7.5	0.20	0.20	0.10	0.25-0.45	0.10	0.20	Al
6061	0.4-0.8	0.70	0.15-0.4	0.15	0.8-1.2	0.25	0.15	Al

### 2.2 Metal-Matrix-Composites vs. Metal-Matrix-Nanocomposites

Micrometer-size particles are commonly chosen as reinforcement because of their low cost and easy availability. Mechanical properties such as hardness and modulus can be

significantly improved with micrometer-size particles reinforcement [27-29]. However, micrometer-size particles reinforced metal matrix composites are usually faced with the problem of low ultimate tensile strength and ductility due to particle fracture and particle/matrix interfacial failure [30, 31]. Particulate-reinforced metal-matrix-composite (MMC), particularly aluminum-based matrix composites have been used extensively as structural materials especially in automotive and railway industries [32]. SiC particulate-reinforced Al-based composites have been employed for the ventral fins and fuel access door covers on the F-16 aircraft as well as for rotor blade sleeves on the Eurocopter EC120 and N4 helicopters [33, 34]. However, the size of ceramic particulates of Al-based composites is large, typically at the order of micrometers or tens of micrometers. Large ceramic particulates are prone to cracking during mechanical loading, leading to premature failure and low ductility of the composites. Particulate size has a strong effect on the failure mode, strength, and ductility of the Al-based composites. Both tensile strength and ductility decrease with increasing particle size [35]. Therefore, decreasing the ceramic particulate size can lead to substantial improvements in mechanical performance of MMC, *e.g.* enhanced strengthening and reduced particle cracking. The mechanical properties of MMC can be further enhanced by decreasing the size of ceramic particulates and matrix grains from micrometer to nanometer level [36-42]. Such materials are referred to as the nanocomposites. The size of matrix grains can be refined to submicrometer or nanometer regime using severe plastic deformation and mechanical alloying processes [43, 44].

To overcome these limitations, and to look for further improvement in mechanical properties, nano-size reinforcements are studied. Nano-size reinforcements are perceived to be able to impart excellent properties to the metal matrix at a much reduced amount of reinforcement material. In recent study [45], a simultaneous increase in 0.2% yield strength,

ultimate tensile strength and ductility was found for the Mg–CNT nanocomposites, until a threshold of 1.3 wt. % was reached. The increase in tensile strength up to an addition of 1.3 wt. % CNT is due to the restriction of dislocation movement by the CNT. It has been previously shown that the presence of reinforcements can produce a slip mode transition depending on the reinforcement/matrix interaction. Cross slip in non-basal slip planes may be activated by the presence of CNT which is responsible for the increased ductility observed in the present study. Addition of more than 1.3 wt. % CNT results in deterioration of mechanical properties due to an increase in porosity from the source of clusters of CNT.

The greatest challenges facing the development of MMNC for wide application are the cost of nano-size reinforcements and the complexity of synthesis and processing of nanocomposites using current methods [46]. For conventional metal matrix composites with micron-scale reinforcements, the mechanical properties of MMNC are strongly dependent on the properties of reinforcements, the distribution and the volume fraction of the reinforcement as well as on the interfacial strength between the reinforcement and the matrix. Due to their high surface area, nano-size powders and nanotubes will naturally tend to agglomerate to reduce their overall surface energy, making it difficult to obtain a uniform dispersion by most conventional processing methods. In addition, due to their high surface area and surface dominant characteristics, these materials may also be highly reactive in metal matrices. For example, in Al/CNT composites there are concerns that brittle aluminum carbide phases could form during processing, impairing the mechanical properties and electrical conductivity of the nanocomposites. Because of these concerns, processing methods are being developed to produce MMNC with uniform dispersions of nanoparticles and little deleterious interfacial reactions.

It has been reported [36] that the tensile strength of Al-1.0 vol. %  $\text{Si}_3\text{N}_4$  (15 nm diameter) nanocomposite is comparable to that of Al-15.0 vol. % SiC (3.5  $\mu\text{m}$  diameter) composite, with the yield stress of the  $\text{Si}_3\text{N}_4$  nanoparticle reinforced MMNC being significantly higher than that of the SiC strengthened MMC. Mg-based nanocomposites can exhibit even higher tensile strength and ductility than their MMC counterparts.[40] This is especially important for structural applications in which high tensile strength and ductility are essential.

In another study [47], several volume fractions of nano-size and micro-size  $\text{TiB}_2$  powders were incorporated into molten aluminum A356 alloy via stir casting method to fabricate A356/ $\text{TiB}_2$  nanocomposites and microcomposites. The effects of particle size and volume fraction of reinforcement powders on porosity content, tensile strength, elongation, toughness and fracture behavior of samples were investigated. The porosity content increased with the increasing volume fraction of reinforcements and the decrease of the particle size. The significant improvements in tensile strength and toughness were obtained when 1.5 vol. %  $\text{TiB}_2$  nanoparticles were introduced into the A356 alloy; further increase in nanoparticle content led to the reduction in the strength values of the matrix. The processed nanocomposites showed higher ductility and toughness compared with those processed using micron size particles. This can be related to superior quality of particle/matrix bonding in the nanoparticle reinforced samples. The highest toughness and total strain were observed in the 1.5 vol. %  $\text{TiB}_2$  nanocomposites.

### 2.3 Effects of Ultrasonic Stirring

UST has been extensively used in purifying, degassing, and refinement of metallic materials [17-21, 48], mainly because introducing the ultrasonic energy into a liquid will induce nonlinear effects such as cavitation and acoustic streaming [11, 18, 49-66]. Ultrasonic cavitation can create small-size transient domains that could reach very high temperatures and pressures as

well as extremely high heating and cooling rates. These pressure and temperature fluctuations are likely to induce heterogeneous nucleation in the melt [17]. They are also likely to promote dendrite fragmentation by enhancing solute diffusion through acoustic streaming [67-71].

The main effects of the UST processing are discussed below:

UST induced degassing: during the cavitation process, very small bubbles are created at low pressure. These bubbles can act as nuclei for the formation of hydrogen and vapor bubbles. Hydrogen will escape from the liquid. The degassing efficiency is proportional to the ultrasonic intensity.

Grain nucleation: there are several ways that UST can alter grain nucleation. Since the pressure oscillations exist in a melt under UST processing, the liquidus temperature for the melt is changed. Thus, some part of the melt is superheated and the other part is undercooled. This phenomenon occurs at high frequencies and causes increase in the amount of nuclei into the melt [60, 72].

Dendrite fragmentation: dendrites usually start melting at the root due to local temperature rise and segregation. In the melt, UST produces strong convection and shock waves which may promote dendrite fragmentation. Convection can promote dendrite fragmentation because it causes local temperature and composition variations and promotes diffusion of solute. Shock waves will induce the breakage of the melting root [70, 71].

In previous study [6], through the comparison of UST treated A356 samples and non-UST A356 samples, it showed that the UST has significantly positive effects on casting components. The effects include microstructure refinement, eutectic modification, and high level of hydrogen degassing.

Several recent studies revealed that ultrasonic cavitation processing was highly efficient in dispersing nanoparticles into a molten metal melt [73]. Based on these studies [2, 3, 5, 7], SiC nanoparticles were well dispersed into the A356 matrix. It also showed that some agglomeration had occurred during the MMNC processing. EDS analysis was also performed, and a uniform dispersion of SiC nanoparticles could be observed from EDS mapping result.

Mechanical stirring is also widely used to mix particles into the melt. However, when the stirring stopped, the particles tended to return to the surface and most of these particles still stuck to each other as clusters/agglomerates. This could be caused by the nanoparticles being surrounded by surface gas layers. Definitely, the phenomena involved in the ultrasonic dispersion of nanoparticles are fundamentally different from the conventional mechanical stirring related phenomena. The major difference lies in the acoustic transient cavitation, which induces a violent collapse of micro gas bubbles around the nanoparticle clusters, thus breaking the clusters and dispersing the nanoparticles into the matrix. Moreover, the transient cavitation could remove the gas layer from the surface of the nanoparticles, thus improving the wettability between the nanoparticles and matrix significantly [22-24].

Investigations on Al - 2 wt. % Al<sub>2</sub>O<sub>3</sub> nanocomposite using optical, scanning and transmission electron microscopes [74] revealed that the nanocomposite was a “super-composite” of nearly continuous nano-alumina dispersed zones (NDZs) enveloping the Al<sub>2</sub>O<sub>3</sub> depleted zones (ADZs). The NDZs were 200 - 300 nm wide and situated mostly near the grain boundaries. The NDZs had a dense dispersion of nano-sized (10 nm) Al<sub>2</sub>O<sub>3</sub> particles with an average inter particle spacing of 24 nm. Analysis of the dense dispersion regions might help us to understand the strengthening mechanism and the interaction between the metal matrix and the nanoparticles. Other researchers also found that in current MMNC fabrication processes, a

boundary effect often occurred where the nanoparticles tended to gather around the grain boundaries of the metal matrix. The nanocomposite matrix used in another study [75] was made of 99.8% (weight) aluminum and 0.2% titanium. 1% aluminum oxide nanoparticles were added into the alloy. Two indices for quantifying the degree of boundary effect in an image, called Boundary Indices (BIs), were developed and validated on the samples.

In the studies mentioned above [73, 74], UST treatment effectively dispersed the nanoparticles into the metal matrix. However, some agglomeration and floating of nanoparticles were still observed. To minimize the agglomeration and eliminate the floating issue of the nanoparticles, some novel methods of adding nanoparticles are applied in present study to assist the UST method.

#### 2.4 Novel Fabrication Methods of Nanocomposites

For composites prepared by the conventional liquid metallurgy route, severe agglomeration of nanoparticles frequently occurs even when mechanical stirring is applied before casting. This is due to poor wettability and high viscosity generated in the molten metal owing to high surface-to-volume ratio of the nano-sized ceramic particles. The density of nanoparticles typically does not play an important role in the production of nanocomposites. Such small particles are supposed to float on the top of the molten bath even if their density is relatively higher than that of the liquid matrix. This issue is indeed of paramount importance in micron-sized particle reinforced composites but it is thought that in nano-reinforced materials, other effects such as those induced by extensive surface tension could play a more important role [76].

The AZ31 Mg-based nanocomposites reinforced with nano-sized  $\text{Al}_2\text{O}_3$  particles were successfully fabricated via FSP (friction stir processing) using threaded probe tools [77]. The

$\text{Al}_2\text{O}_3$  particles distribution was improved with the number of FSP passes. Breaking the “onion-ring” shaped agglomeration formed at the previous FSP pass and further separation of the nanoparticle agglomeration resulted in improved nanoparticle distributions. Also, as rotational speed increased, the nanoparticle agglomeration size of alumina nanoparticles decreased due to increase in material flow in the stir zone.

Mechanical alloying (MA) is well recognized as a potential method for achieving better dispersion of reinforcing particles in the matrices of microncomposites and nanocomposites [37, 78-81]. MA approach allows the formation of nanocomposites via mechano-chemical milling powders of metal, oxide and carbide in various combinations. The process involves repeated plastic deformation, welding and fracture of particles. Several factors such as miller type, ball to powder weight ratio, ball material, milling atmosphere, process control agent, etc., can influence the stage of milling [81]. When welding and fracture mechanism reach equilibrium, equiaxed particles with randomly oriented interfacial boundaries may be formed. In order to suppress the recovery and recrystallization of the matrix grains, the precursor powders are milled in liquid nitrogen to obtain a nanostructure. This technique is commonly referred to as the cryo-milling [78, 79, 82, 83].

Ball milling and mechanical stirring were used to improve the dispersion acting as pre-mix procedures in another study [84-89]. It is extremely challenging for mechanical stirring method to distribute and disperse nanoparticles uniformly in molten metal because of the poor wettability and higher specific surface areas of nanoparticles, which may lead to agglomeration and clustering, especially in the case of alumina in molten aluminum [85]. Recently, it was reported [86-89] that the mixing of ceramic reinforcement with aluminum powders by milling process might lead to an increase in the wettability of ceramic materials with molten aluminum.

Mixtures of fine Al powders and alumina nanoparticles were ball-milled in a high-energy planetary ball mill. Then the mechanical stirring would improve the uniformity of nanocomposite slurry. The use of solid-state processing methods such as mechanical alloying [81, 90-92] permitted the development of nanocomposite materials having large volume fraction of nano-size reinforcement phase homogeneously dispersed in a nanostructure matrix. The MA powders are generally fully densified by hot consolidation such as hot pressing, hot isostatic pressing (HIP) or extrusion.

The use of conventional sintering methods such as hot pressing, high-temperature extrusion, and hot isostatic pressing to consolidate these materials often results in grain growth, which affects the properties of the end product. Preventing or at least minimizing grain growth to maintain the nanostructure features of the matrix is possible through careful control of consolidation parameters, particularly heating rate, sintering temperature, and time. In this regard, spark plasma sintering (SPS), also known as field assisted sintering (FAST), has been shown to be an effective non-conventional sintering method for obtaining fully dense materials [93, 94]. In this work [95], the spark plasma sintering process was presented and recently published work on spark-plasma-sintered metals and metal matrix nanocomposites was reviewed as well. The spark plasma sintering process has been shown to be an effective technique for consolidating metallic materials including nanocomposites. The advantages of spark plasma sintering include high heating rates, short sintering cycles, and low sintering temperatures.

In another study [96], microwave heating was employed for the sintering of pure aluminum and magnesium based composites that were prepared using the powder metallurgy technique. Three different types of reinforcements displaying different behaviors with the microwaves were selected: (1) a microwave absorbing material (SiC), (2) a microwave

transparent material ( $\text{Al}_2\text{O}_3$ ) and (3) a metallic conducting material (Cu). Mechanical characterization revealed an increase in hardness, 0.2% YS and UTS of magnesium with the addition of nanoparticle reinforcements. Failure strain was improved with the addition of SiC and  $\text{Al}_2\text{O}_3$  ceramic reinforcements but displayed the opposite trend with the addition of metallic copper as reinforcement.

The methods that have been used to synthesize metal matrix nanocomposites include powder metallurgy, deformation processing, vapor phase processing, and in some cases solidification processing [46]. Powder metallurgy involves the preparation of blends of powders of metal and reinforcements, followed by consolidation and sintering of the mixtures of powders to form the part. Deformation processing involves subjecting a metal to high rates of deformation to create nanostructure grains in a metal matrix. Vapor phase processing methods such as chemical vapor deposition (CVD) can be used to deposit thin films creating dispersed multiphase microstructures, multilayered microstructures, or homogeneous nanostructure coatings. Each of these methods can create very desirable microstructures, however they are expensive and difficult to scale up to manufacture large and complex shapes in bulk.

From all processing methods available for synthesis and processing of MMNC, the least expensive method for production of materials in bulk is solidification processing. There are various methods by which researchers have created nanostructures and nanocomposite materials using solidification and these can be divided into three categories: (1) rapid solidification, (2) mixing of nano-size reinforcements in the liquid followed by solidification and (3) infiltration of the liquid into a preform that contains the reinforcement followed by solidification.

Rapid solidification (implying solidification rates of up to  $10^4$ – $10^7$  °C/s) through methods such as melt spinning (a liquid metal stream is impinged onto a spinning copper drum),

or spray atomization (a superheated liquid metal is atomized with gas jets and impinged onto a substrate) can lead to nano-size grains as well as amorphous metals from which nano-size reinforcements can be precipitated in the amorphous matrix during heating to form nanocomposites [97]. Mixing techniques involve adding particulate reinforcements and mechanically dispersing them into the matrix. Mixing methods that have been applied to synthesize MMNC include stir mixing, where a high temperature impeller is used to stir a melt that contains reinforcements, creating a vortex in the melt, and ultrasonic mixing, where an ultrasonic probe is used to create cavitation in the melt that disperses the particulate reinforcements by an acoustic streaming effect that occurs through the collapse of bubbles within the melt. Infiltration techniques entail infiltrating a preform or partial matrix containing the reinforcements with a liquid metal. The preform consists of particles formed in a particular shape with some binding agent, and can be composed of the additives and binding agent alone or with some portion of the matrix added as a partial filler. Infiltration methods that have been used include ultra-high pressure, where the pressure used to infiltrate a high-density preform of nanoparticles is in excess of 1 GPa, and pressureless infiltration, where a block of metal is melted on top of a lower density preform of nanoparticles and allowed to seep into the preform [98].

Disintegrated Melt Deposition (DMD) is a liquid metallurgy process successfully employed for production of nanocomposites. Alumina nanoparticles have been well dispersed in Al–Mg alloys by heating the metal in argon atmosphere and adding the ceramic particles by means of a vibratory feeder. The melt was stirred and poured, then disintegrated by argon gas jets and deposited onto a metallic substrate. Finally, the MMNCs were extruded to reduce porosity down to very low levels and to achieve a good dispersion of the particles [99, 100].

Selective laser melting (LSM) was also used to fabricate Ti-based nanocomposites [101]. Powders were milled by high-energy ball milling and then melted by laser beam under protective atmosphere. Through this method, a unique structure very different from the initial structure of the reinforcement was achieved. A proper decrease in the volumetric energy density led to the development of TiC whisker and of uniformly dispersed nano-lamellar TiC, which grew epitaxially from a dendritic TiC. The same research confirmed that well dispersed nano-particles induced improved mechanical and wear properties to the Ti matrix. Melt stirring, high-pressure die casting [102] and arc-discharge plasma method [103] were also used to produce AZ91/CNT composites and in situ Al/AlN MMNC, respectively.

Li *et al.* [104] successfully dispersed MWCNTs on Mg alloy chips, and then the chips were added to the melt with vigorous stirring. They found a significant improvement up to 36% in compressive yield strength and ultimate compressive strength only by addition of 0.1 wt. % MWCNTs. Abbasipour *et al.* [105] produced 356 aluminum alloys reinforced with CNTs by stir casting and compocasting routes. In order to alleviate problems associated with poor wettability, agglomeration, and gravity segregation, CNTs were introduced into the melts by injection of CNTs deposited aluminum particles instead of raw CNTs. Aluminum powder particles with a mean diameter of 100  $\mu\text{m}$  were first deposited by CNTs using Ni-P electroless plating technique and then added into the melt agitated by a mechanical stirrer. The slurry was subsequently cast at a temperature corresponding to full liquid, 0.15 and 0.30 solid fractions. The results showed that the addition of CNTs to A356 matrix could significantly refine both full liquid and semisolid cast microstructures. Hardness of the samples were significantly increased by the addition of CNTs and A356-CNT composite cast at a solid fraction of 0.3.

In another study [106], A356 alloys matrix composites reinforced by different contents of MWCNTs were fabricated. A novel approach by adding Al/MWCNTs ingot into the molten A356 aluminum alloy was performed. This method was significant in de-bundling and preventing flotation of the CNTs within the molten alloy. The results indicated that a significant improvement in ultimate tensile strength and elongation of the nanocomposite occurred at the optimal amount of 1.5 wt. % MWCNTs, which represented an increase in their values by a ratio of about 50% and 280%, respectively.

## 2.5 Strengthening Mechanisms

The outstanding mechanical performance of MMNCs is the result of several strengthening mechanism contributions, namely: load transfer effect, Hall-Petch strengthening, Orowan strengthening, coefficient of thermal expansion (CTE) and elastic modulus (M) mismatch [107-110]. In the following sections, each strengthening method is discussed separately.

### 2.5.1 Load Transfer Effect

The load transfer from the soft and compliant matrix to the stiff and hard particles under an applied external load contributes to the strengthening of the base material. A modified Shear Lag model proposed by Nardone and Prewo [111] is commonly used to predict the contribution in strengthening due to load transfer in particulate-reinforced composites for the case of spherical particles [107-109]:

$$\Delta\sigma_{LT} = \frac{1}{2} v_p \sigma_m \quad [1]$$

where  $v_p$  is the volume fraction of the particles and  $\sigma_m$  is the yield strength of the unreinforced matrix.

### 2.5.2 Hall-Petch Strengthening

The grain size has a strong influence on metal strength since the grain boundaries can hinder the dislocation movement. This is due to the different orientation of adjacent grains and to the high lattice disorder characteristic of these regions, which prevent the dislocations from moving in a continuous slip plane [112]. The Hall-Petch equation relates the strength ( $\Delta \sigma_{HP}$ ) with the average grain size ( $d$ ) [112]:

$$\Delta \sigma_{HP} = \frac{k_y}{\sqrt{d}} \quad [2]$$

where  $k_y$  is the strengthening coefficient (characteristic constant of each material). The type and size of particles play a fundamental role in the final grain size of the nanocomposites since they can interact with grain boundaries acting as pinning points, retarding or stopping their growth. The increase of  $v_p$  (volume fraction) and the decrease of  $d_p$  (particle diameter) lead to a finer grain structure ( $d_m$ ), as theoretically modeled by Zener equation [109]:

$$d_m = \frac{4\alpha d_p}{3v_p} \quad [3]$$

where  $\alpha$  is a proportional constant.

### 2.5.3 Orowan Strengthening

The Orowan mechanism consists in the interaction of nanoparticles with dislocations. The non-shearable ceramic reinforcement particles pin the crossing dislocations and promote dislocations bowing around the particles (Orowan loops) under external load [112].

#### 2.5.4 CTE and M Mismatch

The mismatch in the coefficient of thermal expansion (CTE) and in the elastic modulus (M) between the reinforcements and the metal matrix is accommodated during material cooling and straining by the formation of geometrically necessary dislocations (GNDs) [109].

#### 2.6 Modeling of Ultrasonic Cavitation and Nanodispersion Phenomena during Molten Metal and Solidification Processing

To assist in the development of the UST processing as well as in the optimization and scale up of the UST method, a comprehensive modeling tool is required. Modeling and simulation of casting solidification of alloys with UST requires complex multi-scale computations, from computational fluid dynamics (CFD) macroscopic modeling through mesoscopic to microscopic modeling, as well as strategies to link various length-scales emerged in modeling of microstructure evolution [26, 113]. The CFD analysis tool is required to model acoustic streaming, ultrasonic cavitation and nanodispersion phenomena [26, 114, 115].

The common benefits of applying ultrasonic include (i) significant improvement of the casting quality; (ii) power consumption reduction, and (iii) decreasing considerably the production process time. There are a significant number of potential applications of ultrasonic to fields in life sciences, physics, chemistry and engineering. The most promising ultrasonic applications are in agriculture, food and light industries, goods manufacturing, biotechnology, metallurgy, mineral processing, environmental protection, medicine and energy systems areas [26].

Relevant metallurgical applications of UST include structural refinements of solidifying metals with applications to continuous casting and remelting processes (*e.g.*, vacuum arc remelting (VAR), electroslag remelting (ESR), electron beam remelting (EBR) and plasma arc melting (PAM)) for Ti alloys, specialty steels and superalloys.

An example of predicted solidification structure [113] with and without UST is shown in Figure 2.1, where  $G_E$  is the equiaxed grain density. The legend in Figure 2.1 shows the 256 color indexes ( $CI$  varies from 0 to 255) (legend displays 16 classes, where each class contains 16 different color indexes) used for displaying the preferential crystallographic orientation angle ( $\theta_i$ ). The columnar-to-equiaxed transition (CET) is observed in Figure 2.1 (a), where the UST is not applied. As it can be seen from Figure 2.1 (b), there is no CET zone under UST condition and the predicted equiaxed grain size is about 200  $\mu\text{m}$ , which is in good agreement with the experimental results presented here and in references [1, 6, 20]. The simulation results shown in Figure 2.1 (c) are obtained assuming a lower superheat of about 10  $^{\circ}\text{C}$ , which is significantly lower than the standard high superheat case of about 140 $^{\circ}\text{C}$  presented in Figure 2.1 (b). As shown in Figure 2.1 (d), the addition of the SiC nanoparticles further enhances the cavitation-induced heterogeneous nucleation phenomenon, which is the main mechanism for grain refinement in A356 alloy [116].

It is very difficult to obtain uniform dispersion of nano-sized ceramic particles in liquid metals due to high viscosity, poor wettability in the metal matrix, and a large surface-to-volume ratio, which result in agglomeration and clustering [73, 115]. ANSYS Fluent Dense Discrete Phase Model (DDPM) [117] was adapted in reference [114] to study the nanodispersion during UST processing of Al-based nanocomposites. The DDPM accounts for turbulent fluid flow, heat transfer, and the complex interaction between the molten alloy and nanoparticles.

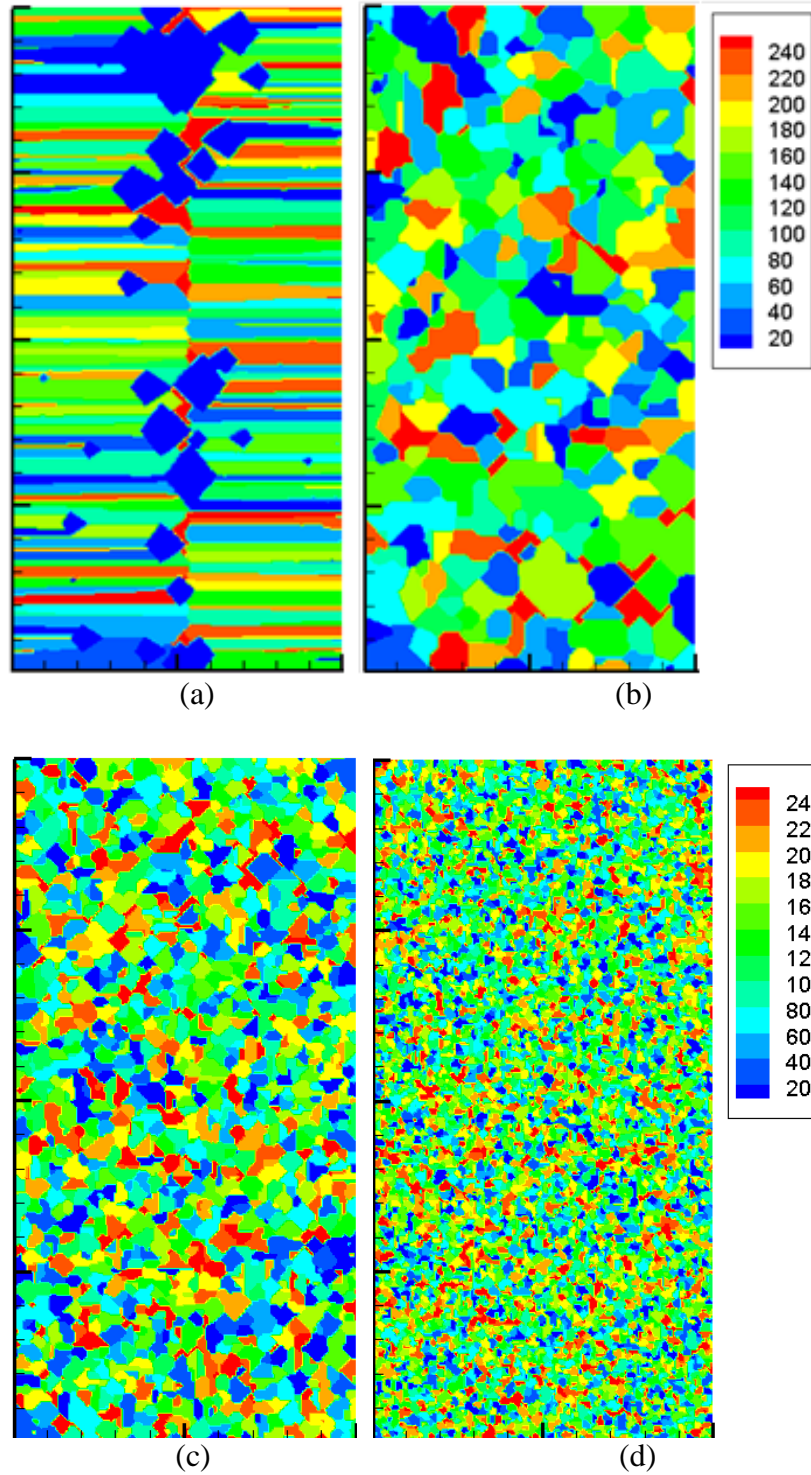


Figure 2.1 Ultrasonic treatment: prediction of the solidification structure for an A356 alloy (2 mm x 4 mm test geometry): (a) without UST ( $G_E = 5 \times 10^7$  nuclei/m<sup>2</sup>); (b) with UST and high superheat ( $G_E = 5 \times 10^8$  nuclei/m<sup>2</sup>); (c) with UST and low superheat ( $G_E = 5 \times 10^9$  nuclei/m<sup>2</sup>) and (d) with UST, low superheat and 1% SiC nanoparticles ( $G_E = 5 \times 10^{10}$  nuclei/m<sup>2</sup>) [113]

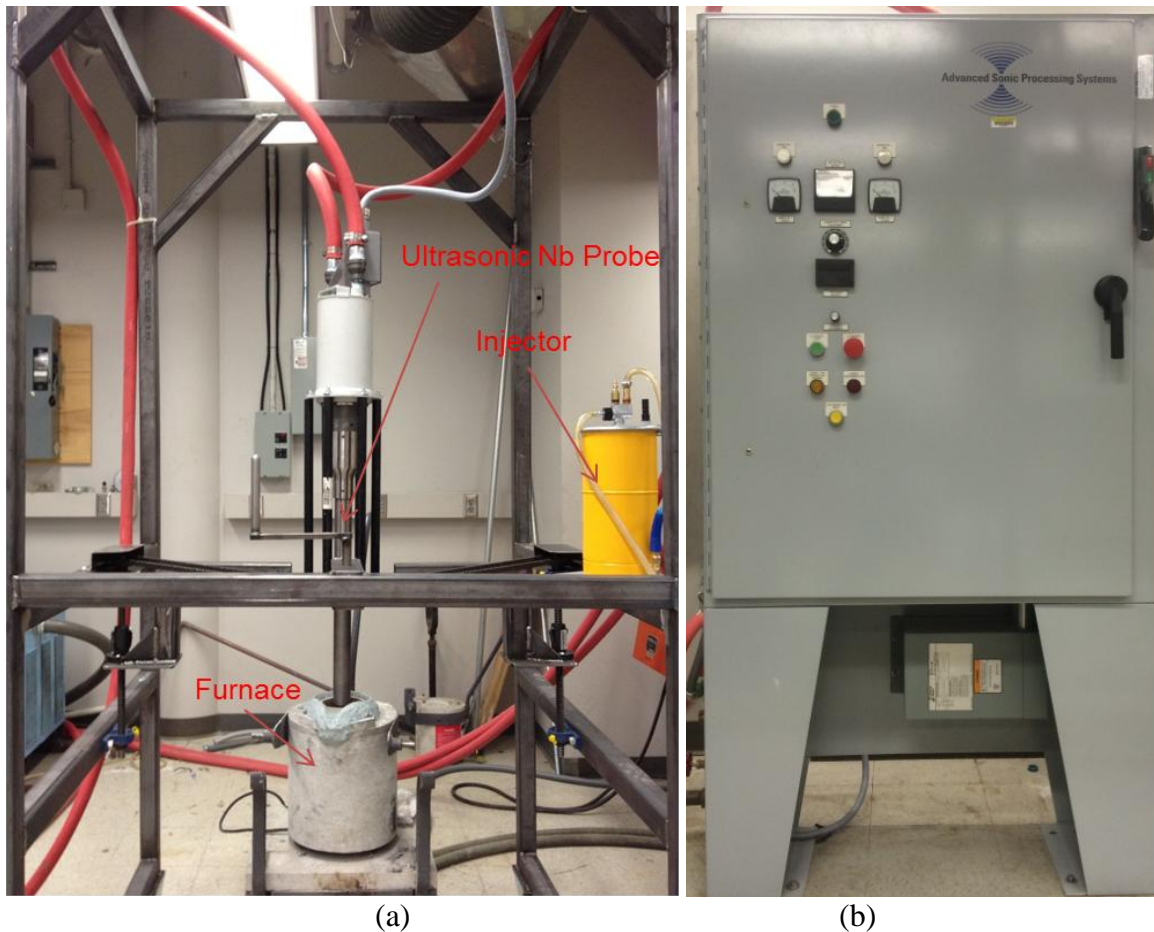
The dispersion of SiC nanoparticles with different injection positions and probe locations are investigated in detail in [114]. Their results revealed the following 4 major conclusions [114]: (1) the particles are dispersed reasonably well in the liquid pool (2) The injection positions do not affect the final distribution of the SiC nanoparticles as long as the flow is strong enough to disperse the particles; (3) When the ultrasonic probe is positioned at the bottom of the furnace, that is, the gravity direction is reversed, the nanoparticles have typically a different distribution due to a new flow pattern and (4) when the flow is stronger, the dispersion of the particles is faster; however, the uniformity of the fluid flow rather than the intensity of the fluid flow is critical to the final distribution of the nanoparticles.

## CHAPTER 3 – EXPERIMENTAL APPROACH

Aluminum alloy A356 and 6061 are selected as the metallic matrix because they are widely used. The ceramic nanoparticles used in this study are  $\beta$ -SiC (spherical shape, average diameter of 55nm),  $\text{Al}_2\text{O}_3$  (spherical shape, average diameter of 20 nm), ZrC (cubic shape, average diameter of 20 nm), TiN (average diameter of 20 nm),  $\text{TiB}_2$  (average diameter of 25 nm) and MWNTs (average diameter of 20nm).

The ultrasonic processing system used in this study is illustrated in Figure 3.1. It includes the generator, Nb ultrasonic probe, injector, induction furnace and the ASTM B108-02 standard metal mold. The main parameters of the ultrasonic equipment are as follows: maximum power,  $P=2.4$  kW and frequency,  $f=18$  kHz. An induction furnace with a capacity of 2.7 kg is used to melt the aluminum-based alloys and nanocomposites. After the alloy is melted, the ultrasonic probe is inserted to about 50 mm beneath the melt surface to perform ultrasonic stirring at 1.75 kW power and 18 kHz frequency. 1 wt % of nanoparticles are added into the cavitation region (which is located beneath the ultrasonic probe) during a 15 min time-frame. The molten pool is protected by Argon gas atmosphere. A thermocouple is used to monitor the melt temperature to control the superheat. A higher pouring temperature of  $750^\circ\text{C}$  is used to avoid the formation of metal-mold filling defects including cold-shuts during mold filling. The metal mold is preheated to  $400^\circ\text{C}$ . The specimen are extracted from the metal mold after 30 min and tested on a tensile test machine. The dimensions of the specimen are 50.8 mm length and 12.7 mm diameter. The experiments are repeated several times for statistical interpretation of the results.

Another set of experiments applying UST treatment during solidification are performed to better understand the effects of UST with and without nanoparticles on the solidification microstructure. The base experiment is done by melting the A356 alloy and turning off the furnace to let the molten metal solidify. The UST experiment is done by melting the A356 alloy and turning off furnace, and then during solidification, treating the molten alloy with UST for 4 min. The UST with nanoparticles (1%  $\text{Al}_2\text{O}_3$  or 1% SiC) experiments are performed by melting the A356 alloy, adding the nanoparticles (1%  $\text{Al}_2\text{O}_3$  or 1% SiC) assisted by UST for 15 min, turning off furnace, and then during solidification, treating the molten alloy with UST for 4 min.





(c)

Figure 3.1 UST equipments: (a) ultrasonic probe, injector and induction furnace (b) generator and (c) ASTM B108-02 standard metal mold

## CHAPTER 4 – MODELING APPROACH

Modeling tools are being applied to assist in the development of the experimental procedures. Two numerical modeling tools, which are developed in the Solidification Lab at the University of Alabama, are used in the current study as follows:

- 1) UST Cavitation Model
- 2) Nanodispersion Model

These models are summarized as below.

### 4.1 CFD Ultrasonic Cavitation Model

Fully couple energy, mass, acoustic, and compressible fluid flow models are developed to perform ultrasonic cavitation modeling [26, 113, 116, 117]. The Noltingk–Neppiras model, which is a general case of a gas vapor–filled cavity in an acoustic field, is used to predict the cavity time evolution in an acoustic field. The UST modeling approach is thus capable to model acoustic streaming, cavitation and bubble dynamics during molten metal and solidification processing of alloys.

Figure 4.1 describes the geometry of the A356 liquid pool. Since the time-domain computations are used for resolving the acoustic field, a very small time step on the order of  $1e-07$  s was used. The ultrasonic probe has a diameter of 50 mm, an amplitude,  $A = 10$  microns, and a frequency,  $f = 18$  kHz [1, 6]. The applied effective power of the ultrasonic generator is 1.7 kW.

In the ultrasonic cavitation model, a two-phase cavitation model is used, which consists of using the standard viscous flow equations governing the transport of phases (Eulerian multi-

phase) and the k- $\epsilon$  turbulence model. In cavitation, the liquid-bubble mass transfer is governed by the cavity (bubble) transport equation [26, 113, 116]:

$$\frac{\partial}{\partial t}(f_b \rho_b) + \nabla \cdot (f_b \rho_b \vec{V}_b) = R_G - R_C \quad (1)$$

where  $b$  subscript denotes the cavitation bubble phase,  $f_b$  is the bubble volume fraction,  $\rho_b$  is the bubble density,  $\vec{V}_b$  is the bubble phase velocity,  $R_G$  and  $R_C$  are the mass transfer source terms related to the growth and collapse of the cavitation bubbles, respectively.

In Eq. (1), the interphase mass transfer rates per unit volume ( $R_G$  and  $R_C$ ) account for the liquid and bubble phases in cavitation. They are calculated using the growth of a single bubble based on the Rayleigh-Plesset model [26]. The model assumes no barrier for nucleation; thus, the bubble dynamics can be obtained from the general Rayleigh-Plesset equation as follows [26, 116]:

$$R_b \frac{d^2 R_b}{dt^2} + \frac{3}{2} \left( \frac{dR_b}{dt} \right)^2 = \frac{p_b - p}{\rho_L} - \frac{2 \sigma_L}{\rho_L R_b} - \frac{4 \nu_L}{R_b} \frac{dR_b}{dt} \quad (2)$$

where  $R_b$  is the bubble radius,  $\sigma_L$  is the surface tension coefficient of the liquid phase,  $\rho_L$  is the liquid density,  $\nu_L$  is the kinematic viscosity of the liquid phase,  $p_b$  is the bubble surface pressure, and  $p$  is the local far-field pressure.

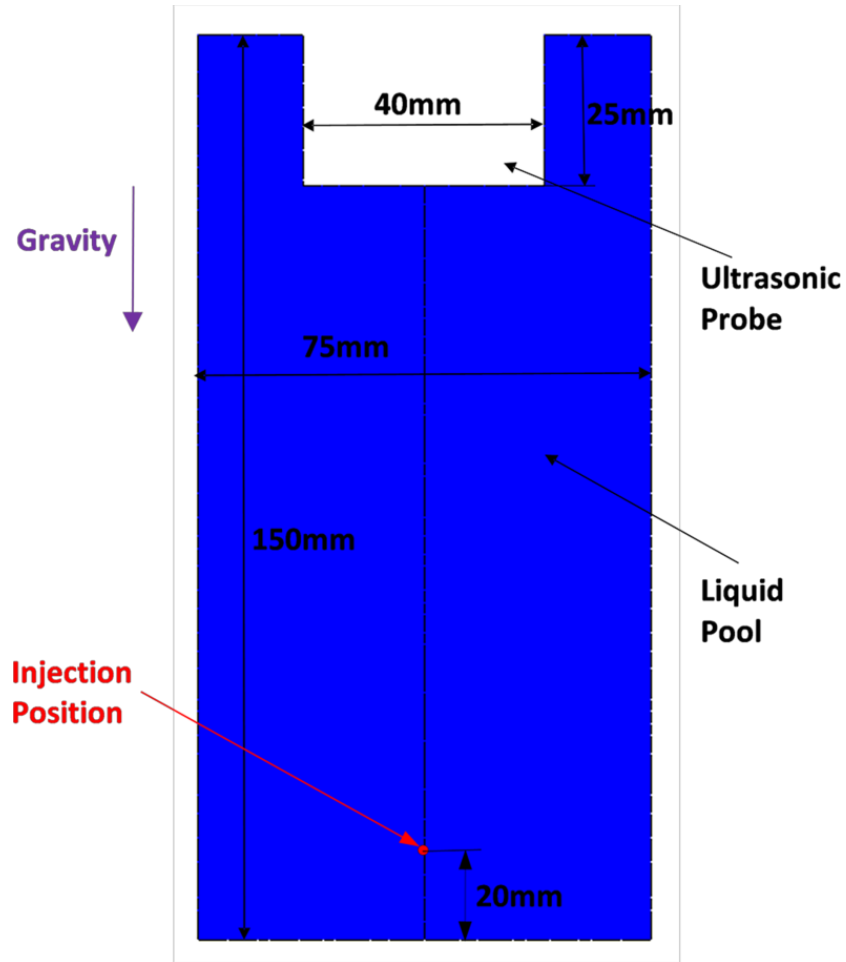


Figure 4.1 Model geometry

#### 4.2 CFD Nanodispersion Model

The geometry of the model is shown in Figure 4.1. The ultrasonic probe has a diameter of 40 mm. The Al alloy has a density of  $2700 \text{ kg/m}^3$  and a viscosity of  $1.0 \times 10^{-3} \text{ kg/(m-s)}$ . The SiC nanoparticles with an average particle size of 55 nm and density of  $3216 \text{ kg/m}^3$  are treated as inert-particles. The mass flow rate of the SiC nanoparticles is 0.014 kg/s. Thus, 1.0 wt. % of SiC nanoparticles can be added at about 20 mm above the bottom of the furnace for 1.0 sec.

By using ANSYS Fluent DDPM and  $k - \omega$  turbulence models, the multiphase CFD model can account for turbulent fluid flow, heat transfer, and the complex interaction between the

molten alloy and the nanoparticles. The CFD modeling equations and procedure are described in detail in [115].

The solution procedure is summarized next. The SiC nanoparticles are added at every fluid flow time step with a mass flow rate of 0.014 kg/s in the first second. The distribution of the particle diameters varying from 45 nm to 65 nm follows the Rosin-Rammler expression. Particles are tracked at every time step after the fluid velocity field is solved. Because of the low volume fraction of the discrete phase, one-way coupling is employed, which neglects the effect of the discrete phase on the fluid turbulence. The boundary conditions used in the simulations are described in the following paragraph.

The ultrasonic probe surface is set as velocity inlet, and the interface between liquid aluminum and air is pressure outlet. The other boundaries are set as wall. All of the discrete phase boundary condition types are set as fully reflective. The velocity inlet profile is defined in a user defined function (UDF), which is dependent on time as shown in Figure 4.2:

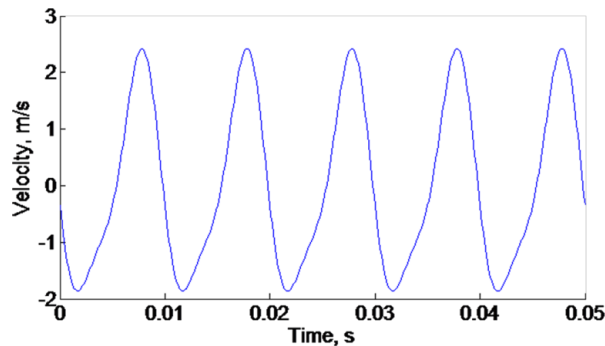


Figure 4.2 Velocity inlet profile

Ultrasonic cavitation model is uncoupled from the CFD nanodispersion model because of significantly different time scales. The frequency used in the UST experiments is 18 kHz. However, modeling of ultrasonic cavitation takes place at a very small time scale (on the order of

$10^{-5}$  to  $10^{-7}$  s) and the fluid flow time scale is on the order of  $10^{-2}$  to  $10^{-3}$  s in this case. In order to account for the effects of ultrasonic stirring on the fluid flow-nanoparticle interaction, the ultrasonic probe surface is set as a velocity inlet sinusoidal profile with a frequency of 100 Hz (see Figure 4.2), and therefore the time step in the nanodispersion simulations can be much higher (*i.e.*, 0.001s), which makes it possible to model the fluid flow with nanoparticles for much longer times with a reasonable computational time. After the initial transient, which is about 1s after adding the nanoparticles, and for the velocity profile shown in Figure 4.2, the characteristics of the fluid flow and nanodispersion remain unchanged. A similar trend can be found at high frequencies [114, 115].

## CHAPTER 5 – SIMULATION RESULTS AND DISCUSSION

### 5.1 CFD Ultrasonic Cavitation Modeling Results

The predictions of the ultrasonic cavitation and velocity vectors are presented in Figure 5.1 for an A356 liquid alloy at time  $t = 2.0 \times 10^{-4}$  s, which is after the onset of cavitation. The simulations are obtained with the UST cavitation model summarized in Chapter 4 and presented in detail in [112, 113, 116]. The onset of cavitation for this alloy system is around  $8.8 \times 10^{-6}$  s [26]. The predicted ultrasonic cavitation region is presented in Figure 5.1 (a), where the cavitation phase is hydrogen. The cavitation region is relatively small at time  $t = 2 \times 10^{-4}$  s, the acoustic streaming is relatively strong, especially in the ultrasonic probe region and thus the newly created/survived bubbles/nuclei can be transported into the bulk liquid quickly. Note that the legend in Figure 5.1 (a) shows the volume cavitation region (volume fraction of cavities/bubbles/potential nuclei). Figure 5.1 (b) shows the profile for the velocity vectors and the velocity magnitude is significantly high beneath the ultrasonic probe.

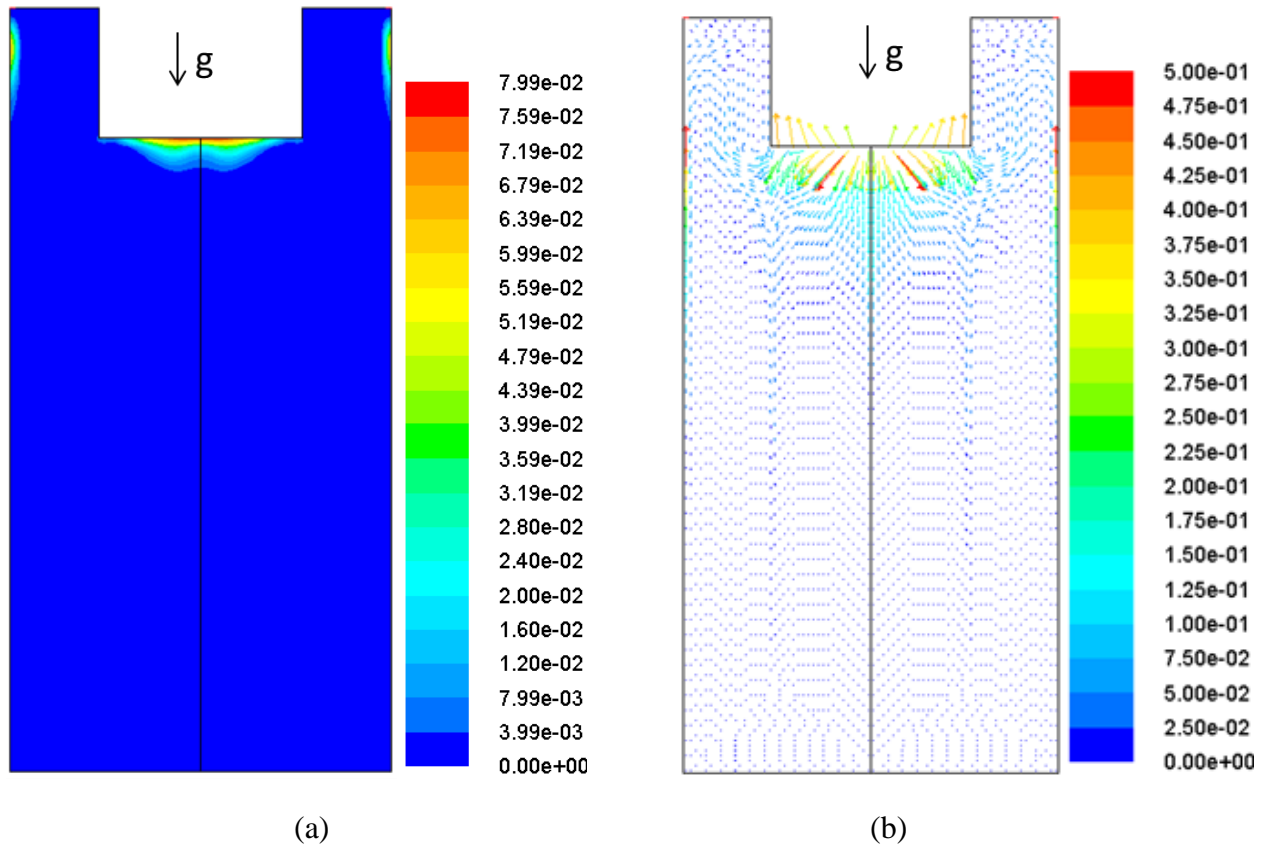


Figure 5.1 (a) Cavitation region and (b) velocity vectors (m/s) at  $t = 2e-04$  s [113]

Note that a detailed study was performed in [112] to determine the flow characteristics during ultrasonic processing of molten metallic alloys under two different gravity conditions: (i) gravitational acceleration oriented downward and (ii) gravitational acceleration oriented upward. It was found [112] that the latter case had significantly stronger bulk stirring and a larger cavitation zone that was more favorable for ultrasonic stirring and cavitation processing of alloys and metal-matrix-nanocomposites.

## 5.2 CFD Nanodispersion Modeling Results

Figure 5.2 shows the fluid flow profile (colored by velocity magnitude, similarly hereinafter) after 3.0 sec with the ultrasonic probe located at the top and the bottom of the furnace, respectively. The flow is simulated using the CFD nanodispersion model summarized in Chapter 4 and presented in more detail in [114, 115]. It can be seen that the flow is much

stronger at the center of the furnace for both cases. But the flow patterns are not exactly the same due to the change of the gravitational acceleration orientation.

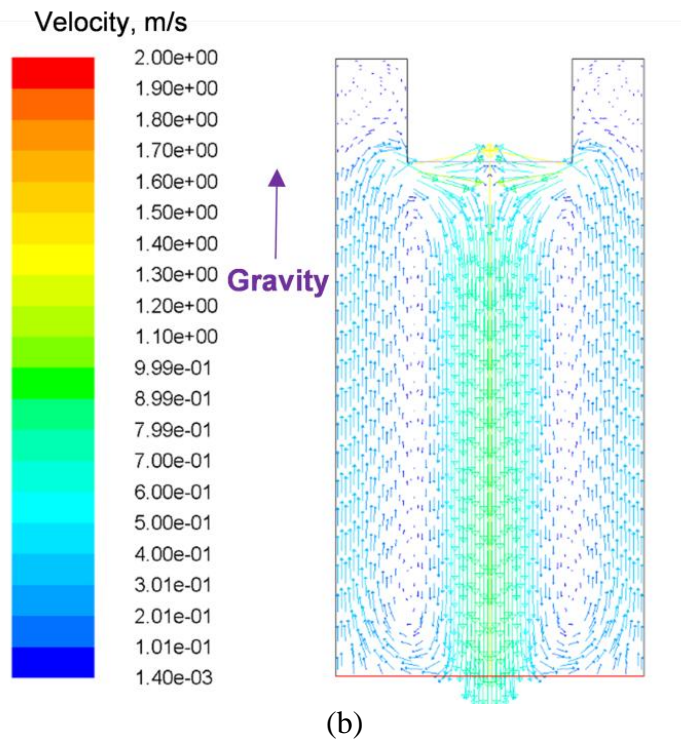
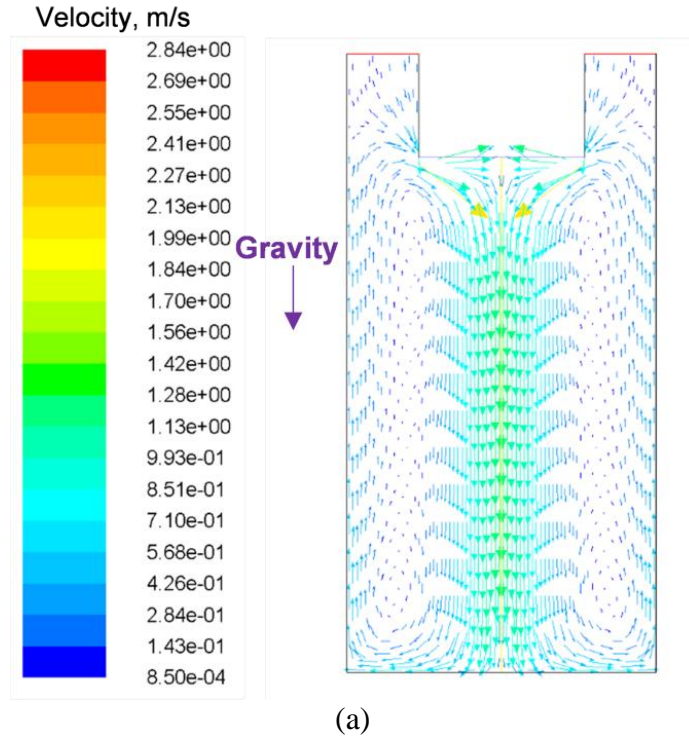
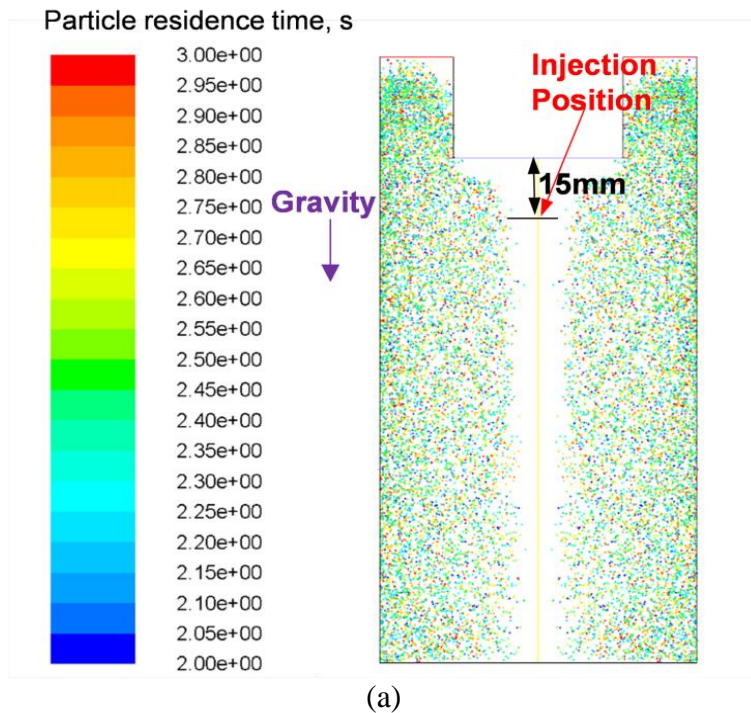
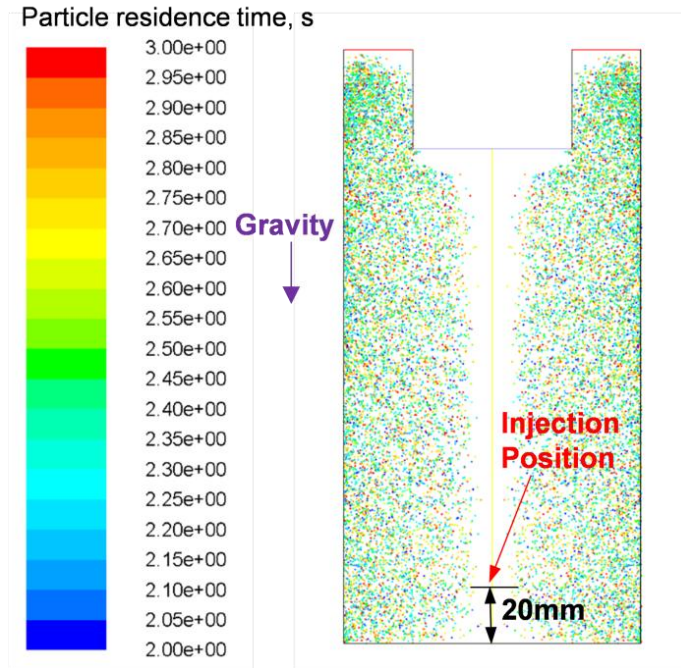


Figure 5.2 Fluid flow profile after 3 s using different ultrasonic probe locations: (a) ultrasonic probe located at the top and (b) ultrasonic probe located at the top [115]

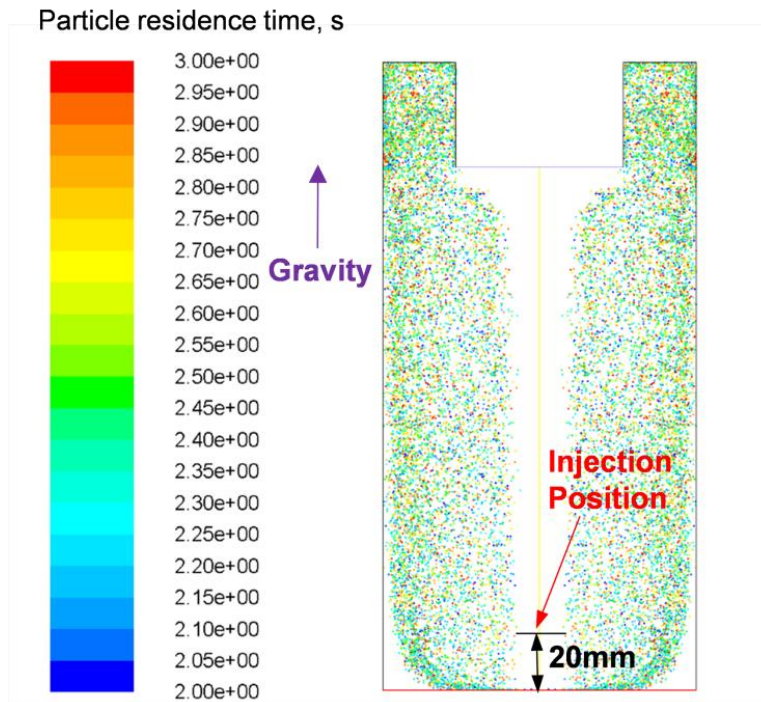
The particle distributions after 3.0 sec using different injection positions and ultrasonic probe locations: (a) particles added at the bottom (ultrasonic probe located at the top); (b) particles added at the top (ultrasonic probe located at the top); and (c) particles added at the bottom (ultrasonic probe located at the bottom) are shown in Figure 5.3. As we can see, after 3.0 sec, the nanoparticles are well dispersed in the fluid, and the distributions are almost the same even with different injection positions. It is demonstrated that the injection position will not affect the final distribution of the SiC nanoparticles as long as the fluid flow is strong enough to disperse the nanoparticles. However, compared with Figure 5.3 (a) and (b), Figure 5.3 (c) presents a different nanoparticle distribution because the fluid flow is changed due to the change of the gravitational acceleration orientation. But the general trend is basically the same, *i.e.*, where the flow is stronger, there are fewer particles, and vice versa.



(a)



(b)



(c)

Figure 5.3 Particles distributions after 3 s using different injection positions and ultrasonic probe locations: (a) particles injected at the bottom (ultrasonic probe located at the top); (b) particles injected at the top (ultrasonic probe located at the top); and (c) particles injected at the bottom (ultrasonic probe located at the bottom) [115]

The CFD model also demonstrates that the nanoparticles can be well dispersed into the molten alloy after about 3.0 sec. However, according to some classical pushing and engulfment of particles (PEP) models [118-122], smaller particles will be pushed by the solidification front during the solidification process leading to agglomeration or aggregation. Indeed, as shown in [123], these models cannot explain the evidence in MMNCs that nanoparticles can indeed be engulfed and distributed throughout the material and are not necessarily concentrated in grain boundary or interdendritic regions. For sufficiently small particles, “Brownian Motion” can partially or completely counteract forces such as viscous drag, gravity and thermal/concentration gradients, thus leading to engulfment rather than pushing. Therefore, based on the assumption that the nanoparticles will not be significantly agglomerated during the solidification process, it is assured that a finely dispersed nanoparticle composite would be obtained after the solidification, which is also proved by our experimental work. This is confirmed by the results shown in Figure 5.4. The particle distributions associated with the solidification after 2 min and 4 min are shown in Figure 5.4 [124]. As it can be seen, the particles will be engulfed and uniformly distributed in the metal matrix eventually.

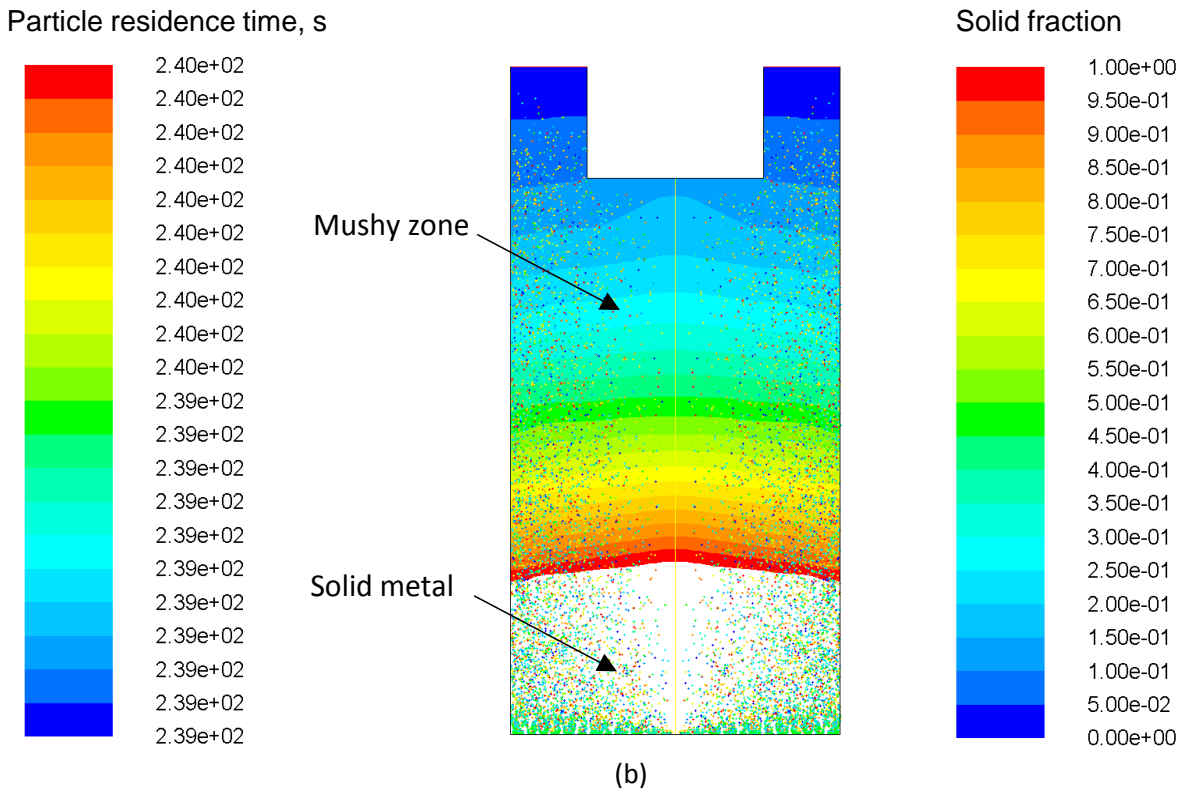
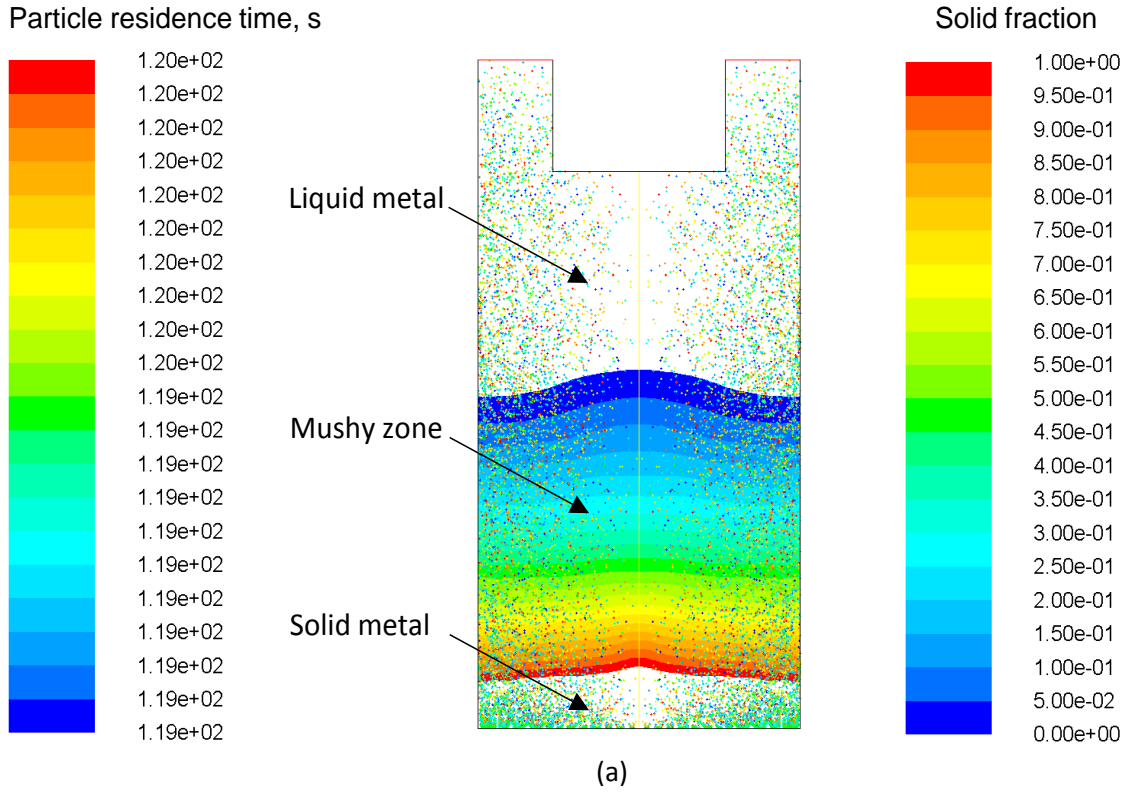


Figure 5.4 Distribution associated with the solidification after (a) 2 min and (b) 4 min [124]

## CHAPTER 6 – EXPERIMENTAL RESULTS AND DISCUSSION

When adding nanoparticles during the experiments, it is found that excess amount of nanoparticles, if more than 1 wt. %, would cause severe wetting and floating problems. To avoid those problems and to make sure the amount of nanoparticles is sufficient to fulfill the full potential, it is determined that the optimum amount of nanoparticles is 1 wt. %.

Several novel methods of adding nanoparticles into the molten alloys are investigated to better suit the requirements of the scale-up work of fabricating MMNC. These methods include using floating injector, making preformed master – alloy composites and wrapping nanoparticles with aluminum foil. The floating injector is expensive and could be easily stuck by the nanoparticles. The preformed master – alloy composites are made from 99.9% pure aluminum powder and nanoparticle powder. The master – alloy composites do not melt with molten metal. Possible reason could be the oxidation of pure aluminum powder. In present study, wrapping nanoparticles with aluminum foil is the most practical method to add nanoparticles into molten metal.

### 6.1 Microscopy Analysis of 6061 / 1.0 wt. % SiC Samples

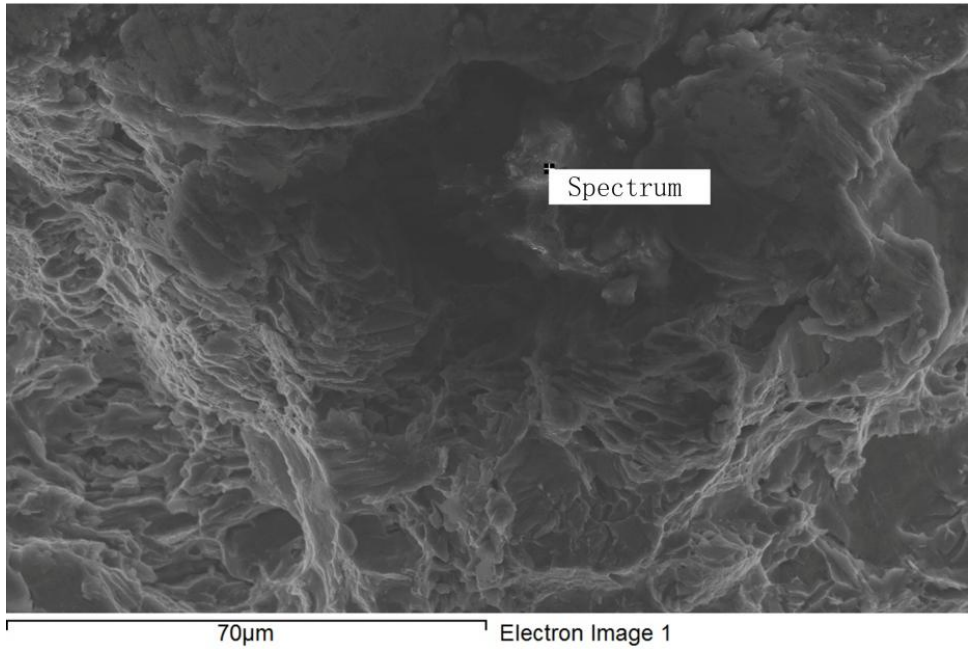
Figure 6.1 shows the distribution of SiC nanoparticles in the 6061/1 wt % SiC nanocomposite samples. EDS analysis is performed only for SiC reinforced 6061 nanocomposite, because  $\text{Al}_2\text{O}_3$  nanoparticles cannot be distinguished in  $\text{Al}_2\text{O}_3$  reinforced 6061 nanocomposite samples. It can be seen that the SiC nanoparticles are dispersed reasonably well into the 6061 matrix. It can also be seen from Figure 6.1 (d) that some insignificant agglomeration occurs during the MMNC processing. Figure 6.1 (b) and (c) show the EDS spectrum of elements in the

6061 nanocomposites, in which Si and C are both detected in the nanocomposite sample. The only possible source of the C showing in the EDS spectrum is from SiC nanoparticle addition.

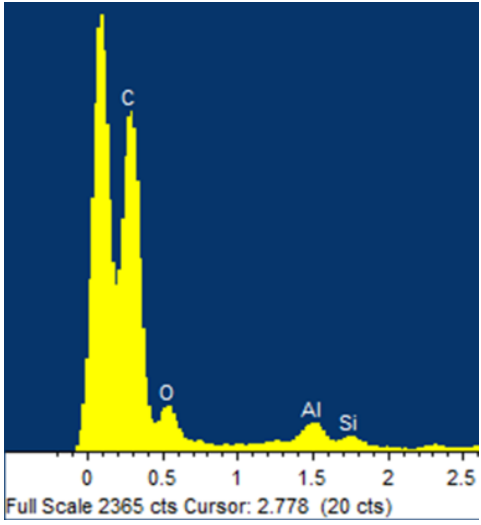
From Figure 6.2, we can see that the alloy samples fail in more of a brittle transgranular manner. Fracture path goes through the grains, and the brittle facets are caused by a fast propagation of the crack trans-granularly across the grains. Some ductile fracture (dimples) can also be observed.

Figure 6.3 shows the tensile fracture in an UST+1% SiC nanocomposite sample. From Figure 6.3, the dimpled surface of nanocomposite samples indicates that the fracture mechanism is dominated by micro-void coalescence. One of the main mechanisms of ductile fracture is known as micro-void coalescence. In this type of failure, microscopic second phase particles in the metal act as stress concentrators. When a triaxial stress state is concentrated at these points, the surrounding material pulls away from the contaminants forming voids in the metal. These voids grow until adjacent voids connect, coalescing into larger voids. Final failure of the material occurs when the voids grow larger and connect together. The occurrence of dimples suggests strong interfacial bonding between the matrix and reinforcement. The addition of these nanoparticles in 6061 alloy matrix definitely changes the fracture mechanism from brittle dominated to ductile dominated. Similar results are obtained for UST+1% Al<sub>2</sub>O<sub>3</sub> nanocomposite samples.

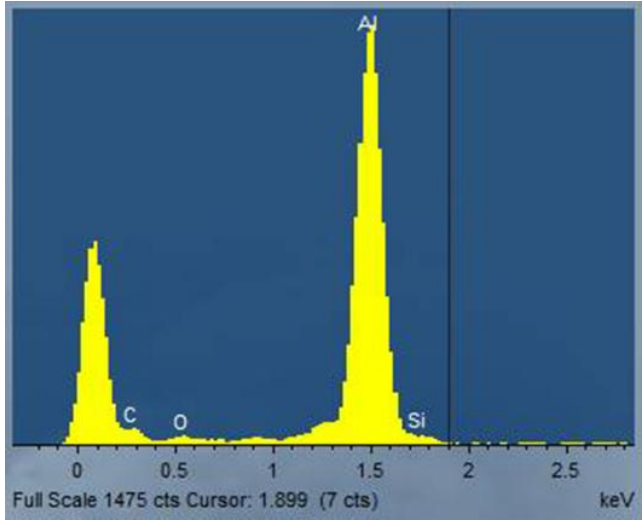
Based on Figure 6.4 and Figure 6.5, in some dimples, reinforcement nanoparticles are found, which confirms the micro-void coalescence mechanism. Not all dimples show trace of reinforcement nanoparticles due to debonding and embedding of nanoparticles.



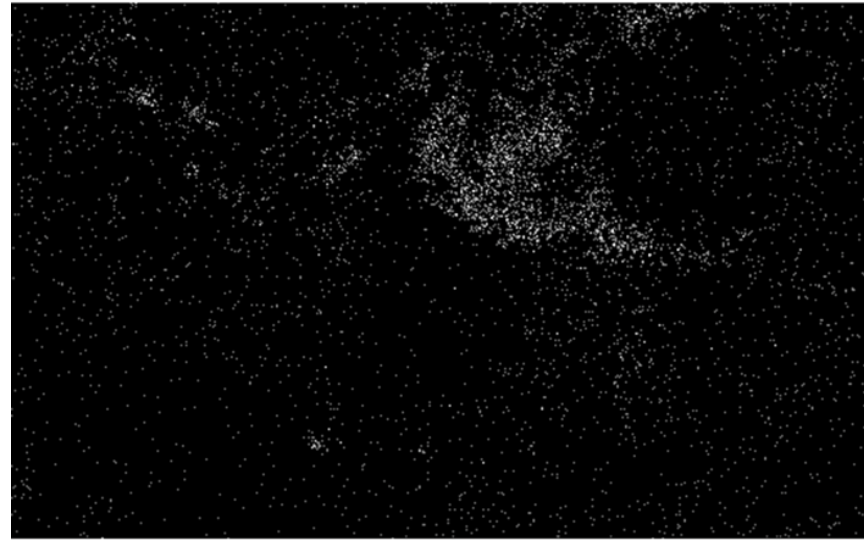
(a)



(b)



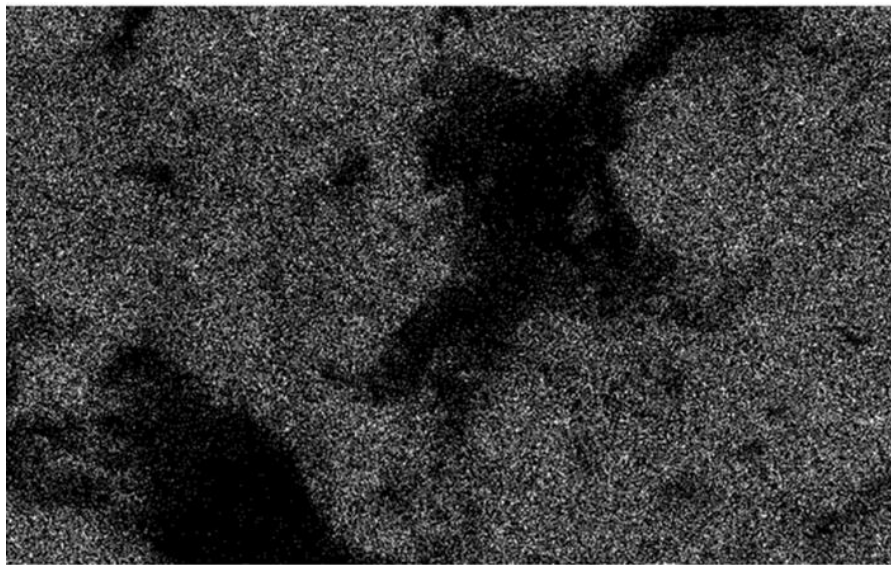
(c)



70 $\mu$ m

C Ka1\_2

(d)

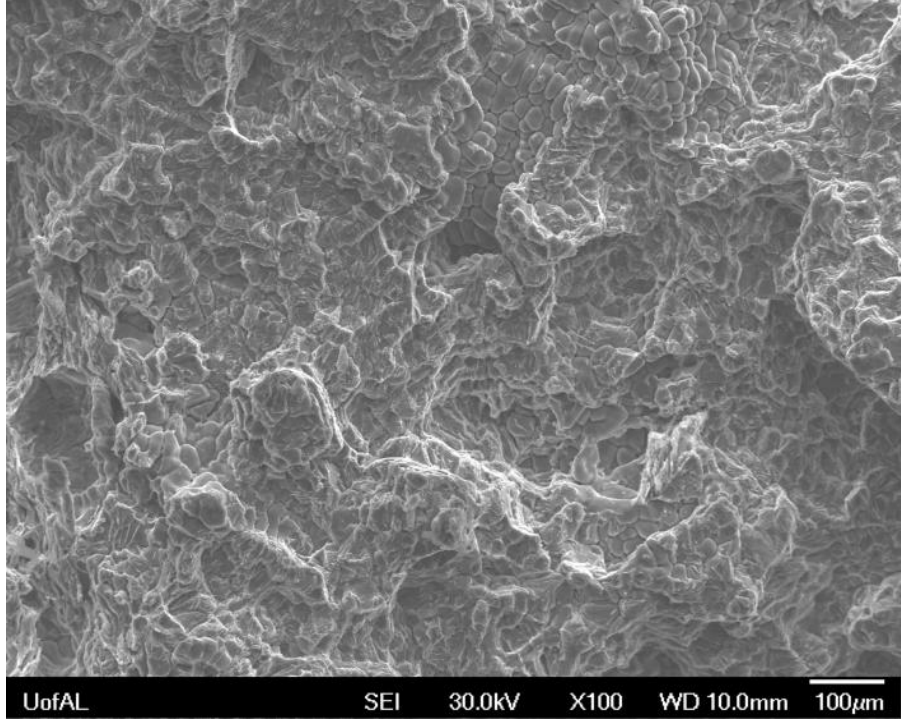


70 $\mu$ m

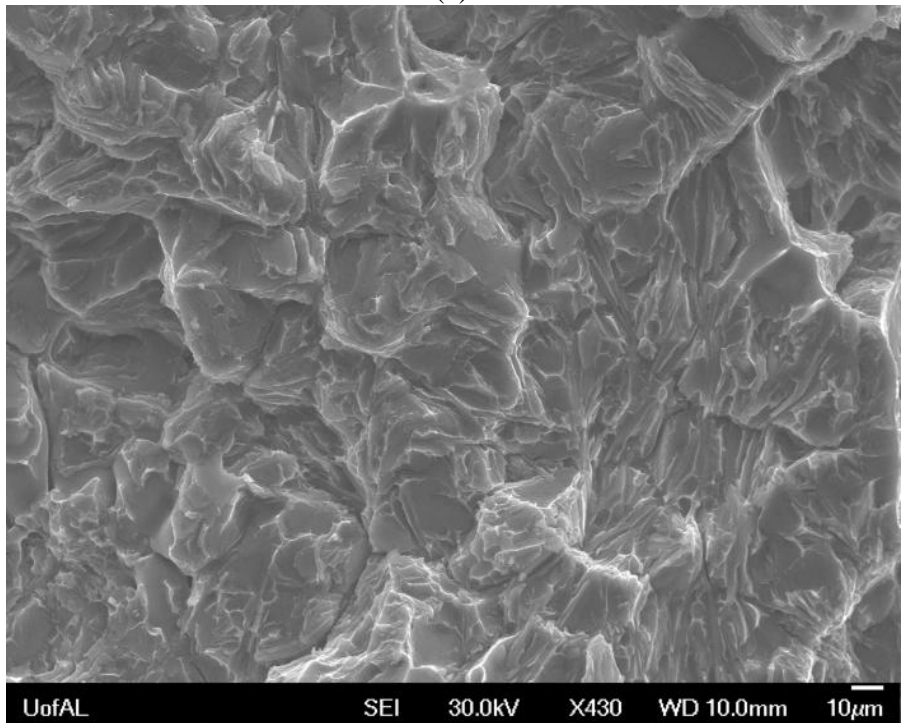
Al Ka1

(e)

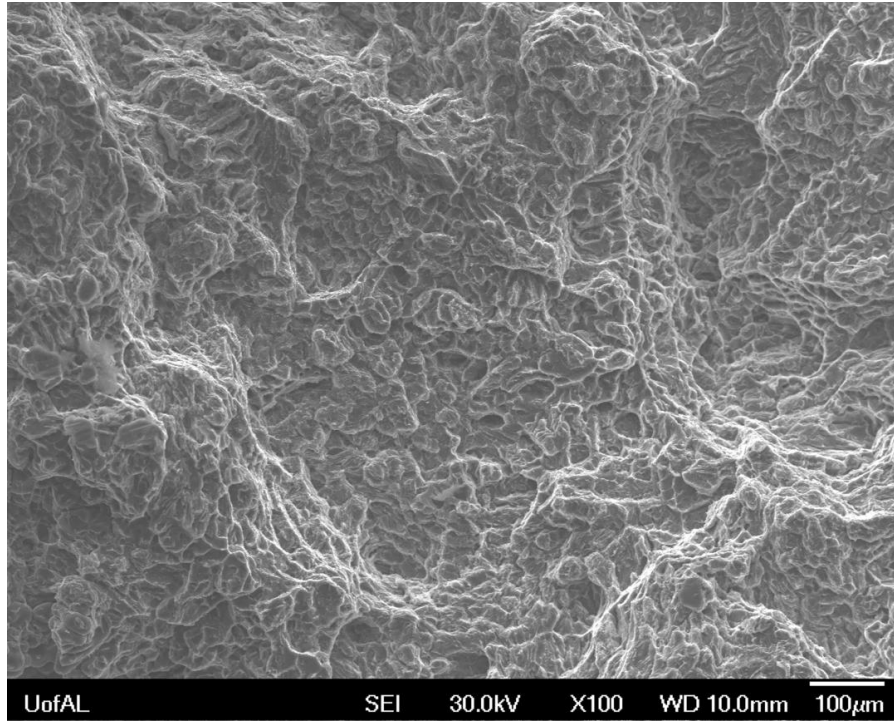
Figure 6.1 (a) SEM tensile fracture surface of the 6061/1% SiC nanocomposite (b) EDS (for the Spectrum position) on the tensile fracture surface of the 6061/1% SiC nanocomposite (c) EDS for the whole area on the tensile fracture surface of the 6061/1% SiC nanocomposite (d) EDS mapping result for Carbon (e) EDS mapping result for Aluminum



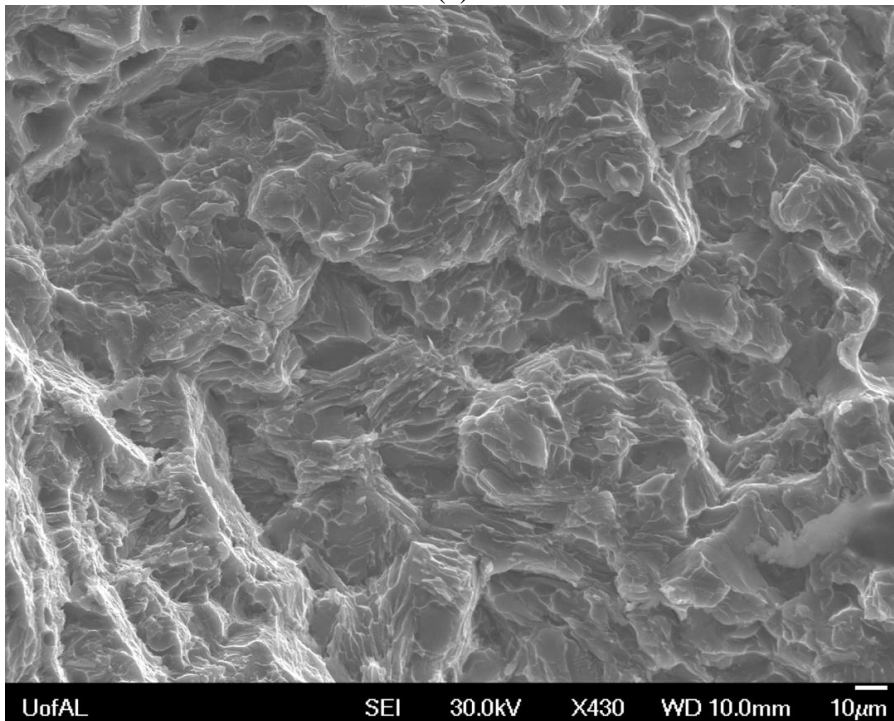
(a)



(b)

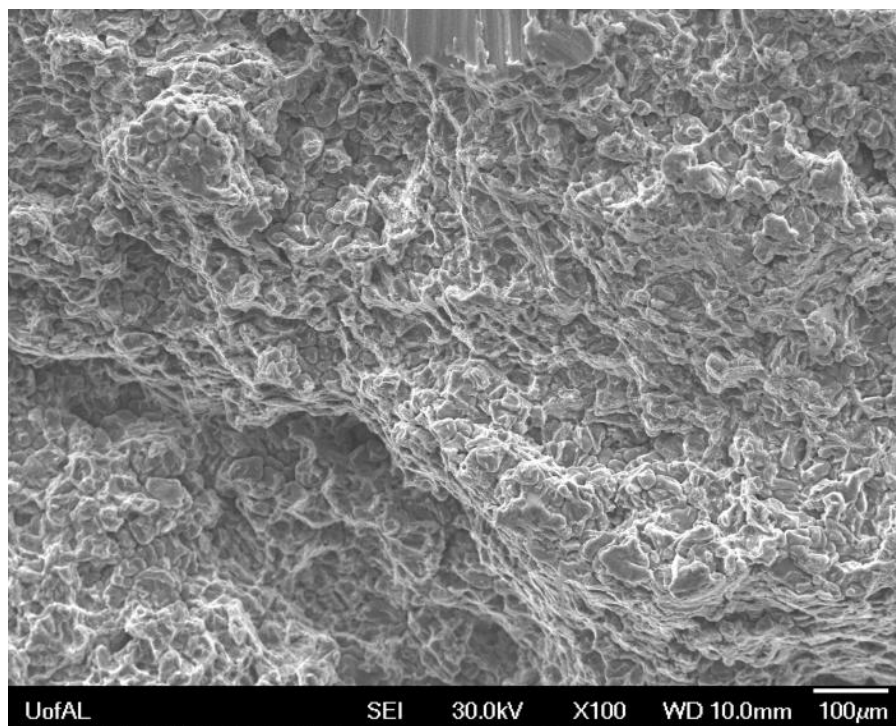


(c)

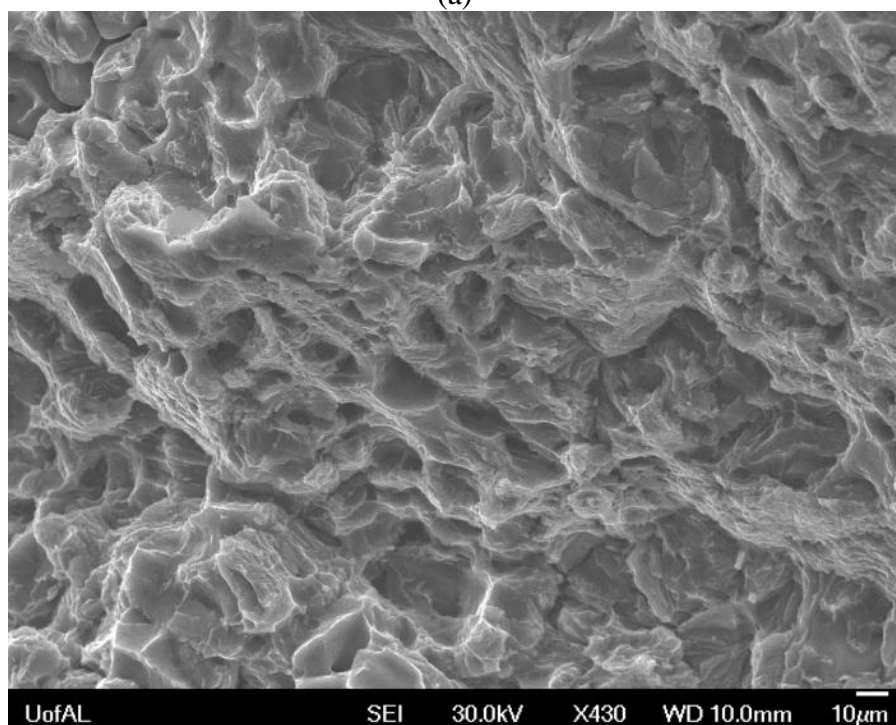


(d)

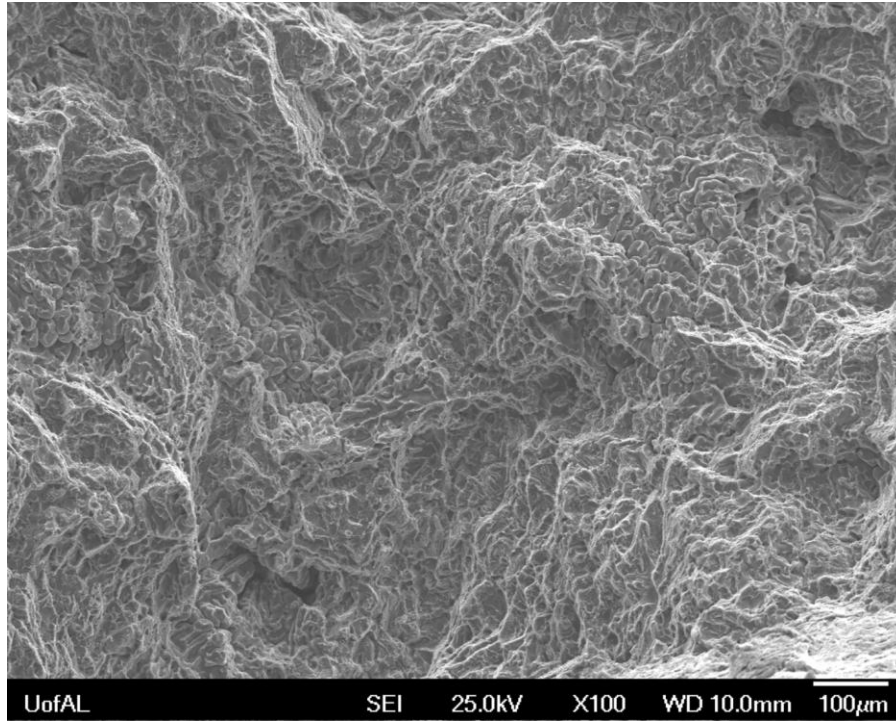
Figure 6.2 SEM pictures of tensile fracture surface for the two alloy samples processed under different conditions: (a) Ar degassed 6061 alloy casting at X100 and (b) Ar degassed 6061 alloy casting at X430 and (c) UST 6061 alloy casting at X100 (d) UST 6061 alloy casting at X430



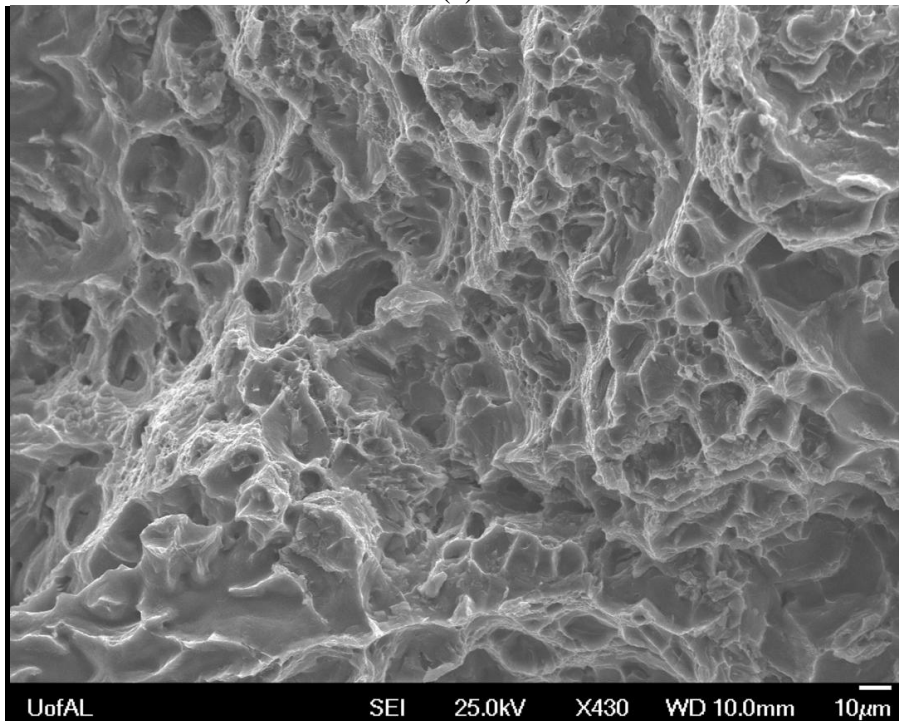
(a)



(b)

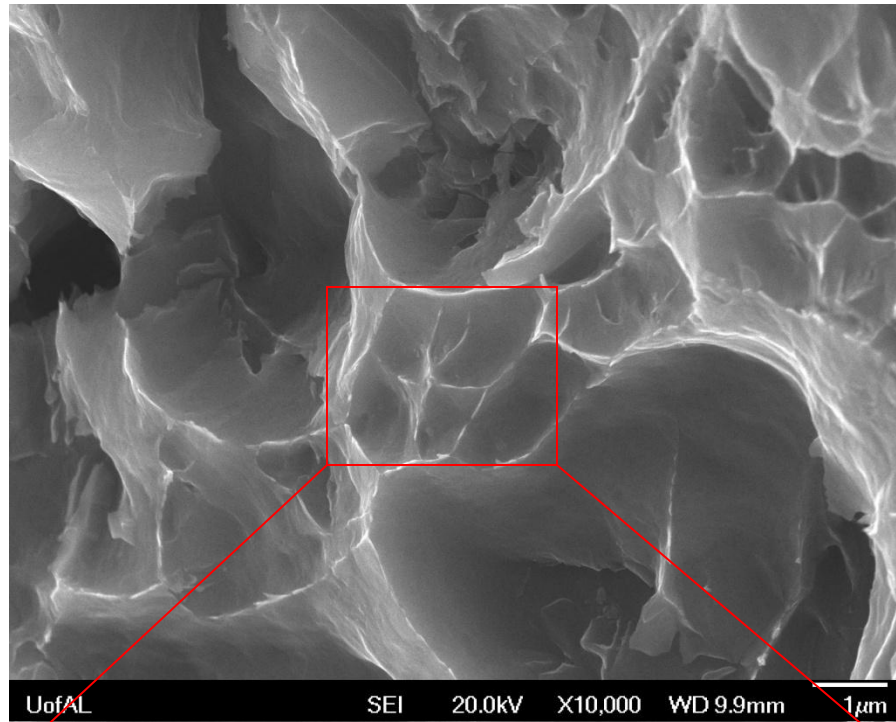


(c)

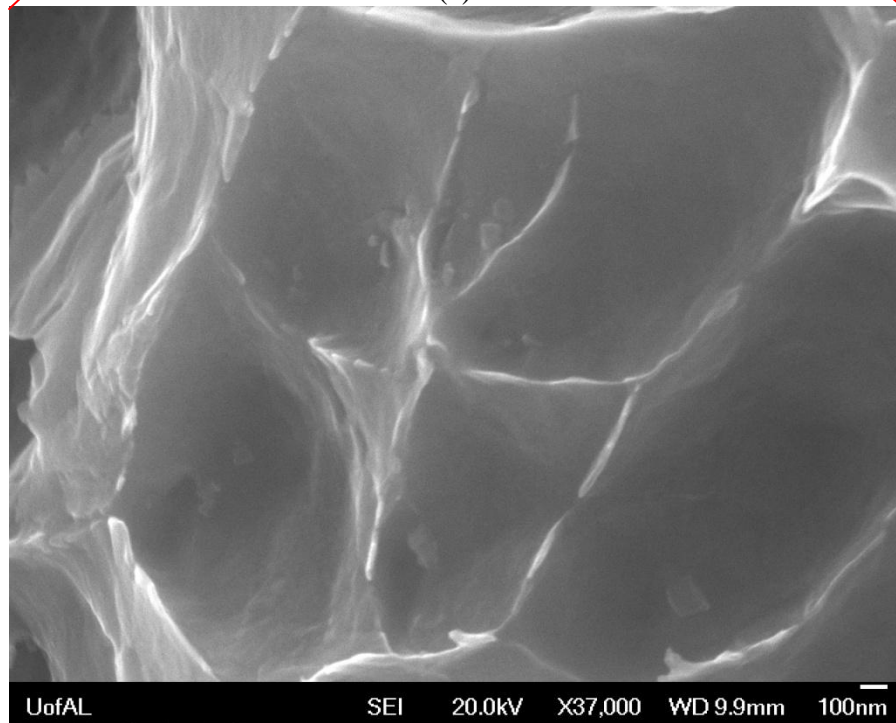


(d)

Figure 6.3 SEM pictures of tensile fracture surface for the 6061 based nanocomposite samples processed under different melting conditions: (a) UST+1% SiC nanocomposite casting at X100 (b) UST+1% SiC nanocomposite casting at X430 (c) UST+1%  $\text{Al}_2\text{O}_3$  nanocomposite casting at X100 (d) UST+1%  $\text{Al}_2\text{O}_3$  nanocomposite casting at X430

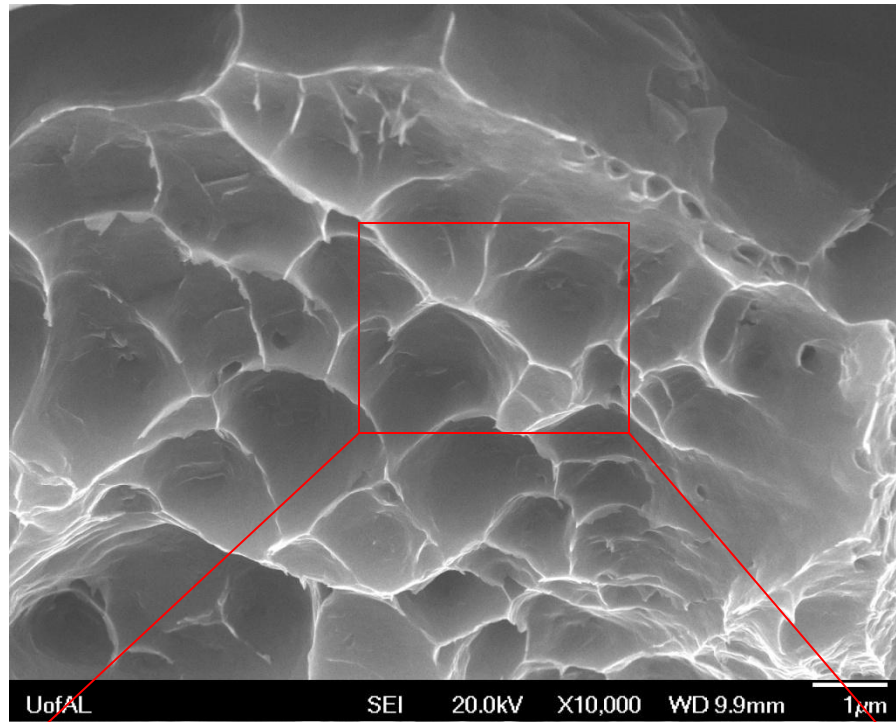


(a)

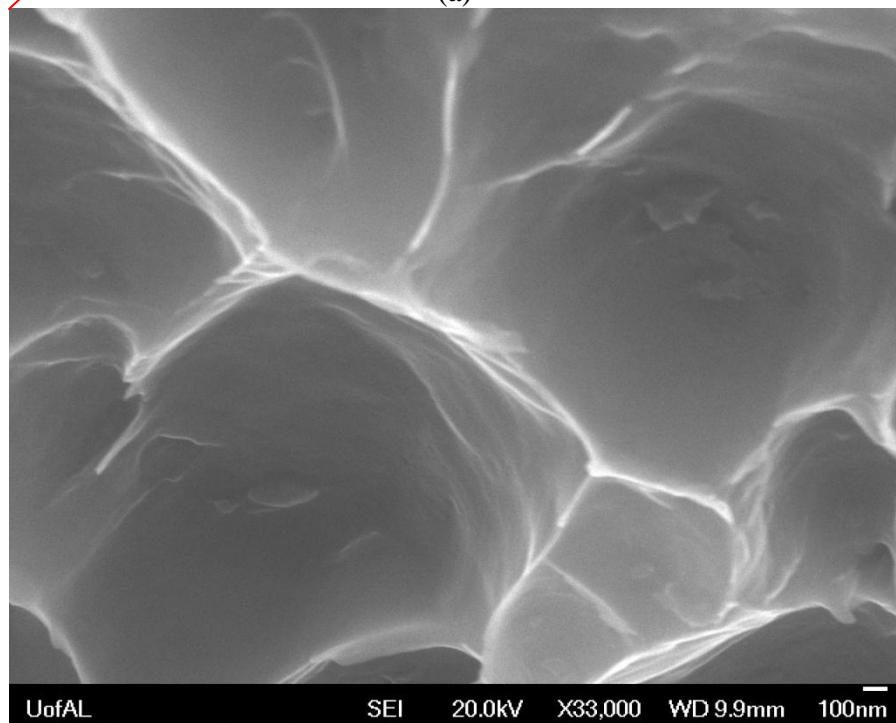


(b)

Figure 6.4 SEM pictures of tensile fracture surface for the 6061 based nanocomposite samples at higher magnification: (a) UST+1% SiC nanocomposite casting at X10000 (b) UST+1% SiC nanocomposite casting at X37000



(a)



(b)

Figure 6.5 SEM pictures of tensile fracture surface for the 6061 based nanocomposite samples at higher magnification: (a) UST+1%  $\text{Al}_2\text{O}_3$  nanocomposite casting at X10000 (b) UST+1%  $\text{Al}_2\text{O}_3$  nanocomposite casting at X33000

## 6.2 Analysis of Mechanical Properties of 6061 and A356 Nanocomposites

Table 6.1, Figure 6.6 and Figure 6.7 show the tensile test results for A356 alloy and SiC/Al<sub>2</sub>O<sub>3</sub> nanocomposites under different treatment conditions. By using the UST treatment and the addition of nanoparticles, the tensile strength increases after the UST treatment and addition of nanoparticles. For UST treated samples, the grain refinement could be the major mechanism for increasing strength and elongation. For the nanocomposite samples, the thermal mismatch between the reinforcements and matrix, Orowan looping between nanoparticles and some other mechanisms result in the increase of tensile strength. The agglomeration of nanoparticles and microporosity brought in by nanoparticles can decrease the elongation of nanocomposite samples. The mechanical properties after T6 heat treatment do not show significant difference. From Figure 6.8, after the T6 heat treatment, the degassed 6061 sample reveals some round remelted eutectic phases, which means that the solution temperature was too high and it needs to be optimized. More work has to be done to optimize the T6 heat treatment for the A356 alloy.

Table 6.1 Tensile testing results for A356 samples

A356 Samples	Tensile strength MPa	Elongation %
Ar Degassed	157.5 ± 6.2	3.8 ± 0.2
UST	172.6 ± 7.9	6.8 ± 0.6
UST+1% SiC	172.0 ± 5.9	4.3 ± 0.5
UST+1% Al <sub>2</sub> O <sub>3</sub>	177.6 ± 8.2	4.2 ± 0.4
Ar Degassed and T6	123.9 ± 1.5	4.2 ± 0.3
UST and T6	136.6 ± 1.2	4.3 ± 0.5
UST+1% SiC and T6	135.6 ± 3.6	8.3 ± 1.2
UST+1% Al <sub>2</sub> O <sub>3</sub> and T6	137.6 ± 0.8	4.7 ± 0.7

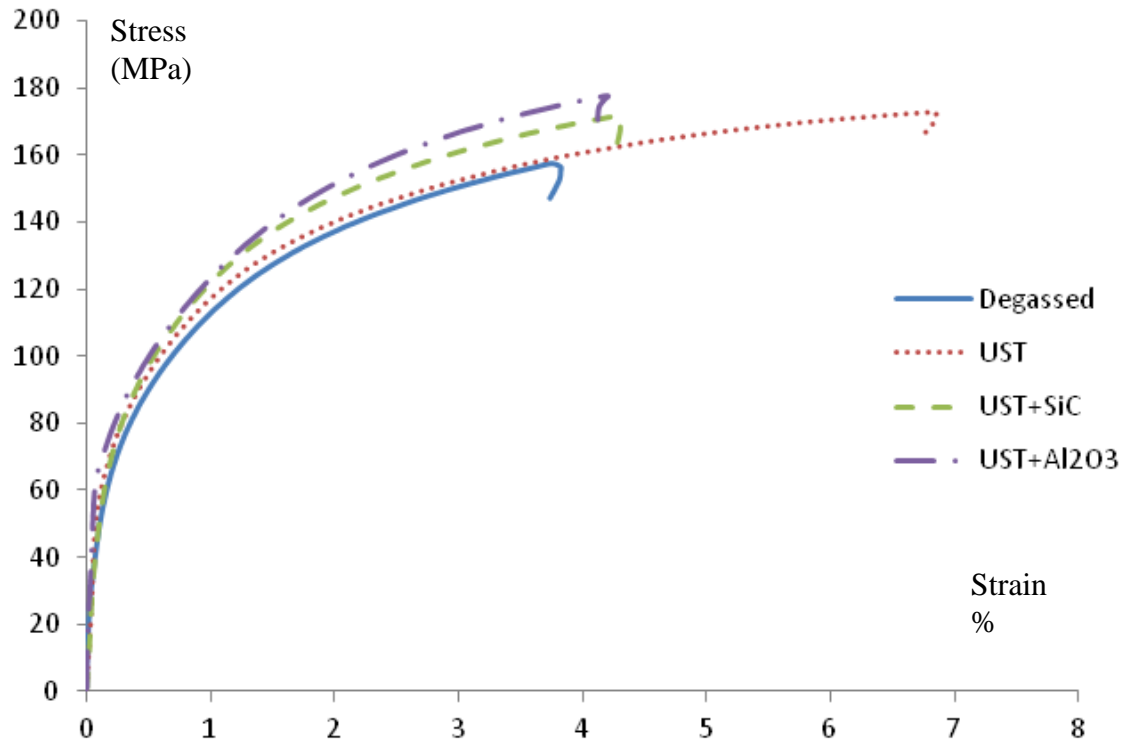


Figure 6.6 Tensile testing results for as-cast A356 samples

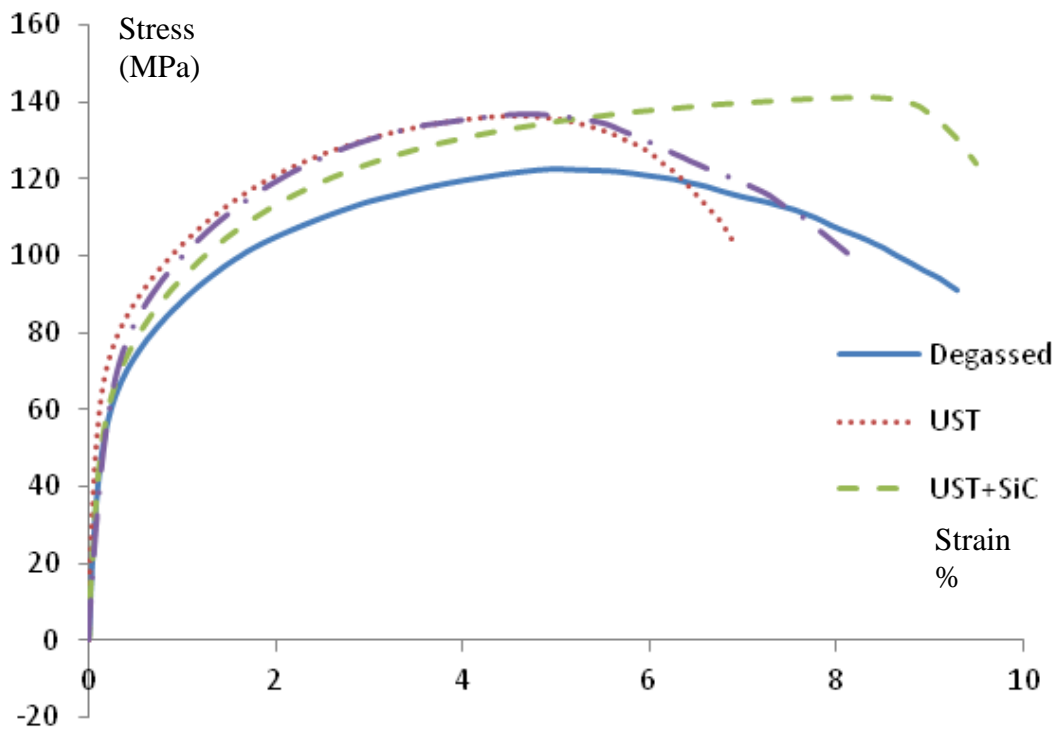
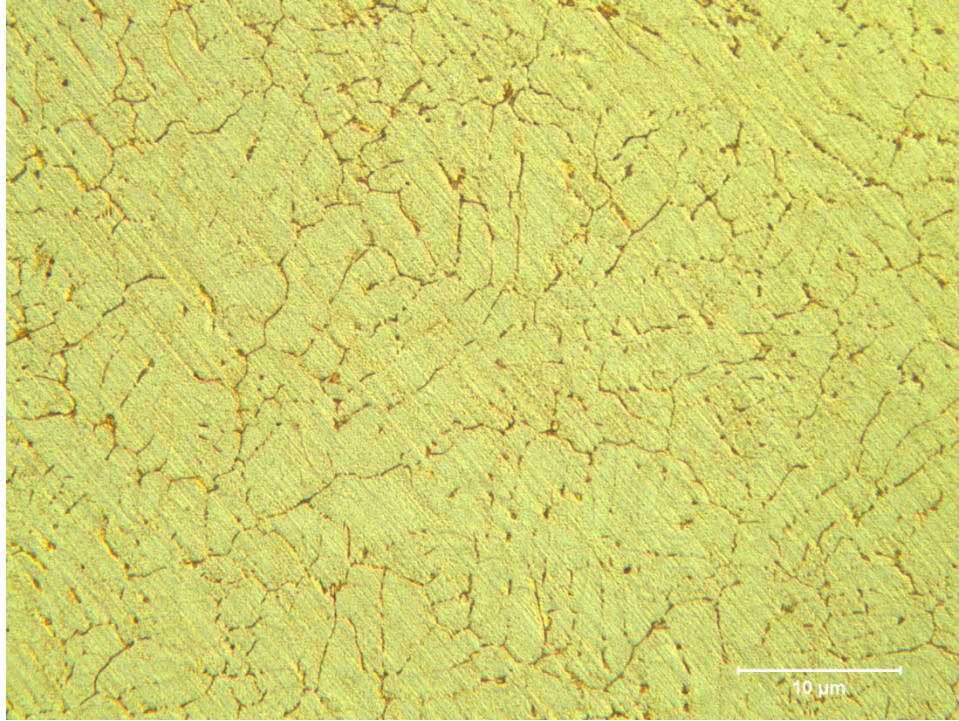
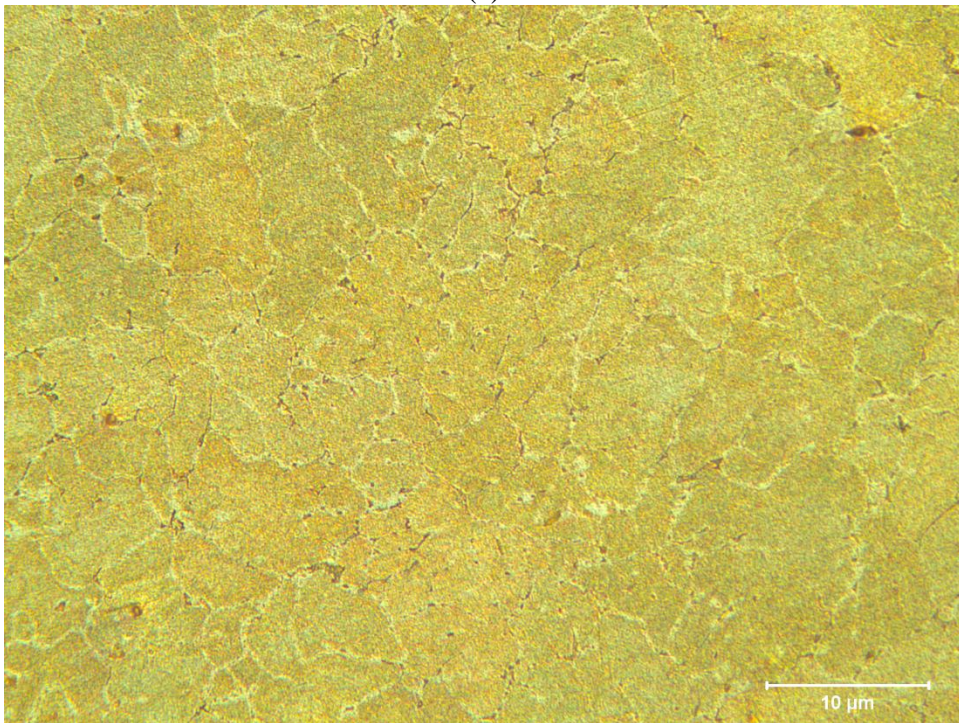


Figure 6.7 Tensile testing results for T6 heat treated A356 samples



(a)



(b)

Figure 6.8 Comparison of (a) as-cast degassed 6061 sample and (b) T6 heat treated sample

Table 6.2 shows the tensile test results for some other A356 alloy based nanocomposites with various reinforcement materials. During the experiments that involve the addition of TiB<sub>2</sub>, ZrC, or CNT, some flames and odor are observed indicating some reactions between the matrix and nanoparticles could have been occurred during the process.

Table 6.2 Tensile testing results for some other A356 alloy based nanocomposites samples

A356 Samples	Tensile strength MPa	Elongation %
UST+1% TiB <sub>2</sub>	150.55 ± 7.6	3.38 ± 0.2
UST+1% ZrC	153.88 ± 5.4	3.38 ± 0.6
UST+1% TiN	153.72 ± 6.2	3.43 ± 0.5
UST+1% CNT	142.71 ± 6.5	2.64 ± 0.7

The tensile results of the samples reinforced with TiB<sub>2</sub>, ZrC, or TiN are close to the Ar degassed as-cast samples shown in Table 6.1.

Table 6.3, Figure 6.9 and Figure 6.10 show the tensile test results for 6061 alloy and nanocomposites under different melt treatment conditions. By using the UST treatment and the addition of nanoparticles, the tensile strength almost remains the same. On the other hand, the elongation increases by 45% after the UST treatment and by 180% after the UST treatment and the addition of nanoparticles. T6 heat treatment is performed. The mechanical property after T6 heat treatment does not show significant difference. From Figure 6.11, after the T6 heat treatment, the degassed A356 sample reveals the distributed eutectic Si phases. Some of the Si phases are strip shape and some of the Si phases agglomerate, which are unfavorable to the mechanical properties. More work has to be done to optimize the T6 heat treatment for the 6061 alloy.

Table 6.3 Tensile testing results for 6061 samples

6061 Samples	Tensile strength MPa	Elongation %
Ar Degassed	$163.3 \pm 9.2$	$4.5 \pm 0.9$
UST	$154.6 \pm 11.3$	$5.8 \pm 1.3$
UST+1% SiC	$158.6 \pm 10.6$	$12.0 \pm 2.4$
UST+1% Al <sub>2</sub> O <sub>3</sub>	$163.5 \pm 12.9$	$12.2 \pm 1.9$
Ar Degassed and T6	$159.2 \pm 4.9$	$11.2 \pm 1.0$
UST and T6	$168.6 \pm 6.3$	$11.1 \pm 0.8$
UST+1% SiC and T6	$173.4 \pm 2.4$	$6.1 \pm 0.2$
UST+1% Al <sub>2</sub> O <sub>3</sub> and T6	$176.8 \pm 8.7$	$8.5 \pm 1.1$

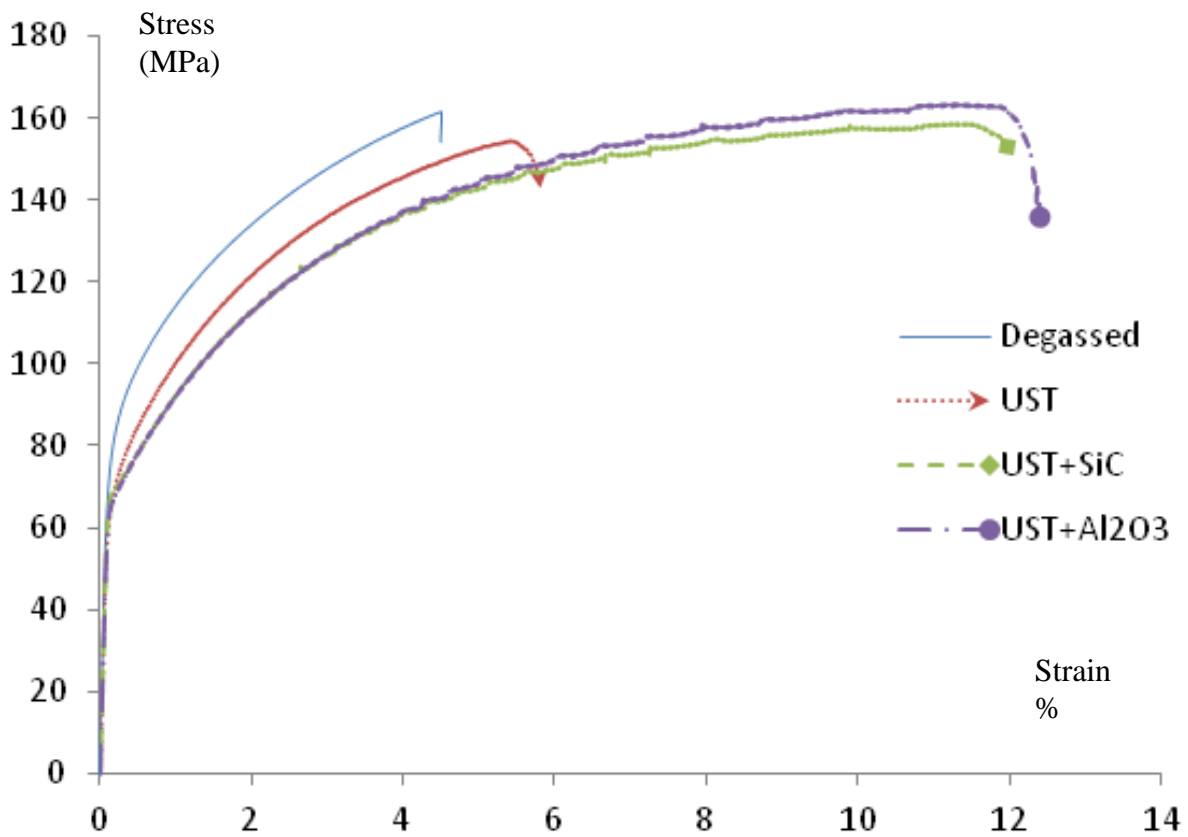


Figure 6.9 Tensile testing results for the as-cast 6061 samples

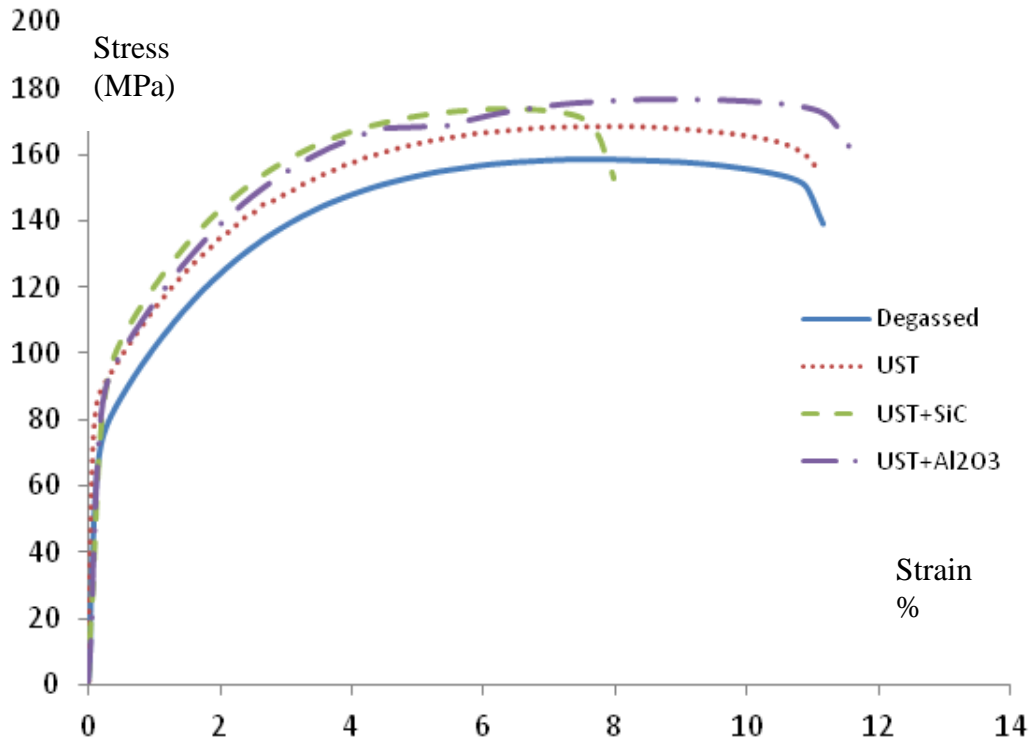


Figure 6.10 Tensile testing results for the T6 heat treated 6061 samples

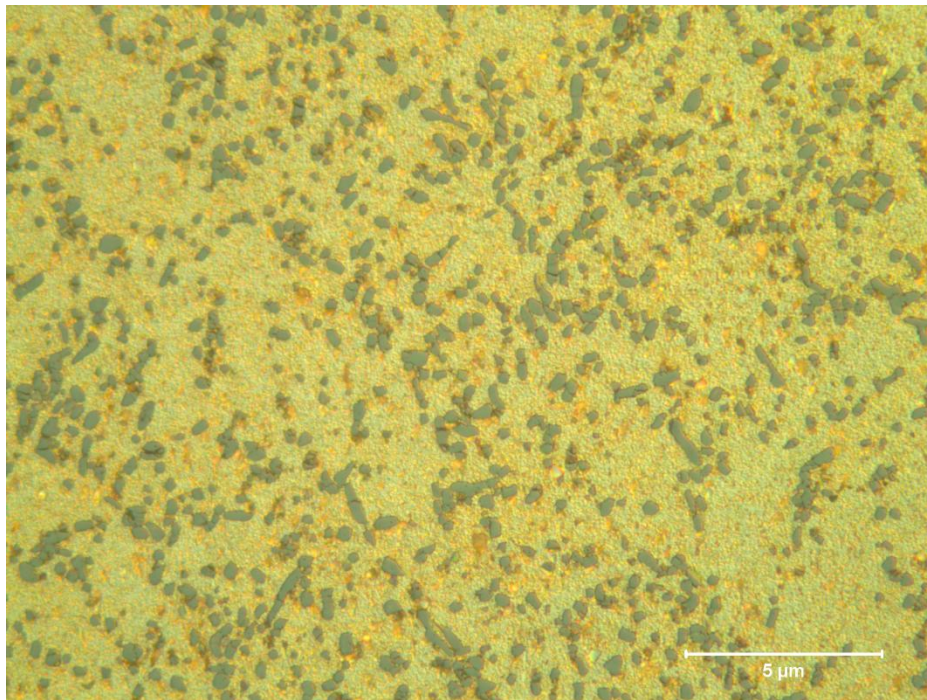


Figure 6.11 T6 heat treated A356 degassed sample

As discussed in other studies [125, 126], the thermal mismatch between the reinforcements and matrix, Orowan looping between nanoparticles and some other mechanism result in the increases of tensile strength. But the agglomeration of nanoparticles and microporosity brought in by nanoparticles can decrease the tensile strength of nanocomposite samples. The combination of these mechanisms may be the reason that the tensile strength almost remains the same for 6061 samples.

The increase in elongation for 6061 samples may be attributed to slip mode transition produced by the presence of nanoparticles which depends on the matrix/nanoparticles interaction. It has been previously shown that the presence of reinforcements can produce a slip mode transition depending on the reinforcement/matrix interaction [106]. As shown in other studies with CNTs [45], elongation also increases with the presence of reasonably amount of nanoparticles, but when the amount of nanoparticles is too big, the tensile strength and elongation both decrease due to greater agglomeration of nanoparticles and higher degree of microporosity present in the nanocomposites. The activation of cross slip in non-basal slip planes by the presence of nanoparticles may be responsible for the increased ductility observed in the present study.

Such different effects of UST and nanoparticles on A356 and 6061 samples may be explained by Si content difference in the two types of alloys. A356 alloy consists about 7% of Si element while 6061 alloy consists only about 0.4 - 0.8% Si element.

Since reinforcement-matrix interfaces play an important role in determining mechanical properties of particulate reinforced composites, previous study [127] paid attention to the interfaces between the SiC particles and alloy. SEM observation of polished and etched A356 - 10% SiC samples revealed that SiC particles appeared to act as substrates for nucleation of Si

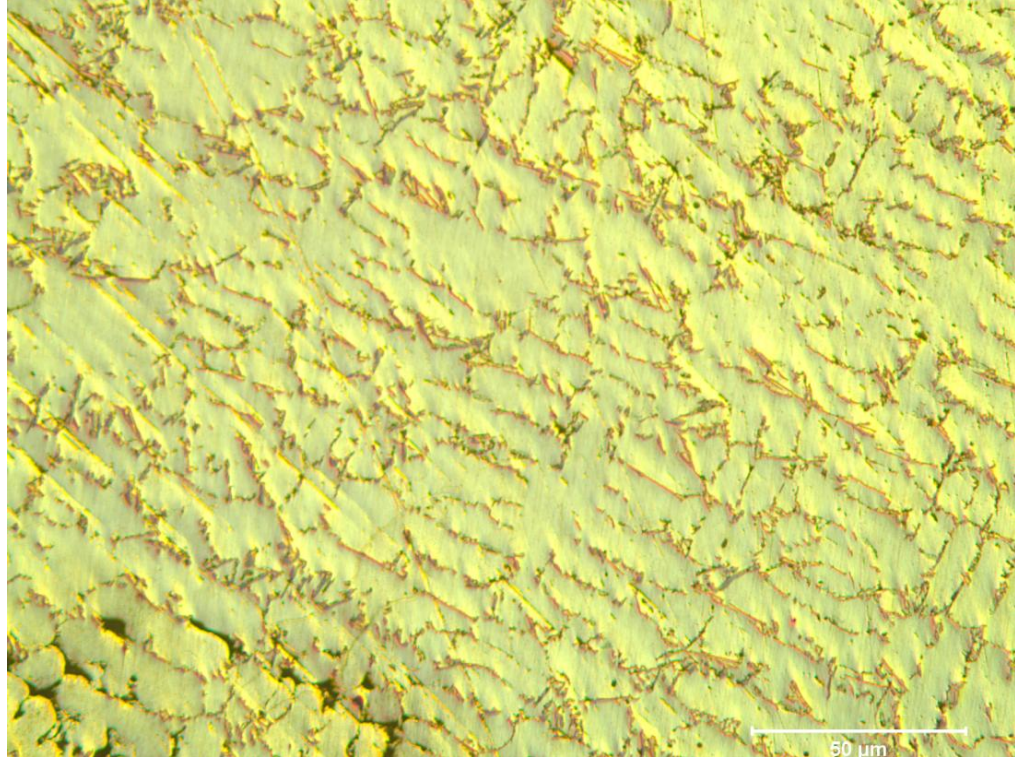
phase. Many Si crystals were observed to be attached to the surface of SiC particles, further supporting the observation that Si phase nucleated heterogeneously from the SiC particles.

In the present study, SiC and Al<sub>2</sub>O<sub>3</sub> nanoparticles may both act as substrates for nucleation of the Si phases in the A356 samples. The interfacial bonding between the nanoparticles and the Si phase may decrease the elongation of the A356 nanocomposite samples.

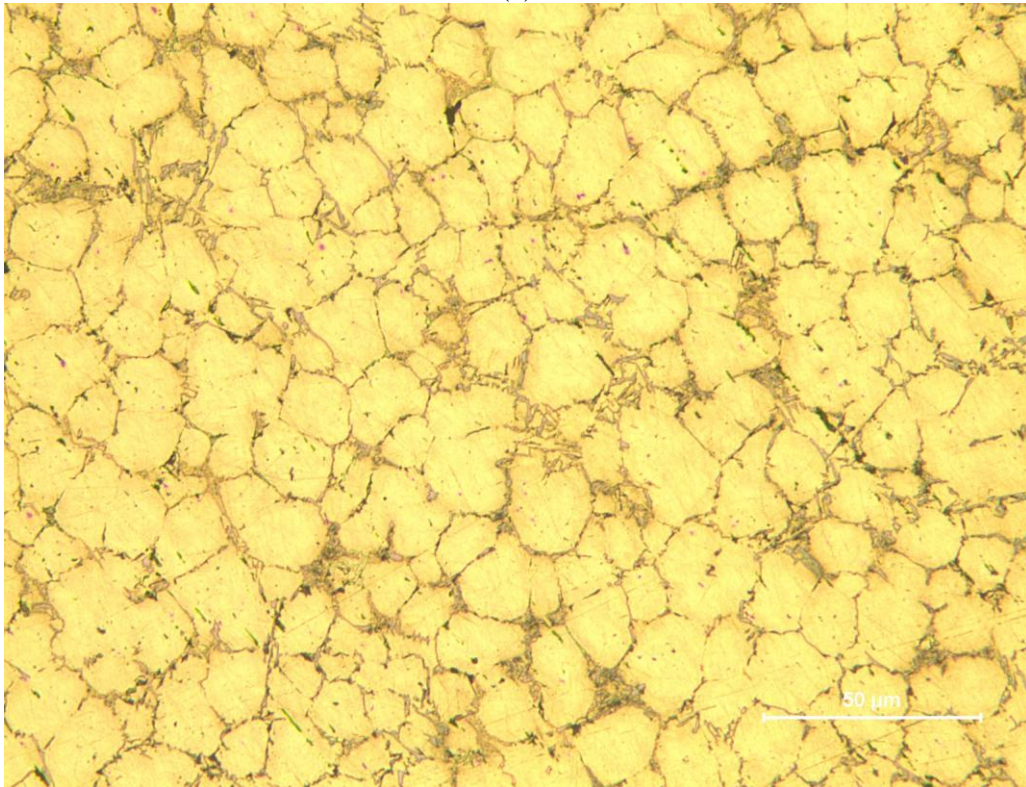
### 6.3 Microscopy Analysis of A356 Based Samples Treated during Solidification

Figure 6.12 shows a comparison of non-UST and UST treated A356 samples. As it can be seen from Figure 6.12, the samples without UST treatment have coarser microstructures than the ones with UST. It can also be seen that the dendritic structure (initial size of the order of hundreds of microns) is broken up because of the UST treatment. Basically, fine globular grain structures (of about 10 - 20 microns) can be observed in the samples obtained via UST during solidification. Also, it can be seen that the Si eutectic structure (black area) is more modified in the UST treated samples.

Figure 6.13 shows the optical microscope pictures at X50 magnification for A356 samples reinforced with SiC and Al<sub>2</sub>O<sub>3</sub>. Similar fine globular structures can be seen in Figure 6.12 (b), Figure 6.13 (a) and (b), which means that the UST is the main approach that promoted the refinement of the primary phase. The eutectic phase appears to have similar morphologies in the samples treated with the UST and with the UST and the addition of nanoparticles.

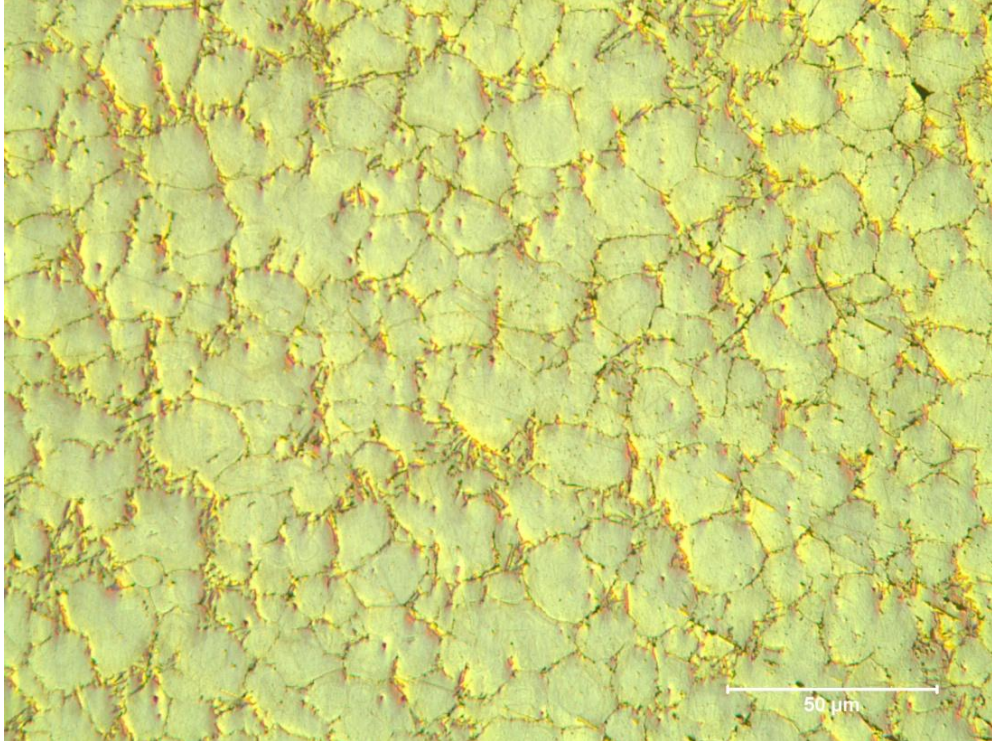


(a)

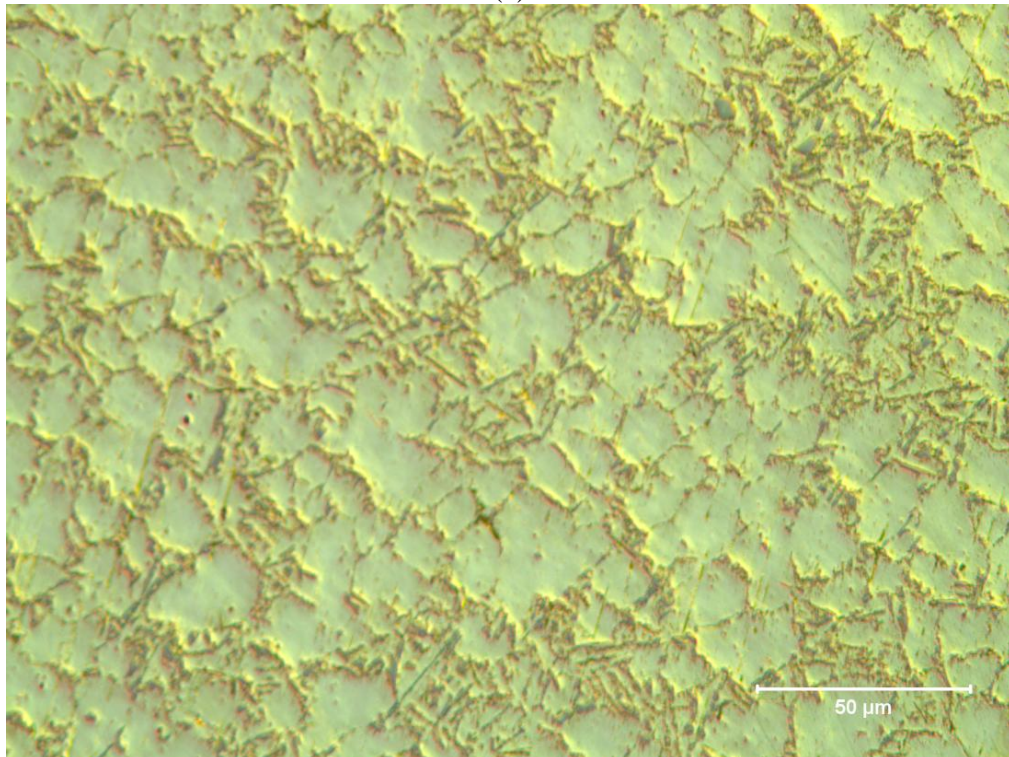


(b)

Figure 6.12 Optical microscope pictures at X50 for A356 samples (a) without UST treatment and (b) with UST treatment during solidification



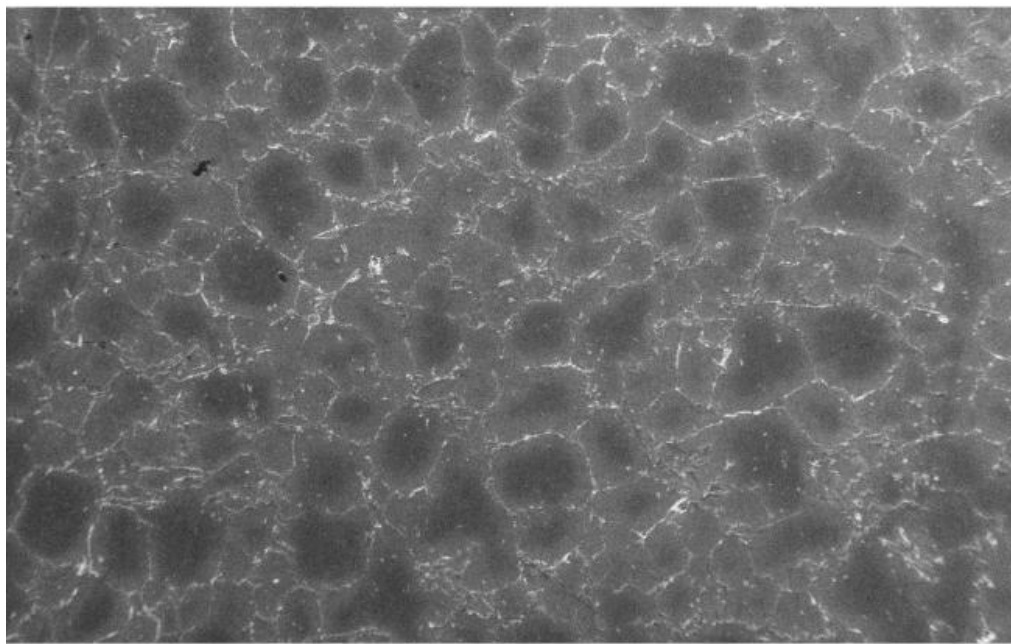
(a)



(b)

Figure 6.13 Optical microscope pictures at X50 for A356 samples reinforced with (a) UST + 1% SiC and (b) UST + 1% Al<sub>2</sub>O<sub>3</sub>

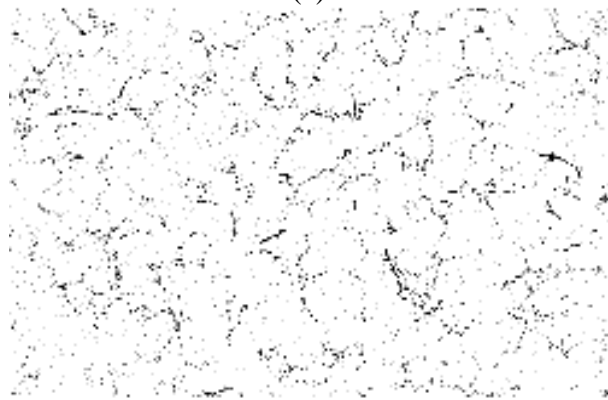
Figure 6.14 shows the distribution of SiC nanoparticles in A356 samples reinforced with UST + 1% SiC during solidification. EDS analysis has been performed only for SiC reinforced A356 nanocomposite, because Al<sub>2</sub>O<sub>3</sub> nanoparticles cannot be distinguished in Al<sub>2</sub>O<sub>3</sub> reinforced A356 nanocomposite samples. It can be seen that the SiC nanoparticles are dispersed reasonably well into the A356 matrix. It also confirms the optical microscope results from Figure 6.13 that grain structure is refined to achieve globular morphology.



1mm

Electron Image 1

(a)



1mm

Al Ka1

(b)

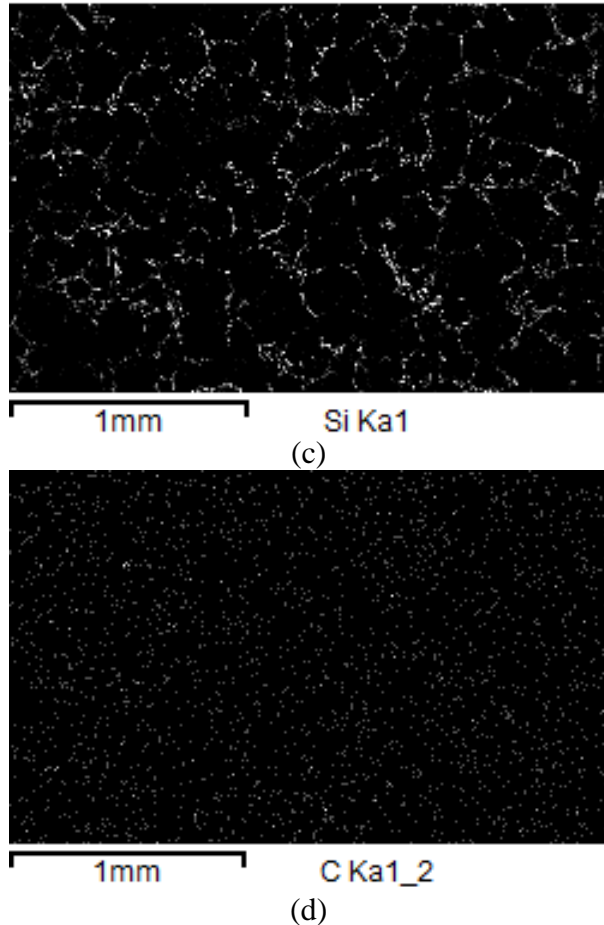
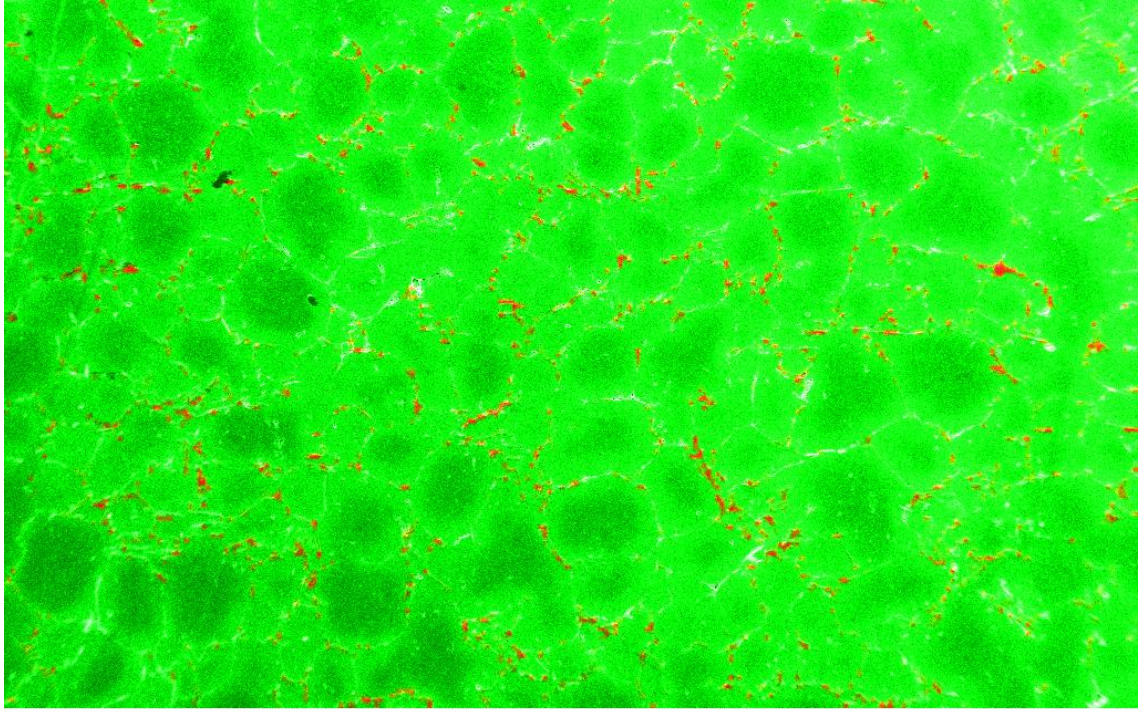


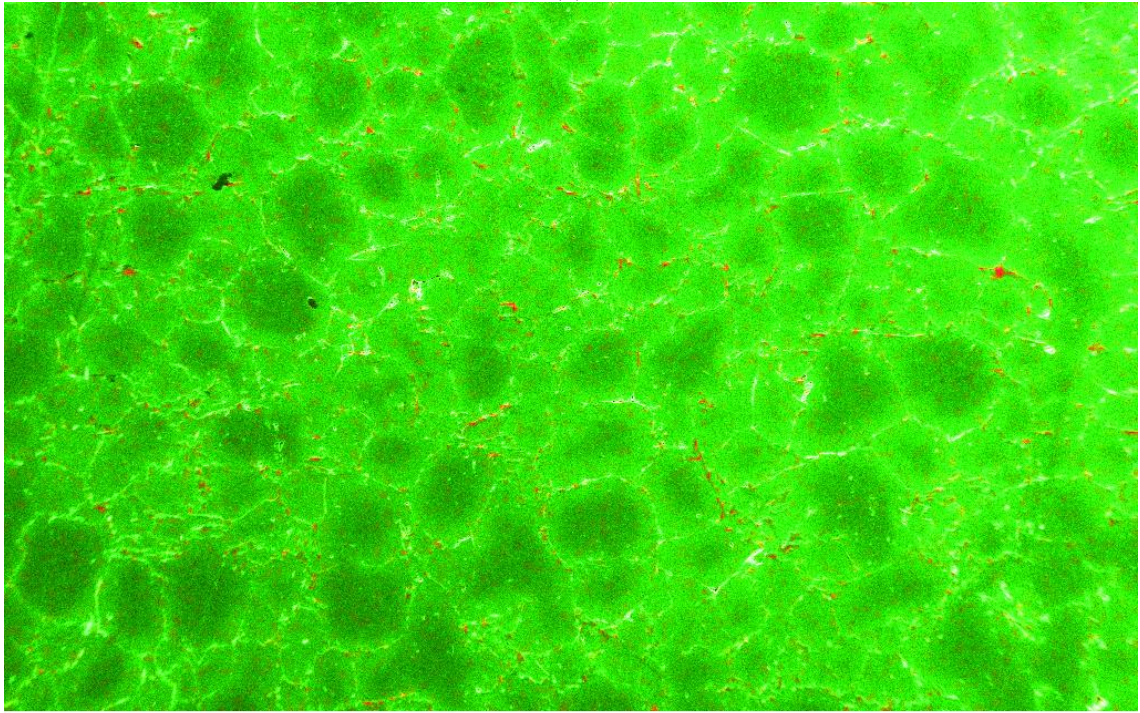
Figure 6.14 SEM results at X50 magnification for A356 samples reinforced with UST + 1% SiC during solidification: (a) SEM pictures (b) EDS mapping result for Al element (c) EDS mapping result for Si element (d) EDS mapping result for C element

Figure 6.15 shows the combined EDS mapping results of different elements. This makes it easier to track the locations of the primary phase, of the eutectic phase and of the SiC reinforcement phase. Figure 6.15 (b) shows that the distribution of C element is generally uniform. Some of the C element is embedded inside grain while most of C element tends to stay in the grain boundary area. Figure 6.15 (c) confirms that C element tends to gather around the grain boundary area where the Si eutectic phase is located.



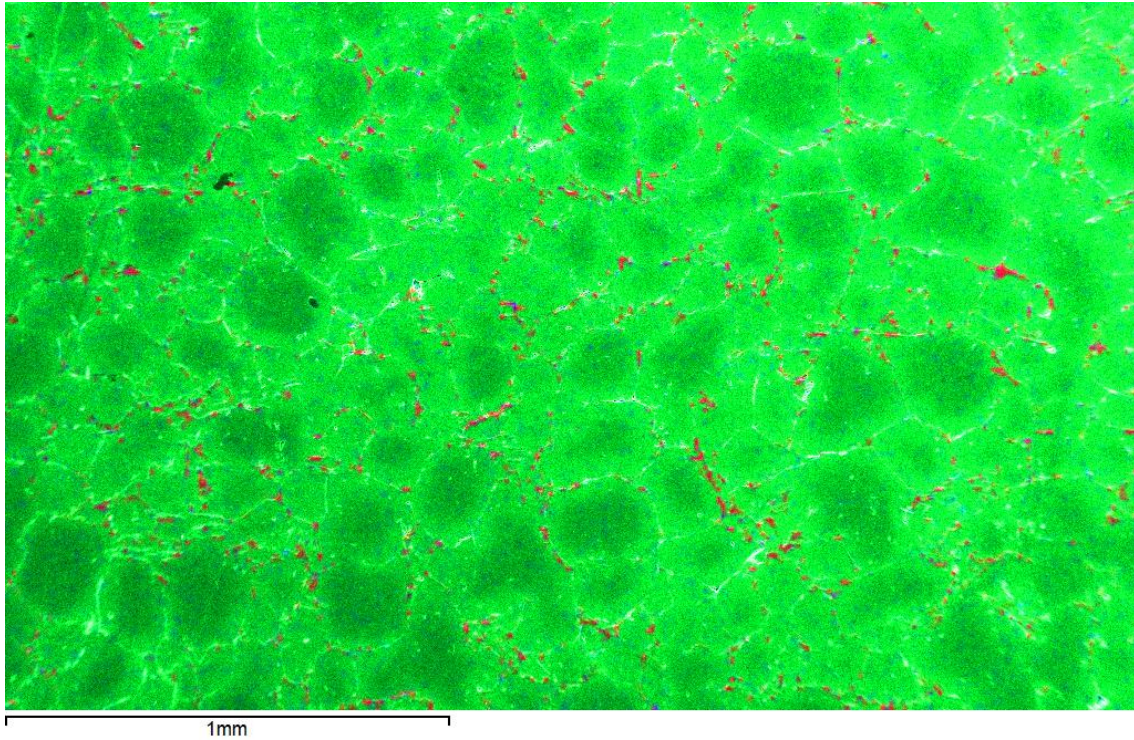
1mm

(a)



1mm

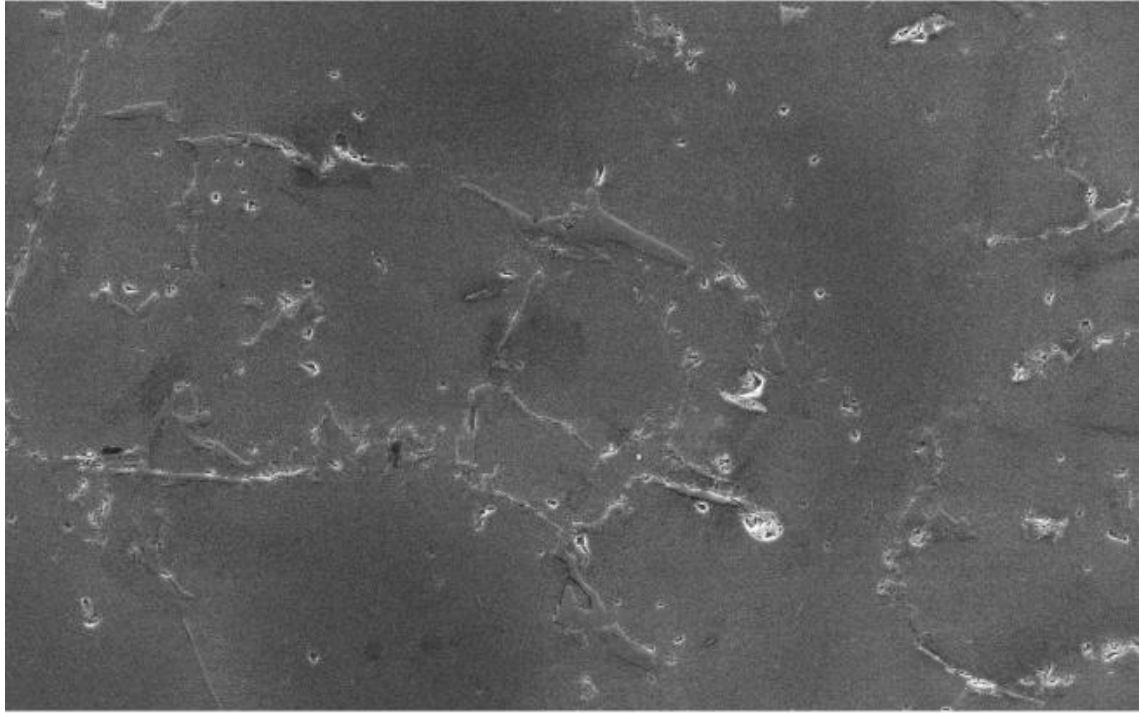
(b)



(c)

Figure 6.15 EDS mapping results at X50 magnification for A356 samples reinforced with UST + 1% SiC during solidification: (a) Al (in green) and Si (in red) elements (b) Al (in green) and C (in red) elements (c) Al (in green), Si (in red) and C (in blue) elements

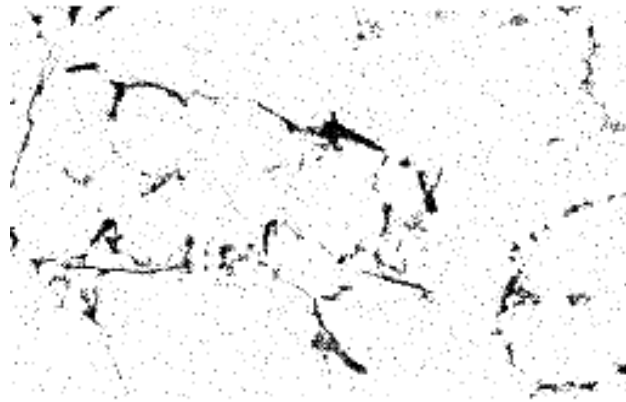
Figure 6.16 shows the distribution of SiC nanoparticles in the A356 samples reinforced with UST + 1% SiC during solidification at X200 magnification. The EDS analysis has been performed only for the SiC reinforced A356 nanocomposite. Similar conclusion can be made from Figure 6.16, that is, the SiC nanoparticles are dispersed reasonably well into the A356 matrix. Figure 6.16 (e) shows the EDS spectrum result of C element in the A356 nanocomposites, in which Si and C are both detected in the nanocomposite sample. The only possible source of the C showed in the EDS spectrum is from the SiC nanoparticle addition.



300 $\mu$ m

Electron Image 1

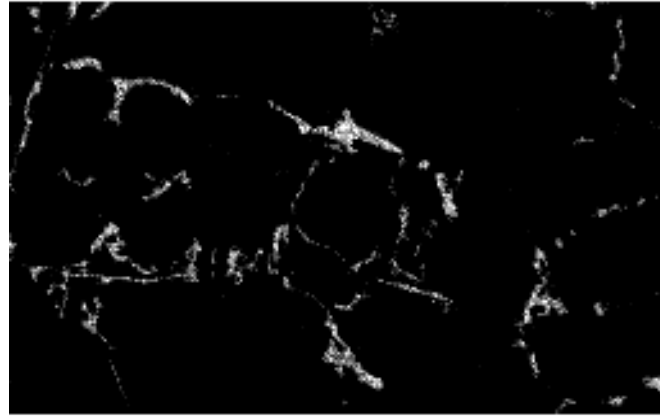
(a)



300 $\mu$ m

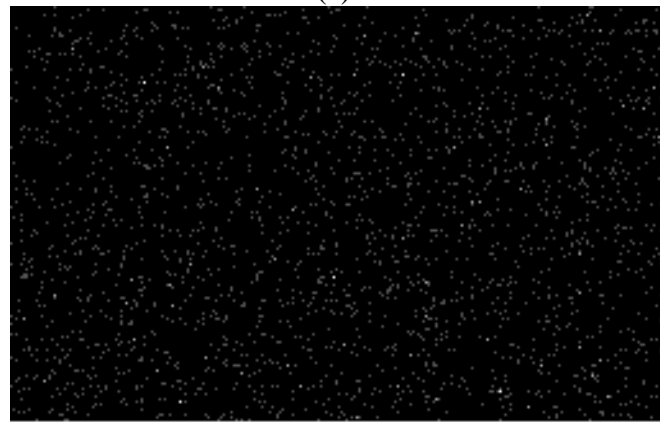
Al K $\alpha$ 1

(b)



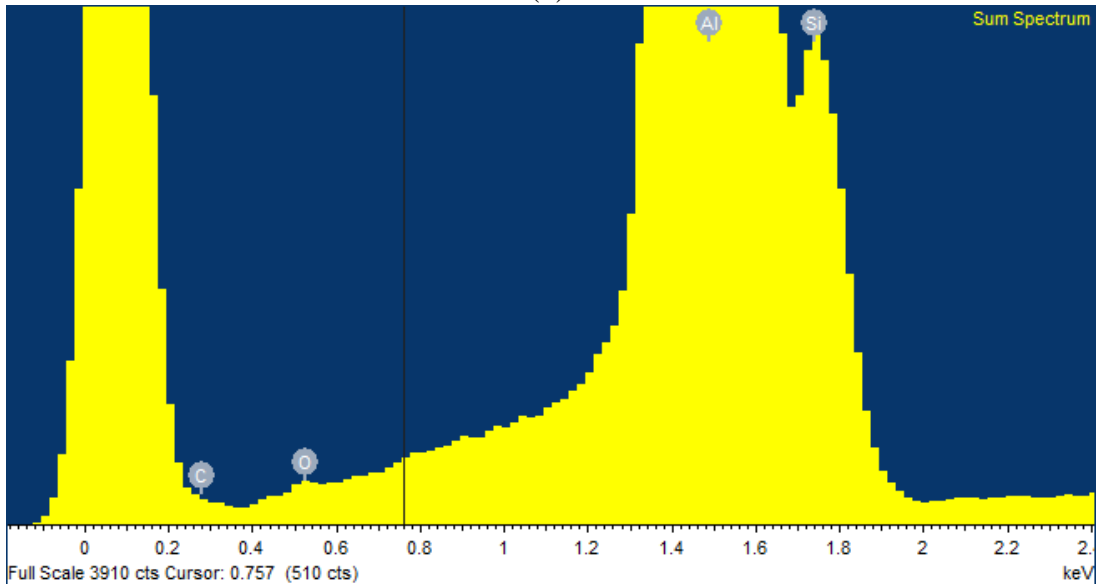
300µm Si Ka1

(c)



300µm C Ka1\_2

(d)



(e)

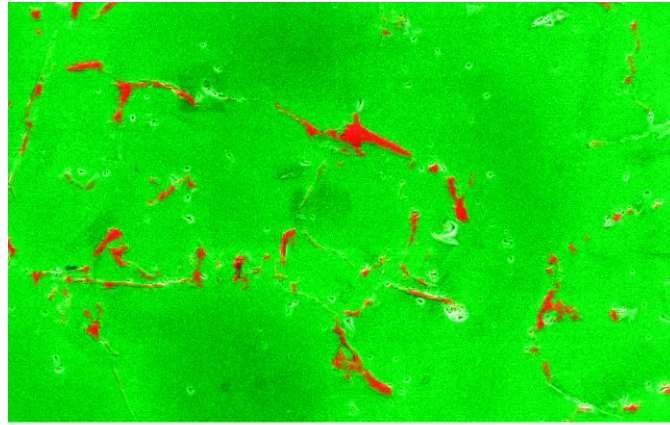
Figure 6.16 SEM results at X200 magnification for A356 samples reinforced with UST + 1% SiC during solidification: (a) SEM pictures (b) EDS mapping result for Al element (c) EDS mapping result for Si element (d) EDS mapping result for C element (e) EDS spectrum result

SEM/EDS spectrum result usually does not provide sufficient accuracy to solve critical problems, for example, determining the formula of a compound. However, in this study, the EDS spectrum result shown in Table 6.4 agrees well with the experiment condition. In these experiments, the A356 alloy consists of about 7% of Si element and 1% of SiC nanoparticle. Also, some oxidation, which is possible to occur during the process, explains the oxygen content.

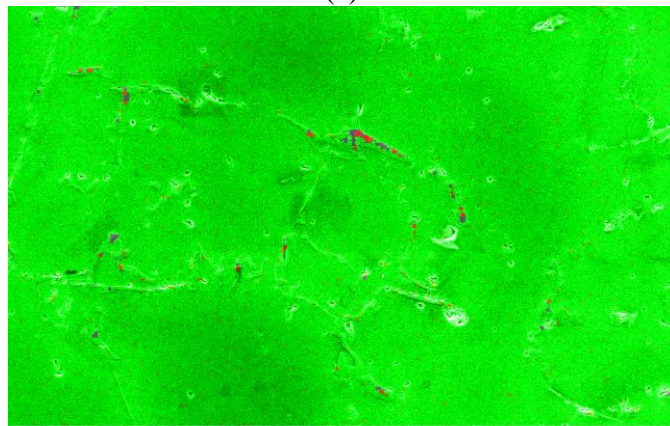
Table 6.4 EDS spectrum result

Element	Intensity	Weight%	Weight% Sigma	Atomic%
Si K	0.1592	8.64	1.61	17.43
O K	0.6090	0.89	0.21	1.35
Al K	1.3101	89.68	1.60	80.54
C		0.78	0.20	0.68
Totals		100.00		100.00

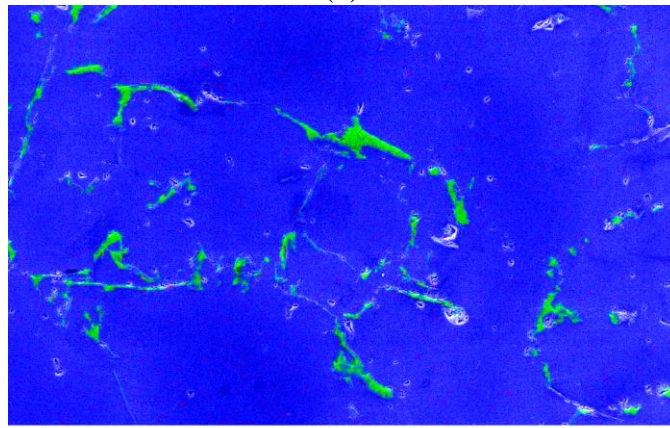
Figure 6.17 shows the combined EDS mapping results of different elements at 200X magnification. Figure 6.17 shows the same results as those in Figure 6.15, which is, the C element tends to gather around the grain boundary area, which is Si eutectic phase. This confirms the literature result [127] about the interfaces between the SiC particles and the alloy matrix. The SEM observation of the polished and etched A356 - 10%SiC samples revealed that the SiC particles appeared to act as substrates for the nucleation of the Si phase. Many Si crystals were observed to be attached to the surface of the SiC particles, further supporting the observation that the Si phase nucleated heterogeneously from the SiC particles. In the present study, for the A356 samples, SiC and Al<sub>2</sub>O<sub>3</sub> nanoparticles may both act as substrates for the nucleation of the Si phase.



(a)



(b)



(c)

Figure 6.17 EDS mapping results at X50 magnification for A356 samples reinforced with UST + 1% SiC during solidification: (a) Al (in green) and Si (in red) elements (b) Al (in green) and C (in red) elements (c) Al (in blue), Si (in green) and C (in red) elements

## CHAPTER 7 – CONCLUSIONS AND RECOMMENDATIONS FOR FUTURE WORK

### 7.1 Conclusions

By using SEM and EDS analyses, it is shown that the nanoparticles are dispersed reasonably well in the metal matrix; but some insignificant agglomeration still occurs. In the A356 alloy matrix, SiC nanoparticles tend to gather around grain boundary area which is mostly the Si eutectic phase. The SiC and Al<sub>2</sub>O<sub>3</sub> nanoparticles may act as substrates for the nucleation of the Si phase. In the 6061 alloy matrix, where the Si composition is very low, the nanoparticle distribution does not indicate similar phenomena.

This agglomeration could happen during UST processing and/or during solidification. The CFD modeling results demonstrate that the nanoparticles would be well dispersed after 3.0 sec into the molten alloy. Thus, based on the assumption that the nanoparticles will not be significantly agglomerated during the solidification process, a finely dispersed nanocomposite can be obtained.

It was determined for the as-cast 6061 samples that the tensile strength remains almost the same while a significant improvement in the ductility of the as-cast 6061 nanocomposite was achieved after the addition of the Al<sub>2</sub>O<sub>3</sub>/SiC ceramic nanoparticles via ultrasonic processing. The addition of these nanoparticles in the 6061 alloy matrix certainly changed the fracture mechanism from brittle dominated to ductile dominated. The tensile strength of the as-cast A356 samples increases after the UST treatment and the addition of the nanoparticles, and the elongation of these samples shows diverse changes.

The CFD modeling results also reveal that the injection position will not significantly affect the final distribution of the SiC nanoparticles as long as the flow is strong enough to disperse the nanoparticles.

## 7.2 Main Contributions of This Study

The main contributions of this study are summarized below:

1. The UST equipment and procedures were developed and applied to the fabrication of aluminum based alloy and nanocomposites (MMNC).
2. A detailed literature review was performed, which revealed the UST effects on the molten metal and solidification processing aspects as well as recent advances in the fabrication process of the MMNCs. The UST effects included degassing, refinement of the primary phase, modification of the eutectic phase, dispersing of the reinforcement nanoparticles, and improving of the wettability of the nanoparticles.
3. A variety of types of nanoparticles were used as reinforcement nanoparticles such as  $\beta$ -SiC,  $\text{Al}_2\text{O}_3$ , ZrC, TiN,  $\text{TiB}_2$  and MWCNTs. It was determined that the optimum type and amount of nanoparticles were 1 wt. % SiC and 1 wt. %  $\text{Al}_2\text{O}_3$ . The role of nanoparticles in the nucleation and the strengthening of the matrix was determined as well. The strengthening mechanisms were determined based on careful comparisons of the microstructure and properties with and without the addition of the nanoparticles. The strengthening mechanisms included thermal mismatch between the reinforcements and matrix, Orowan looping between nanoparticles and slip mode transition produced by the presence of the nanoparticles. The weakening mechanisms included the agglomeration of nanoparticles and microporosity brought in by nanoparticles and interfacial bonding between nanoparticles and Si phase.

4. In most of the proposed experiments, high superheat values similar to those used in the industrial practice have been applied. Three sets of experiments were also performed during solidification at low superheat: (1) without UST, (2) with UST and (3) with UST and nanoparticles. Detailed metallurgical characterization of the samples produced with this method was performed and discussed.

5. Several novel methods of adding nanoparticles into the molten alloys were investigated to better suit the requirements of the scale-up work of fabricating MMNC. It was found the location of the insertion of the nanoparticles is not critical to the nanodispersion. Similar results were found by using the CFD nanodispersion model.

6. The applied UST parameters in the studied experiments were used to validate the developed multiphase CFD model available in the Solidification Lab. This model can simulate cavitation and nanoparticle dispersion during UST processing. A parametric study using this model has been performed and the results were used to further improve the proposed experimental methods.

### 7.3 Recommendations for Future Work

Future work can include Scanning Transmission Electron Microscopy (STEM) analysis of the as-cast A356/6061 nanocomposites to clearly understand the effects of the ultrasonic cavitation processing on the dispersion of the nanoparticles and the interaction between the metal matrix and the nanoparticles. Also, the T6 heat treatment process needs to be optimized and the T6 heat treated samples compared with the as-cast samples. The CFD nanodispersion model will be further enhanced adding a solidification model with PEP and Brownian motion effects and entrapment between dendritic structures and validated against the experiments performed in this study. The dominant strengthening mechanism should to be determined. Also, a numerical

strengthening model, which accounts for all the possible strengthening mechanisms, should be developed.

Additional experiments on ultrasonic stirring of A356/6061 alloys will need to be conducted at the University of Alabama at Tuscaloosa, Solidification Laboratory, to advance the current understanding of the influence of ultrasonic cavitation and acoustic streaming on the microstructure evolution of alloys under both high and low superheat conditions. The developed UST modeling capability in the Solidification Laboratory should be enhanced to study the globular/dendritic transition in alloys that are solidifying in the presence of ultrasonic stirring at low and high superheat.

## REFERENCES

- [1] S. Jia, X. Liu, L. Nastac, Ultrasonic Stirring Effects on the Microstructure of A356 Alloys, Proceedings of the Advanced Casting Technologies Symposium, MS&T, (2012) 112-119, (ISBN-13: 978-0-87339-761-2).
- [2] X. Liu, S. Jia, L. Nastac, On Ultrasonic Cavitation-assisted Molten Metal Processing of A356-Nanocomposites, Proc. of the MS&T 2012 Conference, (2012) 120-127, (ISBN-13: 978-0-87339-761-2).
- [3] X. Liu, S. Jia, L. Nastac, Ultrasonic Processing of A356-Nanocomposite Castings, Proceedings of the AFS Casting Congress, 117th Metalcasting Congress, 13(1382) (2013) 1-6, (ISBN 978-0-87433-403-6).
- [4] S. Jia, X. Liu, L. Nastac, Ultrasonic Stirring Effects on the Microstructure of A356 Castings, Proceedings of the AFS Casting Congress, 117th Metalcasting Congress, 13(1383) (2013) 1-7, (ISBN 978-0-87433-403-6).
- [5] L. Nastac, X. Liu, S. Jia, Advances on Ultrasonic Cavitation-Assisted Molten Metal Processing of Metal-Matrix-Nano-Composites, Proc. of the 21st Intern. Conference on Composites/Nano Engineering (ICCE - 21), Ed. D. Hui (2013).
- [6] S. Jia, L. Nastac, The Influence of Ultrasonic Stirring on the Solidification Microstructure and Mechanical Properties of A356 Alloy, Chemical and Material Engineering, 1(3) (2013) 69-73, (DOI: 10.13189/cme.2013.010301).
- [7] X. Liu, S. Jia, L. Nastac, Ultrasonic Cavitation-Assisted Molten Metal Processing of Cast A356-Nanocomposites, International Journal of Metal Casting (AFS), 8(1) (2013) 1-12.
- [8] L. Nastac, S. Jia, D. Zhang, Advances on Ultrasonic Processing of Alloys and Nanocomposites, Proceedings of the 1st International Caparica Conference on Ultrasonics based applications: from analysis to synthesis, (2014) 59, (ISBN: 978-989-98793-3-1).
- [9] S. Jia, D. Zhang, L. Nastac, Experimental and Numerical Analysis of the 6061-Based Nanocomposites Fabricated via Ultrasonic Processing, J Mater Eng Perform, 24(6) (2015) 2225-2233, (DOI: 10.1007/s11665-015-1467-4).

- [10] T.V. Atamanenko, D.G. Eskin, L. Katgerman, Structure Refinement by Means of Ultrasonic Cavitation Melt Treatment, Proceedings of the 10th Australasian Conference Aluminium Cast House Technology, (2007) 139-146.
- [11] T.V. Atamanenko, D.G. Eskin, L. Katgerman, Influence of ultrasonic melt treatment on structure formation in aluminium alloys with high amount of transition metals, Light Metals, (2009) 827-830.
- [12] K.M. Mussert, W.P. Vellinga, A. Bakker, S. Van Der Zwaag, A nano-indentation study on the mechanical behaviour of the matrix material in an AA6061 - Al<sub>2</sub>O<sub>3</sub> MMC, J Mater Sci, 37 (2002) 789-794.
- [13] K. Akio, O. Atsushi, K. Toshiro, T. Hiroyuki, Fabrication Process of Metal Matrix Composite with Nano-size SiC Particle Produced by Vortex Method, J. Jpn. Inst. Light Met., 49 (1999) 149-154.
- [14] X.F. Chen, E.G. Baburai, F.H. Froes, A. Vassel, Ti-6Al-4V/SiC Composites by Mechanical Alloying and Hot Isostatic Pressing, Proc. Adv. Part. Mater. Processes, (1997) 185–192.
- [15] S.L.U. Filho, R. Rodriguez, J.C. Earthman, E.J. Lavernia, Synthesis of Diamond Reinforced Al-Mg Nanocrystalline Composite Powder Using Ball Milling, Mater. Sci. Forum, 416-418 (2003) 213–218.
- [16] J.R. Groza, Sintering of nanocrystalline powders, Int. J. Powder Metall., 35 (1999) 59–66.
- [17] X. Jian, H. Xu, T.T. Meek, Q. Han, Effect of power ultrasound on solidification of aluminum A356 alloy, Materials Letters, 59 (2005) 190-193.
- [18] W. Khalifa, Y. Tsunekawa, M. Okumiya, Effect of ultrasonic melt treatment on microstructure of A356 aluminium cast alloys, Int. J. Cast. Metals Res., 21 (2008) 129-134.
- [19] G.I. Eskin, Effect of ultrasonic (cavitation) treatment of the melt on the microstructure evolution during solidification of aluminum alloy ingots, Zeitschrift für Metallkunde, 93 (2002) 502-507.
- [20] H. Xu, X. Jian, T.T. Meek, Q. Han, Degassing of Molten Aluminum A356 Alloy Using Ultrasonic Vibration, Materials Letters, 58 (2004) 3669–3673.
- [21] T.T. Meek, X. Jian, H. Xu, Q. Han, Ultrasonic processing of materials, in, US Department of Energy, Washington DC, USA, 2006.
- [22] J. Lan, Y. Yang, X. Li, Microstructure and microhardness of SiC nanoparticles reinforced magnesium composites fabricated by ultrasonic method, Materials Science and Engineering: A, 386 (2004) 284-290.

- [23] G. Cao, H. Choi, H. Konishi, S. Kou, R. Lakes, X. Li, Mg–6Zn/1.5%SiC nanocomposites fabricated by ultrasonic cavitation-based solidification processing, *J Mater Sci*, 43 (2008) 5521-5526.
- [24] J. Yan, Z. Xu, L. Shi, X. Ma, S. Yang, Ultrasonic assisted fabrication of particle reinforced bonds joining aluminum metal matrix composites, *Mater Design*, 32 (2011) 343-347.
- [25] T. Hielscher, Ultrasonic Production of Nano-Size Dispersions and Emulsions, in: *Dans European Nano Systems Workshop - ENS 2005*, Paris, France, 2005.
- [26] L. Nastac, Mathematical Modeling of the Solidification Structure Evolution in the Presence of Ultrasonic Stirring, *Metallurgical and Materials Transactions B*, 42 (2011) 1297-1305.
- [27] R.A. Saravanan, M.K. Surappa, Fabrication and characterisation of pure magnesium-30 vol.% SiCP particle composite, *Materials Science and Engineering A*, 276 (2000) 108-116.
- [28] M. Gupta, M.O. Lai, D. Saravananathan, Synthesis, microstructure and properties characterization of disintegrated melt deposited Mg/SiC composites, *J Mater Sci*, 35 (2000) 2155-2165.
- [29] S. Ugandhar, M. Gupta, S.K. Sinha, Enhancing strength and ductility of Mg/SiC composites using recrystallization heat treatment, *Composite Structures*, 72 (2006) 266-272.
- [30] M. Gupta, L. Lu, M.O. Lai, K.H. Lee, Microstructure and mechanical properties of elemental and reinforced magnesium synthesized using a fluxless liquid-phase process, *Materials Research Bulletin*, 34 (1999) 1201-1214.
- [31] S. Seshan, M. Jayamathy, S.V. Kailas, T.S. Srivatsan, The tensile behavior of two magnesium alloys reinforced with silicon carbide particulates, *Materials Science and Engineering A*, 363 (2003) 345-351.
- [32] S.C. Tjong, Novel Nanoparticle-Reinforced Metal Matrix Composites with Enhanced Mechanical Properties, *Advanced Engineering Materials*, 9 (2007) 639-652.
- [33] K. Chawla, *Metal Matrix Composites*, in: *Composite Materials*, Springer New York, 1998, 164-211.
- [34] D.B. Miracle, Metal matrix composites – From science to technological significance, *Compos Sci Technol*, 65 (2005) 2526-2540.
- [35] D.E. Alman, Properties of metal matrix composites, in: *ASM Handbook*, 21: Composites, ASM International, Metals Park, Ohio, 2001, 838-858.
- [36] Z.Y. Ma, Y.L. Li, Y. Liang, F. Zheng, J. Bi, S.C. Tjong, Nanometric Si<sub>3</sub>N<sub>4</sub> particulate-reinforced aluminum composite, *Materials Science and Engineering A*, 219 (1996) 229-231.

- [37] D.C. Jia, Influence of SiC particulate size on the microstructural evolution and mechanical properties of Al-6Ti-6Nb matrix composites, *Materials Science and Engineering: A*, 289 (2000) 83-90.
- [38] H. Ferkel, B.L. Mordike, Magnesium strengthened by SiC nanoparticles, *Materials Science and Engineering: A*, 298 (2001) 193-199.
- [39] Y.C. Kang, S.L.I. Chan, Tensile properties of nanometric Al<sub>2</sub>O<sub>3</sub> particulate-reinforced aluminum matrix composites, *Mater Chem Phys*, 85 (2004) 438-443.
- [40] L. Lü, M.O. Lai, W. Liang, Magnesium nanocomposite via mechanochemical milling, *Compos Sci Technol*, 64 (2004) 2009-2014.
- [41] S.F. Hassan, M. Gupta, Development of high performance magnesium nano-composites using nano-Al<sub>2</sub>O<sub>3</sub> as reinforcement, *Materials Science and Engineering: A*, 392 (2005) 163-168.
- [42] S.C. Tjong, Z.Y. Ma, Microstructural and mechanical characteristics of in situ metal matrix composites, *Materials Science and Engineering: R: Reports*, 29 (2000) 49-113.
- [43] R.Z. Valiev, Structure and mechanical properties of ultrafine-grained metals, *Materials Science and Engineering: A*, 234-236 (1997) 59-66.
- [44] V.V. Stolyarov, Y.T. Zhu, T.C. Lowe, R.K. Islamgaliev, R.Z. Valiev, Processing nanocrystalline Ti and its nanocomposites from micrometer-sized Ti powder using high pressure torsion, *Materials Science and Engineering: A*, 282 (2000) 78-85.
- [45] C.S. Goh, J. Wei, L.C. Lee, M. Gupta, Simultaneous enhancement in strength and ductility by reinforcing magnesium with carbon nanotubes, *Materials Science and Engineering: A*, 423 (2006) 153-156.
- [46] P. Rohatgi, B. Schultz, Light weight metal matrix composites - Stretching the boundaries of metals, *Material Matters*, 2 (2007) 16-19.
- [47] M. Karbalaei Akbari, H.R. Baharvandi, K. Shirvanimoghaddam, Tensile and fracture behavior of nano/micro TiB<sub>2</sub> particle reinforced casting A356 aluminum alloy composites, *Materials and Design*, 66 (2014) 150-161.
- [48] Y. Han, K. Li, J. Wang, D. Shu, B. and Sun, Influence of high-intensity ultrasound on grain refining performance of Al-5Ti-1B master alloy on aluminium, *Materials Science and Engineering A* 405 (2005) 306-312.
- [49] B.E. Noltingk, E.A., Cavitation produced by ultrasonics, *Proc. Phys. Soc., London*, 63B, (1950) 674-685.
- [50] A. Prosperetti, Bubble phenomena in sound fields: part one and part two, *Ultrasonics*, 22 (1984) 69-77 and 115-124.

- [51] C.E. Brennen, *Cavitation and Bubble Dynamics*, Oxford University Press, 1995.
- [52] G.I. Eskin, *Ultrasonic Treatment of Light Alloy Melts*, Gordon & Breach, Amsterdam, 1998.
- [53] V.O. Abramov, O.V. Abramov, F. Sommer, D. Orlov, Properties of Al-Pb base alloys applying electromagnetic forces and ultrasonic vibration during casting, *Materials Letters*, 23 (1995) 17-20.
- [54] V. Abramov, O. Abramov, V. Bulgakov, F. Sommer, Solidification of aluminium alloys under ultrasonic irradiation using water-cooled resonator, *Materials Letters*, 37 (1998) 27-34.
- [55] G. I. Eskin, Broad prospects for commercial application of the ultrasonic (cavitation) melt treatment of light alloys., *Ultrasonics Sonochemistry*, 8 (2001) 319–325.
- [56] G.I. Eskin, *Ultrasonics Sonochemistry*, 1 (1994) S59.
- [57] G.I. Eskin, *Ultrasonics Sonochemistry*, 8 (2001) S319.
- [58] T.T. Meek, Q. Han, *Ultrasonic Processing of Materials.*, Final DOE Technical report, Oak Ridge National Laboratory, 2006.
- [59] G.I. Eskin, *Principles of Ultrasonic Treatment: Application for Light Alloys Melts*, *Advanced Performance Materials*, 4 (1997) 223-232.
- [60] S.L. Hem, The Effect of Ultrasonic Vibrations on Crystallization Processes, *Ultrasonics*, 5 (1967) 202-207.
- [61] E.A. Neppiras, B.E. Noltingk, Cavitation produced by ultrasonics: theoretical conditions for the onset of cavitation., *Proc. Phys. Soc., London*, 64B (1951) 1032--1038.
- [62] G.I. Eskin, Influence of cavitation treatment of melts on the processes of nucleation and growth of crystals during solidification of ingots and castings from light alloys, *Ultrasonics Sonochemistry*, 1 (1994) S59-S56.
- [63] J. Lee, Kentish, S., Matula, T.J. and Ashokkumar, M., Effect of surfactants on inertial cavitation activity in a pulsed acoustic field, *Journal of Physical Chemistry B*, 109 (2005) 16860-16865.
- [64] O.V. Abramov, *Ultrasound in Liquid and Solid Metals*, CRC Press, Boca Raton, 1994.
- [65] L. Zhang, *ultrasonic processing of aluminum alloys*, Delft University of Technology, 2013.

- [66] G.I. Eskin, D.G. Eskin, Effects of ultrasonic (cavitation) melt processing on the structure refinement and property improvement of cast and worked aluminium alloys, *Materials Science Forum*, 396-402 (2002) 77-82.
- [67] D. M. Herlach, K. Eckler, A. Karma, M. Schwarz, Grain Refinement Through Fragmentation of Dendrites in Undercooled Melts, *Materials Science and Engineering A*, 304-306 (2001) 20-25.
- [68] H. Yasuda, N. Nakatsuka, T. Nagira, A. Sugiyama, M. Yoshiya, K. Uesugi, K. Umetani, X-ray imaging study on grain refinement due to dendrite fragmentation, *Proc. 6th Electromagnetic Processing of Materials*, (2009) 257-260.
- [69] M. Li, G. Yang, Y. Zhou, Direct observation of fragments of primary dendrite from undercooled Fe-Co alloys, *Journal of Crystal Growth*, 204 (1999) 413-417.
- [70] H. Yasuda, Y. Yamamoto, N. Nakatsuka, T. Nagira, M. Yoshiya, A. Sugiyama, I. Ohnaka, K. Umetani, K. Uesugi, In Situ Observation of Nucleation, Fragmentation and Microstructure Evolution In Sn-Bi And Al-Cu Alloys, *International Journal of Cast Metals Research*, 21 (2008) 125-128.
- [71] D. Ruvalcaba, R.H. Mathiesen, D.G. Eskin, L. Arnberg, L. Katgerman, In Situ Observation of Dendritic Fragmentation Due to Local Solute-Enrichment during Directional Solidification of an Aluminum Alloy, *Acta Materialia*, 55 (2007) 4287-4292.
- [72] D.M. Stefanescu, *Science and Engineering of Casting Solidification*, New York : Springer Oct. 2008 2nd ed., 2008.
- [73] Y. Yang, J. Lan, X. Li, Study on bulk aluminum matrix nano-composite fabricated by ultrasonic dispersion of nano-sized SiC particles in molten aluminum alloy, *Materials Science and Engineering: A*, 380 (2004) 378-383.
- [74] S. Mula, P. Padhi, S.C. Panigrahi, S.K. Pabi, S. Ghosh, On structure and mechanical properties of ultrasonically cast Al-2% Al<sub>2</sub>O<sub>3</sub> nanocomposite, *Materials Research Bulletin*, 44 (2009) 1154-1160.
- [75] L. Zeng, Q. Zhou, M.P. De Cicco, X. Li, S. Zhou, Quantifying boundary effect of nanoparticles in metal matrix nanocomposite fabrication processes, *IIE Transactions*, 44 (2011) 551-567.
- [76] M.A. Azouni, P. Casses, Thermophysical properties effects on segregation during solidification, *Advances in Colloid and Interface Science*, 75 (1998) 83-106.
- [77] M. Azizieh, H.S. Kim, A.H. Kokabi, P. Abachi, B.K. Shahraki, Fabrication of AZ31/Al<sub>2</sub>O<sub>3</sub> Nanocomposites by Friction Stir Processing, *Reviews on Advanced Materials Science*, 28 (2011) 85-89.

- [78] F. Tang, M. Hagiwara, J.M. Schoenung, Microstructure and tensile properties of bulk nanostructured Al-5083/SiCp composites prepared by cryomilling, *Materials Science and Engineering: A*, 407 (2005) 306-314.
- [79] F. Tang, M. Hagiwara, J.M. Schoenung, Formation of coarse-grained inter-particle regions during hot isostatic pressing of nanocrystalline powder, *Scripta Materialia*, 53 (2005) 619-624.
- [80] F.Y.C. Boey, Z. Yuan, K.A. Khor, Mechanical alloying for the effective dispersion of sub-micron SiCp reinforcements in Al-Li alloy composite, *Materials Science and Engineering: A*, 252 (1998) 276-287.
- [81] C. Suryanarayana, Mechanical alloying and milling, *Progress in Materials Science*, 46 (2001) 1-184.
- [82] F. Zhou, X.Z. Liao, Y.T. Zhu, S. Dallek, E.J. Lavernia, Microstructural evolution during recovery and recrystallization of a nanocrystalline Al-Mg alloy prepared by cryogenic ball milling, *Acta Materialia*, 51 (2003) 2777-2791.
- [83] B.Q. Han, J. Ye, F. Tang, J. Schoenung, E.J. Lavernia, Processing and behavior of nanostructured metallic alloys and composites by cryomilling, *J Mater Sci*, 42 (2007) 1660-1672.
- [84] N. Valibeygloo, R. Azari Khosroshahi, R. Taherzadeh Mousavian, Microstructural and mechanical properties of Al-4.5wt% Cu reinforced with alumina nanoparticles by stir casting method, *Int J Miner Metall Mater*, 20 (2013) 978-985.
- [85] M. Karbalaei Akbari, H.R. Baharvandi, O. Mirzaee, Nano-sized aluminum oxide reinforced commercial casting A356 alloy matrix: Evaluation of hardness, wear resistance and compressive strength focusing on particle distribution in aluminum matrix, *Composites Part B: Engineering*, 52 (2013) 262-268.
- [86] H. Su, W. Gao, Z. Feng, Z. Lu, Processing, microstructure and tensile properties of nano-sized Al<sub>2</sub>O<sub>3</sub> particle reinforced aluminum matrix composites, *Mater Design*, 36 (2012) 590-596.
- [87] M. Ghahremanian, B. Niroumand, M. Panjepour, Production of Al-Si-SiCp cast composites by injection of low-energy ball-milled Al-SiCp powder into the melt, *Met. Mater. Int.*, 18 (2012) 149-156.
- [88] S. Amirkhanlou, B. Niroumand, Synthesis and characterization of 356-SiCp composites by stir casting and compocasting methods, *Transactions of Nonferrous Metals Society of China*, 20, Supplement 3 (2010) s788-s793.
- [89] S. Amirkhanlou, B. Niroumand, Development of Al356/SiCp cast composites by injection of SiCp containing composite powders, *Mater Design*, 32 (2011) 1895-1902.
- [90] S. Kamrani, R. Riedel, S.M. Seyed Reihani, H.J. Kleebe, Effect of reinforcement volume fraction on the mechanical properties of Al<sub>3</sub>-SiC nanocomposites produced by mechanical alloying and consolidation, *J Compos Mater*, 44 (2010) 313-326.

- [91] S.H. Hwang, D.S. Bang, K.H. Yoon, Y.B. Park, D.Y. Lee, S.S. Jeong, Fabrication and characterization of aluminum-carbon nanotube powder and polycarbonate/aluminum-carbon nanotube composites, *J Compos Mater*, 44 (2010) 2711-2722.
- [92] M.K. Habibi, K.S. Tun, M. Gupta, An investigation into the effect of ball milling of reinforcement on the enhanced mechanical response of magnesium, *J Compos Mater*, (2011) 0021998311401098.
- [93] Z.A. Munir, U. Anselmi-Tamburini, M. Ohyanagi, The effect of electric field and pressure on the synthesis and consolidation of materials: A review of the spark plasma sintering method, *J Mater Sci*, 41 (2006) 763-777.
- [94] G. Salvatore, S. Yoshio, M. Giovanni, Electric current activated/assisted sintering ( ECAS ): a review of patents 1906–2008, *Science and Technology of Advanced Materials*, 10 (2009) 053001.
- [95] N. Saheb, Z. Iqbal, A. Khalil, Spark Plasma Sintering of Metals and Metal Matrix Nanocomposites: A Review, *J Nanomater*, 2012 (2012) 1.
- [96] W.W.L. Eugene, M. Gupta, Characteristics of Aluminum and Magnesium Based Nanocomposites Processed Using Hybrid Microwave Sintering, *Journal of Microwave Power and Electromagnetic Energy*, 44 (2010) 14-27.
- [97] S.F. Hassan, M. Gupta, Development of nano-Y<sub>2</sub>O<sub>3</sub> containing magnesium nanocomposites using solidification processing, *J Alloy Compd*, 429 (2007) 176-183.
- [98] S. Zhou, X. Zhang, Z. Ding, C. Min, G. Xu, W. Zhu, Fabrication and tribological properties of carbon nanotubes reinforced Al composites prepared by pressureless infiltration technique, *Composites Part A: Applied Science and Manufacturing*, 38 (2007) 301-306.
- [99] K.F. Ho, M. Gupta, Development of Al–Mg based composites containing nanometric alumina using the technique of disintegrated melt deposition, *J. Metast. Nanocryst. Mater*, 23 (2005) 159-162.
- [100] N. Srikanth, H.K.F. Calvin, M. Gupta, Effect of length scale of alumina particles of different sizes on the damping characteristics of an Al–Mg alloy, *Materials Science and Engineering: A*, 423 (2006) 189-191.
- [101] D. Gu, Y.C. Hagedorn, W. Meiners, K. Wissenbach, R. Poprawe, Nanocrystalline TiC reinforced Ti matrix bulk-form nanocomposites by Selective Laser Melting (SLM): Densification, growth mechanism and wear behavior, *Compos Sci Technol*, 71 (2011) 1612-1620.
- [102] Q. Li, C.A. Rottmair, R.F. Singer, CNT reinforced light metal composites produced by melt stirring and by high pressure die casting, *Compos Sci Technol*, 70 (2010) 2242-2247.

- [103] Y.Q. Liu, H.T. Cong, W. Wang, C.H. Sun, H.M. Cheng, AlN nanoparticle-reinforced nanocrystalline Al matrix composites: Fabrication and mechanical properties, *Materials Science and Engineering: A*, 505 (2009) 151-156.
- [104] Q. Li, A. Viereckl, C.A. Rottmair, R.F. Singer, Improved processing of carbon nanotube/magnesium alloy composites, *Compos Sci Technol*, 69 (2009) 1193-1199.
- [105] B. Abbasipour, B. Niroumand, S.M. Monir Vaghefi, Compocasting of A356-CNT composite, *Transactions of Nonferrous Metals Society of China*, 20 (2010) 1561-1566.
- [106] A.B. Elshalakany, T.A. Osman, A. Khattab, B. Azzam, M. Zaki, Microstructure and Mechanical Properties of MWCNTs Reinforced A356 Aluminum Alloys Cast Nanocomposites Fabricated by Using a Combination of Rheocasting and Squeeze Casting Techniques, *Journal of Nanomaterials*, (2014) 386370.
- [107] Z. Zhang, D.L. Chen, Contribution of Orowan strengthening effect in particulate-reinforced metal matrix nanocomposites, *Materials Science and Engineering: A*, 483-484 (2008) 148-152.
- [108] Z. Zhang, D.L. Chen, Consideration of Orowan strengthening effect in particulate-reinforced metal matrix nanocomposites: A model for predicting their yield strength, *Scripta Materialia*, 54 (2006) 1321-1326.
- [109] A. Sanaty-Zadeh, Comparison between current models for the strength of particulate-reinforced metal matrix nanocomposites with emphasis on consideration of Hall-Petch effect, *Materials Science and Engineering: A*, 531 (2012) 112-118.
- [110] P. Luo, D.T. McDonald, W. Xu, S. Palanisamy, M.S. Dargusch, K. Xia, A modified Hall-Petch relationship in ultrafine-grained titanium recycled from chips by equal channel angular pressing, *Scripta Materialia*, 66 (2012) 785-788.
- [111] V.C. Nardone, K.M. Prewo, On the strength of discontinuous silicon carbide reinforced aluminum composites, *Scripta Metallurgica*, 20 (1986) 43-48.
- [112] D. Hull, D.J. Bacon, *Introduction to dislocations*, Butterworth-Heinemann, Oxford; Burlington, MA, 2011.
- [113] L. Nastac, Numerical Modeling of Fluid Flow and Solidification Characteristics of Ultrasonically Processed A356 Alloys, *ISIJ International*, 54 (2014) 1830-1835.
- [114] D. Zhang, L. Nastac, Numerical modeling of the dispersion of ceramic nanoparticles during ultrasonic processing of aluminum-based nanocomposites, *Journal of Materials Research and Technology*, 3 (2014) 296-302.

- [115] D. Zhang, S. Jia, P. Allison, a.L. Nastac, Numerical Modeling of the Dispersion of Ceramic Nanoparticles during Ultrasonic Processing of 6061-based Nanocomposites, Proceedings of the Advanced Metal Casting Technologies Symposium, MS&T, (2014) 695-702, (ISBN-13: 978-0-87339-763-6).
- [116] L. Nastac, Multiscale Modeling of the Solidification Microstructure Evolution in the Presence of Ultrasonic Stirring, IOP Conference Series: Materials Science and Engineering, 33 (2012) 012079.
- [117] Fluent 6.3: User's Guide Manual, in, Fluent Inc. and ANSYS's Fluent, 2006.
- [118] J.K. Kim, P.K. Rohatgi, An analytical solution of the critical interface velocity for the encapsuring of insoluble particles by a moving solid/liquid interface, Metallurgical and Materials Transactions A, 29 (1998) 351-358.
- [119] D.R. Uhlmann, B. Chalmers, K.A. Jackson, Interaction Between Particles and a Solid-Liquid Interface, Journal of Applied Physics, 35 (1964) 2986-2993.
- [120] D. Stefanescu, A. Moitra, A.S. Kacar, B. Dhindaw, The influence of buoyant forces and volume fraction of particles on the particle pushing/entrapment transition during directional solidification of Al/SiC and Al/graphite composites, MTA, 21 (1990) 231-239.
- [121] D. Shangguan, S. Ahuja, D.M. Stefanescu, An analytical model for the interaction between an insoluble particle and an advancing solid/liquid interface, MTA, 23 (1992) 669-680.
- [122] G. Kaptay, Interfacial criterion of spontaneous and forced engulfment of reinforcing particles by an advancing solid/liquid interface, Metallurgical and Materials Transactions A, 32 (2001) 993-1005.
- [123] J.B. Ferguson, B.F. Schultz, P.K. Rohatgi, C.S. Kim, Brownian Motion Effects on the Particle Settling and Its Application to Solidification Front in Metal Matrix Composites, in: Light Metals 2014, John Wiley & Sons, Inc., 2014, 1383-1388.
- [124] D. Zhang, L. Nastac, Numerical Modeling of the Dispersion of Ceramic Nanoparticles during Ultrasonic Processing of A356-Based Nanocomposites, in: Advances in the Science and Engineering of Casting Solidification: An MPMD Symposium Honoring Doru Michael Stefanescu, John Wiley & Sons, Inc., 2015, 37-47, (ISBN 978-1-119-08238-5).
- [125] R. George, K.T. Kashyap, R. Rahul, S. Yamdagni, Strengthening in carbon nanotube/aluminium (CNT/Al) composites, Scripta Materialia, 53 (2005) 1159-1163.
- [126] S. Jia, P.G. Allison, T.W. Rushing, and L. Nastac, Ultrasonic Processing of 6061-based Nanocomposites for High Performance Applications, Advances in the Science and Engineering of Casting Solidification: An MPMD Symposium Honoring Doru Michael Stefanescu, John Wiley & Sons, Inc., 2015, 31-36, (ISBN 978-1-119-08238-5).

[127] W. Zhou, Z.M. Xu, Casting of SiC reinforced metal matrix composites, *Journal of Materials Processing Technology*, 63 (1997) 358-363.